IMPLEMENTATION OF SOLUTION AND SOLID STATE NUCLEAR MAGNETIC RESONANCE (NMR) SPECTROSCOPIC TECHNIQUES FOR QUANTITATIVE AND QUALITATIVE ANALYSES OF MOLECULAR SPECIES

A DISSERTATION IN
Chemistry
And
Physics

Presented to the Faculty of University of
Missouri-Kansas City in partial fulfillment of
The requirements for the degree of

DOCTOR OF PHILOSOPHY

By

ABRAR S.ALNAFISAH

B.Sc., Qassim University, 2009

M.Sc., University of Missouri-Kansas City, 2016

Kansas City, Missouri

2019

IMPLEMENTATION OF SOLUTION AND SOLID STATE NUCLEAR MAGNETIC RESONANCE (NMR) SPECTROSCOPIC TECHNIQUES FOR QUANTITATIVE AND QUALITATIVE ANALYSES OF MOLECULAR SPECIES

Abrar Saleh Alnafisah, Candidate for the Doctor of Philosophy Degree
University of Missouri-Kansas City, 2019

ABSTRACT

In this dissertation, spectroscopy has been used to solve a variety of problems in different domains of science. Therefore, each chapter consists of different examples that have been addressed using different concepts of spectroscopy.

The objective of part I (application of solution state NMR spectroscopy in pharmaceutical sciences) is to apply NMR techniques in different pharmaceutical projects. In chapter3, a real-time quantification of in vitro Bortezomib (BTZ) release from alginate microparticles using a solution-state quantitative boron nuclear magnetic resonance (^{11}B qNMR) method is presented. The method was validated according to International Conference on Harmonization (ICH) guidelines. Therefore, several analytical performance parameters were discussed such as limit of detection (LOD), limit of quantification (LOQ), linearity, specificity, accuracy, precision and robustness. The ^{11}B qNMR method was applied to the in vitro release study of a model drug, bortezomib (BTZ) from alginate microparticles and results were compared to a commonly used dialysis

method. Throughout the release study, the dialysis method consistently underestimated the level of drug released, probably due to the separating membrane that can interfere with the real-time drug transport process. Overall, compared to the dialysis method, the direct ^{11}B qNMR method was accurate and provided a direct and real-time quantification of BTZ for an effective study of drug release kinetics.

Similarly, in chapter 4, a ^{19}F qNMR method was developed and validated and then applied to study the real-time release of maraviroc from a microparticle formulation in a vaginal and seminal stimulated environment. Different possibilities were discussed to control the release profile such as the crosslinking process and a pH sensitive polymer.

In chapter 5, the project is a collaborative effort between the department of Chemistry and School of Pharmacy. Our contributions in that project are to utilize ^{11}B NMR spectroscopy technique as a characterization tool for the reaction progression. Moreover, to perform theoretical and experimental calculations and compare them to each other in order to trace the reaction mechanism. The overall motivation of the project is to test an assumption about phenylboronic acid (PBA) to prevent HIV transmission. It has been found that phenylboronic acid can form boronic acid in the presence of cis-diol, like the one found in HIV-gp120 glycoproteins. In order to exam the proposed hypothesis, a derivative of phenylboronic acid was synthesized. The synthetic scheme and the spectroscopic results are presented and discussed in detail.

The objective of part II (applications of solid-state NMR spectroscopy) is to apply SSNMR spectroscopy experiments in two projects to gain significant information about specific materials. In chapter 6, some main concepts of SSNMR spectroscopy are discussed as well as some basic SSNMR experiments.

In chapter 7, boron carbide thin films were grown using plasma enhanced chemical vapor deposition (PECVD) under different growth conditions. Different possible spectroscopic techniques were discussed in order to discover the local physical structure of boron carbide thin films. However, most of these techniques have shown a lack of an ability to demonstrate the internal structure of thin films. SSNMR spectroscopy was successfully employed to reveal information about the internal structure of boron carbide thin films.

In chapter 8, the optical properties of titanium oxide TiO_2 were modified by introducing a hydrazine molecule. SSNMR spectroscopy was implemented to monitor the reaction progression of TiO_2 to improve its optical properties.

APPROVAL PAGE

The faculty listed below, appointed by the Dean of the School of Graduate Studies, have examined this dissertation titled "Implementation of Solution and Solid Sate Nuclear Magnetic Resonance (NMR) Spectroscopic Techniques for Quantitative and Qualitative Analysis of Molecular Species", presented by Abrar S.Alnafisah, candidate for the Doctor of Philosophy Degree, and certify that in their opinion it is worthy of acceptance.

Supervisory Committee

Nathan A. Oyler, Ph.D. Committee Chair
Department of Chemistry

Zhonghua Peng, Ph.D.
Department of Chemistry

Shin Moteki, Ph.D.
Department of Chemistry

Elizabeth Stoddard, Ph.D.
Department of Physics

Megan Hart, Ph.D.
Department of Civil and Mechanical Engineering

Contents

LIST OF ILLUSTRATIONS

LIST OF TABLES

LIST OF ABBREVIATIONS

NMR: Nuclear magnetic resonance

FT-IR: Fourier-transform infrared

SEM: Scanning electron microscopy

BTZ: Bortezomib

MVC: Maraviroc

LOD: Limit of detection

LOQ: Limit of quantification

LD: Drug loading

AUC: Area under curve

VFS: Simulated vaginal fluid

SFS: Simulated semen fluid

HIV: Human immunodeficiency virus

PBA: Phenyl boronic acid

MAS: Magic angle spinning

PECVD: Plasma enhanced chemical vapor deposition

CP: Cross polarization

LG-CP: Lee-Goldburg cross polarization

REDOR: Rotational-Echo, Double-Resonance

REAPDOR: Rotational-echo, adiabatic-passage double-resonance

FPRFDR: Finite pulse radio frequency driven recoupling

DRAWS: Dipolar recoupling using a windowless sequence

ACKNOWLEDGMENTS

I would not have been able to achieve this Ph.D dissertation without the tremendous support and guidance that I have received from many people.

First of all, I would like to express my sincere gratitude to my advisor Dr. Nathan A. Oyler for all of his contributions and support during my doctoral journey. I really appreciate all of his time, patience, ideas and encouragement which made my experience more productive. He has always been there for my questions and offered constant feedback. His advice have been invaluable for both my research as well as my academic coursework.

I also would like to thank my committee members, Dr. Elizabeth Stoddard, Dr. Zhonghua Peng, Dr. Shin Moteki, and Dr. Megan Hart for all of their feedback, ideas, discussions, and insightful comments.

My sincere thanks also goes to Dr. Andre Clayborne for providing me an opportunity to work in his research laboratory. I have gained great experience and remarkable scientific knowledge through my Ph.D journey.

I would like to acknowledge the chemistry department, faculty, and staff and I am especially grateful for Dr. Kathleen Kilway, the chair of chemistry department, for all her valuable advice. She has been immensely supportive throughout challenging times. I also present my cordial gratitude to Dr. Charles Wurrey. I am glad that his courses were some of the first courses in the graduate program. He has been so supportive and encouraging and he has always gone above and beyond the expectations of a great professor. This list would not be complete if I were not to mention John J.Whitchurch, the electrical engineer in the chemistry department. I appreciate all

his generous assistance. Without his immediate contributions, my research projects would be unachievable.

I also present my cordial gratitude to our collaborators from the school of pharmacy Dr. Bi-Botti Youan, Dr. Fohona Coulibaly and Omowumi Akinjole. It was a pleasure to work with such brilliant scientists like them. I would like to thank our collaborators from Chemistry and Physics departments Dr. Xiaobo Chen and Dr. Michelle Paquette respectively. It was an eye-opening experience working with them.

I would like to thank Qassim University (QU) and Saudi Arabian Cultural Mission (SACM) for offering me a scholarship and giving me this opportunity to fulfill my dream.

I owe my deepest gratitude to my family. I am forever thankful to my parents Mr.Saleh Alnafisah, and Miss. Maryam Altasan, who believed in me and always encouraged me to follow my dreams. Their loves and prayers are what have sustained me so far and I hope I have made them proud. Special and profound thanks for my brothers and sisters for their unconditional love and guidance which are constantly with me. I also would like to express my warmest gratitude to my parents- in law Mr. Saleh Altasan and Miss. Nourah Altasan for all the sacrifices that they have made on my behalf along this journey.

My lovely kids, Sibaa and Saleh, who are the joy of my life. You have made me stronger and better than I could have imagined. Thank you for cheering me up and for being patient during my Ph.D studies.

Finally, there are no appropriate words to convey my recognition to my husband and soulmate, Ibrahim. He has been a constant source of support, love, and encouragement during my pursuit of my Ph.D degree. I deeply value his belief in me, and appreciate how he always reminds me how proud he is of me. Thanks Ibrahim for giving up so many things to make my Ph.D studies a priority in our lives. Thank you for taking up the responsibilities of our family. You lived every single minute of this journey and have dealt momentously with pressure and critical times during my studies and our time abroad.

To my parents, husband, and children
I dedicate this dissertation

Chapter 1 . INTRODUCTION

1.1 Overview

Spectroscopy is a very broad field which studies the interaction between matter and energy. It is divided into various subfields based on the nature of interaction as well as the type of material. When matter is exposed to electromagnetic radiation, different types of interactions may occur including absorption, emission, reflection, elastic scattering, and inelastic scattering[1]. All these interactions can happen to different components of a molecule. For instance, electronic excitation (UV) occurs in between electron orbitals, molecular vibrations (IR) takes place in the molecule, and nuclear spin transitions (NMR) occur in the nucleus. Despite the difference of interactions, all spectroscopic techniques measure the change in intensity and/or frequency of the energy of the interaction. The interpretation of those interactions reveal fundamental information about physical structure. Spectroscopy is used daily in chemistry as it can accurately probe information about atomic and molecular properties. Understanding the physical structure of a molecule is an essential step in analytical chemistry. Various types of spectroscopic techniques can be applied to achieve this goal like Solution State and Solid State nuclear magnetic resonance (NMR) spectroscopy, Infrared (IR) spectroscopy, Ultraviolet/ visible (UV/Vis), Atomic absorption (AA), atomic emission (AE). In this dissertation, I have mainly utilized solution state and solid state NMR as well as IR to obtain quantitative, qualitative, and theoretical analyses of different molecular species in different contexts.

1.2 NMR

In 1938, Nuclear Magnetic Resonance Spectroscopy was discovered by Isidor Rabi who was awarded the Nobel prize in physics 1944[2]. NMR phenomena is very suitable technique to examine the chemical, physical and biological properties of matter. NMR is powerful and widely used analytical tool in chemistry, biology, pharmacy and geology. It is a non- destructive technique that has greatly contributed to compound identification. For modern studies, NMR turns out to be an indispensable technique as it can give a multitude of information about molecular structure including configuration, concentration, and intermolecular interaction at the atomic level. Nowadays, chemists are able to obtain 2- and 3- dimensional NMR spectra by a few clicks of a button. Although NMR has been utilized routinely, care must be taken when setting NMR experimental parameters. Incorrect setup may convert the spectra from a beneficial to a meaningless result. Furthermore, this could lead to damaging the equipment, which will cost thousands of dollars to repair. Hence, understanding the basic concepts of NMR can ensure the best results.

In order to understand NMR phenomena, it is important to have a closer look at molecular structures, which are usually the target matter examined by NMR. A molecule is composed of atoms, which are made of electrons and nuclei. Under the electron cloud of an atom lies the nucleus with its neutrons and protons. The proton, neutron, and electron possess a property called a spin, which acts as a small magnetic dipole. Hence, NMR phenomena relies on intrinsic spin properties of nuclei. Spin can be expressed using the quantum number (I). In order for any given nucleus to be NMR active, it has to have a non-zero net spin, which occurs when we have unpaired protons and/or neutrons (Table1-1).

In the absence of an external magnetic field (B_0), each magnet orients randomly. When external magnetic fields are applied, all magnets are aligned and precess around the magnetic field. For isotopes with spin =1/2 such ^1H and ^{13}C, there are 2I+1=2 possible orientations which can be distinguished by quantum number m (m= +1/2 or -1/2). In the absence of external magnetic fields, all nuclei are oriented randomly because of thermal effects and spin vectors that orient everywhere leaving zero net magnetization. When an external magnetic field is applied, nuclei with non-zero spin angular momentum orient either aligned or opposite with the external magnetic field as shown in (Figure1-1)[3]. For nuclei with a positive gyromagnetic ratio γ, the parallel orientation which has lower energy (α spin state or +1/2) is preferred more than the antiparallel orientation which has higher energy (β spin state or -1/2). At equilibrium, the population of the alpha state is slightly higher than the beta energy state. This interaction between external magnetic fields and nuclear magnetic moment is known as a Zeeman splitting (Figure1-2)[3]. Mathematically, we can calculate the population difference using Boltzman distribution ($N^-/N^+ = e^{-E/kT}$ where k is Boltzman's constant 1.3805×10^{-23} JK^{-1})[4]. The population difference leads to a net magnetization (M_o) vector in Z+ direction. This net magnetization is precessing around B_0, and this precession is known as Lamor precession Equation(1-1) (Figure1-3)[3] where B_0 is the magnetic field and γ is the gyromagnetic ratio. The Lamor frequency is proportional to the magnetic field.

$$\omega^0 = -\gamma B_0 \qquad (1\text{-}1)$$

When electric current is applied through a wire coil, it will generate a magnetic field (B_1) inside the coil. NMR is performed with two magnetic fields, one large Zeeman field and another much smaller field used to perturb the net magnetization. As shown in (Figure1-4)[3] the second magnetic field is oriented perpendicular to the B_0. If the current of the electrical wire which is used to generate the second magnetic field B_1 oscillates at the same frequency of Lamor frequency ω^0, the energy will be absorbed and the population of α and β are perturbed. Under these circumstances, the net magnetization (M_0) is tipped into the xy plane precessing around B_1 simultaneously with its precession around B_0. The application of B_1 will be briefly applied for $\leq$ seconds and is known as a radio frequency RF pulse. When B_1 is turned off, the net magnetization relaxes back to equilibrium along the Z-direction (Figure1-5)[3]. During the relaxation process, a current profile of the current developed in the coil by the precessing net magnetizations is recorded.

This profile is identified as the free induction decay (FID). Since the FID is in a time domain, a mathematical technique called Fourier transform (FT) will be performed to convert the FID from time domain to frequency domain (Figure1-6)[3].

Nuclei with a quantum spin number higher than 1/2 are called quadrupolar nuclei. In the application of an external magnetic field, the energy splits into multiple levels (Figure 1-7)[5]. Boron has a 3/2 spin number. Therefore, it will split into five different energy levels. More about quadrupolar nuclei will be discussed later.

An NMR spectrum is a plot of absorption against frequency. For any given nuclei with spin 1/2, the NMR spectrum ideally should look like the spectrum in (Figure1-8)[6]. Several parameters can be extracted from the spectrum such as central frequency, area, and line-width. The central frequency is related to the chemical shift, which is the position of the peak shown in ppm value. The chemical shift is very important as it reveals information about the local environment. The area is related to the number of spins, which is the number of nuclei present at that shift. Line-width has number of components, including some orientation dependence.

1.3 Relaxation

The two fundamental types of relaxation in NMR include spin-lattice relaxation or longitudinal relaxation (T1) and spin-spin or transverse relaxation (T2). These phenomena describe how the signal changes with time. Understanding the concept of relaxation is important for an appropriate NMR spectrum measurement and interpretation [7–9].

When there is no external magnetic field applied, the total magnetic polarization is zero for any given active nuclei. Nonetheless, when the external magnetic field is suddenly applied, the total magnetic moment is initially zero and it will gradually grow until reaching thermal equilibrium. The loss and gain of the net magnetization around z-axis is known as a Spin-lattice relaxation or longitudinal relaxation with a time constant T1. The term 'lattice' formerly used in the early days of NMR when they used the interaction of nuclear spins and crystal lattice to explain the thermal equilibrium. Conversely, the term 'longitudinal' is used to indicate that the magnetization build up is in the same direction as the applied magnetic field B_0. The term 'relaxation' is commonly used, especially in physics, with a particular meaning indicating the re-establishment of thermal equilibrium after applying some perturbation. Equation (1-2) governs this process as a function of time. In the absence of the magnetic field, the equilibrium is established, and then broken after applying an external magnetic field. The longitudinal spin magnetization builds up and establishes a new equilibrium state (Figure1-9)[10]. The spin-lattice relaxation time constant T1 depends on the sample and some of its parameters such as temperature and viscosity (if the sample is in solution state). For most samples, the relaxation time constant can range from milliseconds to seconds; however, there are a few materials in which T1 can span hours or days [4].

$$M_z = M_0 \, (1-e^{-t/T1}) \qquad (1\text{-}2)$$

Where: M_z longitudinal magnetization

M_0 magnetization at the equilibrium

t time

T1 spin-longitudinal relaxation time constant

In the presence of the large external magnetic field B_0, the longitudinal spin magnetization is too small to be detected. It is four times smaller than the normal diamagnetism of the sample in magnitude. Hence, NMR spectroscopy follows a different methodology, which involves perturbing the magnetization and then measuring the perpendicular magnetization instead of measuring the net magnetization along the external magnetic field.

If a radio frequency pulse is applied (r.f pulse $\pi/2$), the magnetization will rotate from z-axis to –y-axis. Therefore, all the net spin polarization will transfer from z-axis to –y-axis, where it will be perpendicular to the magnetic field (Figure1-10). This perpendicular magnetic moment is known as a transverse magnetization. When the r.f pulse is suddenly turned off, the transverse magnetic moment around –y-axis will gradually decay and simultaneously start precessing around the z-axis. The time it takes the transverse magnetic moment to decay is called spin-spin relaxation or transverse relaxation time constant T2, and it can be described using Equation (1-3).

$$M_{xy}= M_{xyo}\, e^{-t/T2} \qquad (1\text{-}3)$$

Where : M_{xy} transverse magnetization

M_{xyo} transverse magnetization at equilibrium

t time, T2 transverse relaxation time constant

In theory, T_2 can be measured by applying a specific pulse to create a transverse magnetization and then measure the decoherence constant of the FID. However, in fact there are several parameters, which dramatically influence the rate of the decay such as magnetic field inhomogeneity, sample inhomogeneity, and anything that perturbs the internal motion like temperature and humidity. As a result of these effects, the decoherence constant of the FID is called T_2^* rather than T_2. Generally, T_2 is greater than or equal to $T_2^{*.}$ Moreover, T_2 is an instrumentally independent parameter while the T_2^* is not. According to Equation (1-4), T_2^* governs the apparent line width of the NMR spectrum.

There are different factors that can be the main sources of broadening NMR lines. Some of them are related to instrumental problems such as tuning and shimming while others are related to sample problems such as sample inhomogeneity (poor mixing) and temperature gradients around the sample. However, the source of NMR line broadening topic would be incomplete without mentioning motion based relaxation. Internal motion can play a significant role in both the intensity and width of the NMR peak.

The spin-lattice relaxation mechanism depends on the rate of molecular motion; this motion is related to the correlation time, which is the time it takes a spherical molecule to rotate by one radian. The spin-lattice relaxation (T1) will be large when we have a molecule with a very small correlation time, which also indicates a rapid molecular motion as shown in (Figure 1-11)[11]. Moreover, T1 is also large when we have a solid sample since the molecular motion is hindered and the correlation time is too long. Under these circumstances, the intensity will not be as strong at that frequency as it would be. Interaction with unpaired electrons such as paramagnetic substances can lead to a fruitless line broadening in NMR. Lastly, in quadrupolar nuclei (I> ½) there will be an interaction with the electric field gradient which typically results in very short relaxation time and, thus, broaden the NMR lines.

There is a notable relationship between T1 relaxation and the chemical structure. When comparing the T1 value for two different carbon ,quaternary carbon and carbon bonded directly to a proton, we will find that the T1 value for the quaternary carbon can vary from 10-300s. On the other hand, the T1 value of a carbon bonded directly to a proton only ranges from 0.1-10s. This is because of the ^{1}H-^{13}C dipole-dipole interaction, which has a direct effect on T1. Typically, the more hydrogen atoms attached to ^{13}C, the smaller T1 value will be.

NMR signal reduction derived from incorrectly estimating the value of T1 can be avoided by setting up the spin-lattice relaxation time constant accurately. The most common experiment to measure T1 is the inversion recovery experiment. Figure1-12[11] shows the pulse sequence of the inversion recovery experiment. More details about T1 measurements will be discussed later.

Not only does T1 have a critical effect on broadening NMR signal, but T_2 (spin-spin relaxation) also has a significant effect too. According to the Equation (1-4), the linewidth of the NMR signal is directly dependent on T_2. The size of molecule, viscosity and hydrophobicity tend to vary the T_2 value remarkably[12,13]. When molecular weight increases, the correlation time increases too. Therefore, T_2 decreases and the line width of NMR peak increases.

Large molecules such as a polymers and proteins have a tendency to possess a very slow molecular tumbling and a long correlation time. Therefore, these large molecules have relatively small T_2 values (Figure1-11) which will result in a very broad NMR signal Equation (1-4). We took advantage of the T_2 molecular size dependent and studied a real-time quantification of boron and fluorine containing drugs' release from nano/microparticles formulations. When the drug is free in the solution, we can see a clear ^{11}B or ^{19}F NMR peak with a narrow line. However, when the drug is encapsulated inside the polymer, it has a very fast T_2 and, thus, a very broad and noisy NMR signal is not observed.

In solution-state NMR, the viscosity of the solvent plays a substantial role in T2 value since different measurements give different T2 values. As shown in (Figure1-11), as the viscosity increases, the T2 gets smaller. Consequently, the NMR peak will be more broad and noisy[14,15]. Additionally, interactions between solvent and solute have a key influence on T2. It has been found that the polar or hydrophobic environment samples can drive clustering which eventually will cause of broadening the signal[16]. More about this topic will be covered later.

$$\text{Line width} = (1/T^{*}_{2})^{-1} \qquad (1\text{-}4)$$

1.4 Interactions in NMR

Generally, there are internal and external interactions in NMR for any given nucleus as shown in Equation (1-5). Table 1-2 and (Figures1-13,14) [17]show the relative magnitude of these interactions and how these interactions can cause a small perturbation of the resonance from the lamor frequency. The Zeeman and quadrupolar interactions are the largest, on the order of 100MHz and 1-5MHz respectively, followed by dipolar and chemical shift interactions which are on order of 1-5KHz. The smallest interaction is related to J-coupling interaction, which is only $<10^2$ Hz [18].

$$\hat{H}_N = \hat{H}_Z + \hat{H}_Q + \hat{H}_{DD} + \hat{H}_{cs} + \hat{H}_J \qquad (1\text{-}5)$$

Where: $\hat{H}_Z$ is the Zeeman interaction

$\hat{H}_Q$ is the quadrupolar interaction

$\hat{H}_{DD}$ is the dipolar interaction

$\hat{H}_{cs}$ is the chemical shift

$\hat{H}_J$ is the J-coupling

1.4.1 Zeeman interaction

The Zeeman interaction is an external interaction, which occurs between the spin magnetic moment and magnetic field B_0.

1.4.2 Chemical shift

The chemical shift δ is the resonance frequency of a nucleus relative to a standard in a magnetic field. Typically, it is expressed in parts per million (ppm). Chemical shifts provide essential information about the structure of the molecule and assist in compound identification. Moreover, chemical shifts play a supporting role in distinguishing which nucleus belongs to which functional group. Chemical shift is an anisotropic parameter, which means it is directionally dependent. The magnitude of the chemical shift depends on the orientation of the molecule relative to the applied magnetic field. Hence, chemical shift is a three dimensional property. In solution NMR, the molecules randomly tumble, and their motions are significantly faster than the actual NMR experiment. Therefore, the obtained chemical shift is the average chemical shifts of all molecular orientations, and it is known as the isotropic chemical shift (Figure1-15).

On the other hand, in solid- state NMR, the situation is entirely different. The orientation of the solid sample is restricted. For example, an amorphous solid sample can be approximated as composed of lots of single crystals oriented in all directions with respect to the applied magnetic field. Under these circumstances, different chemical shifts will be observed which will cause a substantial broadening in the peak because of the different orientations. The shape of the peak, known as a powder spectrum, is shown in (Figure1-16)[19]. Unlike amorphous solid, in a single crystal (crystalline solid) all molecules have the same orientation with respect to the magnetic field. Hence, a narrow peak is going to be observed. If the single crystal changes its orientation, the peak is going to move to a different chemical shift as shown in (Figure1-17).

1.4.3 Dipolar interaction

The dipolar interaction is a direct interaction between nuclear spins through space. It is classified to homonuclear and heteronuclear coupling. In homonuclear coupling, the interaction happens between identical nuclear isotopes while in heteronuclear coupling the interaction happens between different nuclear isotopes.

A nucleus with spin ½ possesses a dipole moment, so it will be oriented either parallel or anti-parallel to the static magnetic field, and these two spin states have almost equal energy. Frequently, the interesting nuclei is not in an isolated system, which means that nucleus is surrounded by another nuclei. These nuclei also have multiple spin states. The target nucleus will be influenced by the spin states of the neighboring nucleus via dipolar and J coupling. Consequently, the line in the NMR spectrum is going to be split into a multiplet.

A nucleus with spin higher than ½ possesses a quadrupole moment and it will have more than two spin states. When the interested nucleus is influenced by another nucleus, the line in NMR spectrum is going to split to a different multiplet.

1.4.4 J-coupling

In contrast to dipolar coupling, J-coupling is an indirect interaction of nuclear spins mediated by the electrons in the molecule. Typically, the anisotropic part of the interaction is very small and can be neglected, so only the isotropic value is relevant.

In SSNMR spectroscopy, J-coupling is indeed hard to measure because of the resolution problems. Hence, J-coupling is not as important in SSNMR spectroscopy as in solution state NMR spectroscopy where it provides valuable information about connectivity through bonds.

1.4.5 Quadrupolar interaction

The quadrupolar interaction is a crucial topic in both solid and solution NMR spectroscopy. It is defined as an electric coupling between the nuclear quadrupole moment Q and local electric field gradient. Nuclei with spin $I=1/2$ have a spherical positive charge distribution in contrast to quadrupolar nuclei with spin $I>1/2$. It has an asymmetric distribution around the nucleus, which will give a rise to a non-spherical positive charge distribution. The asymmetric positive charge distribution can be described by the nuclear electric quadrupole moment (eQ), which is an intrinsic property of the nucleus. The quadrupole nucleus interacts with an applied magnetic field while the electric quadrupole moment interacts with the electric field gradient (EFG). The strength of this interaction depends upon two main factors: the magnitude of electric quadrupole moment (eQ) as well as the strength of electric field gradient (EFG). Mostly, the electric quadrupole moment expresses as eQ, where e is the positive charge of a proton, and it has a constant value for any given quadrupole nuclear regardless of the change in the electric field gradient.

When the strength of the zeeman interaction (applied magnetic field B_0) with the nucleus is on the similar order of magnitude to the strength of quadruple interaction, then the applied field will not be considered as the quantization axis any more leading to 2nd order perturbation effects. The interaction will be anisotropic, so it depends on the orientation with respect to the magnetic field. In order for the zeeman and quadrupole interactions to be comparable, they do not have to be identical in scale, for instance, for ^{11}B the zeeman is around 115 MHz while a big quadruple interaction is around 5 MHz, (less than 5%), the second order effects are still present.

1.5 Averaging of NMR interactions

In solution state NMR spectroscopy, molecular motion is freely random, hence all anisotropic interaction will average to zero. However, in SSNMR spectroscopy the molecular motion is absent or severely restricted. Consequently, all these interactions are going to lead to a very poor spectrum with a broad line and lower resolution, which makes the identification and the analysis of the spectrum featureless as shown in (Figure1-18) [17]. In order to enhance the spectrum's quality and resolution, the sample must be spun at the magic angle with respect to the applied magnetic field. More about the magic angle spinning technique will be covered later in chapter 6.

1.6 Solution NMR vs. SSNMR spectroscopy

As a tool of analysis, solution state NMR is well established and has evolved rapidly. Generally, when NMR is mentioned it refers to solution state NMR spectroscopy. The structural information is acquired based on the isotropic interactions like isotropic chemical shift and J coupling, as well as relaxation information. In order for this type of experiment to be applicable, the sample has to be in a solution phase for testing. Unlike SSNMR, solution state NMR has better resolution, narrow linewidths, and strong signal intensity due to the rapid isotropic orientation and apparent lack of anisotropic interactions[20]. However, the target sample has to be soluble in deuterated solvents to acquire proton solution NMR spectrum.

In contrast to well-known solution state NMR, the structural information that we gain from SSNMR is based on chemical shift anisotropy (CSA) and dipolar coupling, regardless of the solubility and crystallinity of the sample. Typically, SSNMR spectrum has broader linewidths and has lower resolution compared to the solution NMR spectrum. There are three important reasons that make the SSNMR spectrum less readily useful. First is the dipolar broadening which is the interaction between two spins. Second is the chemical shift anisotropy (CSA) which arises from the asymmetry of electronic density around the nuclei. Third is the quadrupolar interactions. In the solution NMR spectroscopy, all these factors average to zero due to the fast isotropic motion of the sample. Luckily, we can mostly average all these factors to zero and acquire high-resolution spectra with narrow lines, ~0.1Hz for solution and 1-100 Hz solid state NMR respectively, by applying different strategies such as magic angle spinning (MAS)[21,22] and cross polarization (CP)[23,24] since all of the factors are orientation dependent. More explanation about these strategies will be discussed later.

In order to identify the structural information of any given sample, a high abundance of these nuclei is required to make this technique sensitive, and give high signal-to-noise (S/N) SSNMR spectra. Unfortunately, not all nuclei have high abundance, specifically ^{13}C which makes up only 1% of all natural carbon on earth. Consequently, NMR spectroscopy is going to be significantly less sensitive to those nuclei and our analysis will be hampered by a low signal-to-noise ratio due to the low natural abundance. Moreover, since there are spin-spin heteronuclear interactions, we can implement heteronuclear correlation experiments between different nuclei based on the S/N. It is essentially impossible to determine homonuclear correlations for certain specific nuclei in a natural abundance sample such as ^{13}C. If a correlation experiment is performed to measure ^{13}C-^{13}C distance, the probability of a neighboring ^{13}C is only 1%, and the maximum peak height that can be gained is going to be only 1%. Therefore, using isotopic labeling schemes will have major impacts such as an improvement in S/N by a factor of ~90 fold in homonuclear correlations experiments. Another impact is the ability to measure interatomic distances by doing correlation experiments and 2D experiments [25].

In contrast to solution state NMR, SSNMR sample preparation and handling are difficult. Packing and unpacking the sample in a very small rotor is more complicated than ejecting the sample in NMR tube for solution NMR. Additionally, to use it properly, SSNMR requires more expertise [5,26].

1.7 NMR components

Generally, NMR spectrometer contains several parts: the magnet, the shim coils, the probe, the transmitter, the receiver and the computer. Figure 1-19[27] shows a schematic representation for NMR components [27,28].

The NMR magnet is the most essential part of NMR hardware as well as the most expensive one. Most NMR experiments require a homogenous magnetic field along with a highly stable magnetic field. These requirements are necessary to acquire a spectrum with better resolution and avoid a broad NMR signal. The magnet in early NMR spectrometer systems was iron core permanent or electromagnetic and it generated only a 1.5 T magnetic field. However, the type of magnet has evolved substantially. Recently, most NMR spectrometers have superconducting magnets, which have a strength field from 6 to 23.5 T. The superconducting magnet wires are made of $(NbTaTi)_3Sn$, and embedded with copper because this material is fragile. The superconducting wire has zero electrical resistance below 4K. Therefore, it has to be cooled to reduce the electrical resistance. To achieve that, the superconducting magnet is immersed in liquid helium (-269°C or 4K). The wire and liquid helium are in a big container, which is surrounded by vacuum and then liquid nitrogen (77K) which acts as a thermal buffer between the outside temperature (293K) and liquid helium. Followed by liquid nitrogen, there is a vacuum region filled between liquid helium and liquid nitrogen which has several layers of reflective mylar film to reflect thermal photons and then block any heat from entering the magnet.

Shim coils come after the magnet (Figure1-19). The purpose of shim coils is to adjust the homogeneity of the B^0 magnetic field. Hence, shim coils generate a small magnetic field opposed to the B^0 inhomogeneous and cancel out any inhomogeneity (Figure 1-20)[27].

The transmitter section contains several parts namely, r.f synthesizer, pulse gate, pulse programmer, and amplifier. Each part of the transmitter has its own function. The r.f synthesizer produces an electrical signal with a specific frequency. Under the control of pulse programmer, the r.f pulses are allowed to pass through the pulse gate. The amplifier is utilized to increase the amplitudes of r.f pulse before transmitting to the probe.

The probe is a distinctive part of NMR spectrometer and the way to communicate with the sample. Moreover, it is the main difference between solid and solution state NMR spectrometers. The probe consists of r.f coil, sample spinner, temperature control circuity, and gradient coils. The probe's tasks are:

1. To hold the sample in appropriate place where the magnetic field is homogenous so we can acquire a spectrum with a narrow line (Figure 1-21). When the sample is placed in a more inhomogeneous field, the result spectrum will be broad as shown in (Figure 1-22).

2. To send r.f energy to the sample.
3. To detect the signal from the sample.

The receiver is responsible for detecting and converting the signal to readable data.

1.8 The basics of quantitative NMR (qNMR)

The first application of qNMR was in 1963 by Jungnickel and Forbes [29]and Hollis[29]. Jungnickel and Forbes determined the intramolecular proton ratio in different organic solvents while Hollis determined the amount of three components namely: aspirin, caffeine, and phenacetine in separate mixtures. In the past decades, qNMR was an efficient tool to quantify essentially organic chemicals and proton qNMR specifically was mostly commonly used. Nowadays, qNMR is becoming a well-established and widely popular technique among numerous fields such as the pharmaceutical and food industries [30–32]. When proton qNMR is applied to study complex molecules, which have multiple protons in their structure, the proton qNMR becomes relatively challenging because of peaks overlapping. Therefore, the usage of other active nuclei would be a suitable option to perform qNMR accurately[33–35].

In order for any NMR peak to be quantifiable, certain requirements have to be obtainable in that peak. First of all, the line shape of the peak has to be integrated and has a good resolution. Moreover, the relaxation time should be $5*T_1$ with the purpose of getting a complete relaxation and avoiding intensity distortion. Lastly, the quantified NMR peaks should be in a similar environment.

Several advantages of qNMR allow this technique to compete among other chromatographic methods. For instance, the area of integrated signal peak is directly proportional to the number of nuclei contributing to the signal. It is a non-destructive and highly predictable technique in which no intensity calibration is required. It has short measuring times and fast acquisition. Sample preparation and handling are relatively easy. In NMR spectroscopy, the characterization of analytes in mixtures are routinely conducted without a need for prior isolation or purification.

The fundamental theory of qNMR is based on the direct proportional relationship between the signal response (integrated signal area) (Ix) for a compound X and the number of nuclei (Nx) producing the NMR signal[36].

qNMR principle is governed by Equation (1-6), where Ks represents the NMR spectrometer constant. For a given NMR spectrum, Ks is identical for all resonance lines so the ratio of I_x and I_y is equivalent to the ratio of N_x and N_y Equation (1-7). The molar ratio of a given compound in a mixture of analytes can be determined using Equation (1-8), where n_x/n_y is the molar ratio of compound x and y. Hence, the mole fraction of compound X in a mixture of components m can be found by using Equation (1-9). An internal standard with known purity is required in order to determine the purity of compound x in a mixture using Equation (1-10), where p_x, M_x , and m_x are the purity, the molecular weight, and the mass of compound X respectively. Whereas p_{std}, M_{std} , and m_{std} are the purity, the molecular weight, and the mass of the standard.

$$I_x=K_s\times N_x \qquad (1\text{-}6)$$

$$\frac{I_x}{I_y}=\frac{N_x}{N_y} \qquad (1\text{-}7)$$

$$\frac{n_x}{n_y}=\frac{I_x}{I_y}\frac{N_y}{N_x} \qquad (1\text{-}8)$$

$$\frac{n_x}{\sum_{i=1}^{m} n_i}=\frac{I_x/N_x}{\sum_{i=1}^{m} I_i/N_i}\times 100\% \qquad (1\text{-}9)$$

$$\mathrm{P_x}=\frac{\mathrm{I_x}}{\mathrm{I_{std}}}\frac{\mathrm{N_{std}}}{\mathrm{N_x}}\frac{\mathrm{M_x}}{\mathrm{M_{std}}}\frac{\mathrm{m_{std}}}{\mathrm{m_x}}\mathrm{P_{std}} \qquad (1\text{-}10)$$

Table 1-1. Nuclei of interest in this dissertation

Nuclei	neutron	proton	Nature abundance	Net spin
^{1}H	0	1	99.985%	½
^{2}H	1	1	0.015%	1
^{12}C	6	6	98.9%	0
^{13}C	7	6	1.1%	½
^{10}B	5	5	19.97%	3
^{11}B	6	5	80.0%	3/2
^{19}F	10	9	100%	½

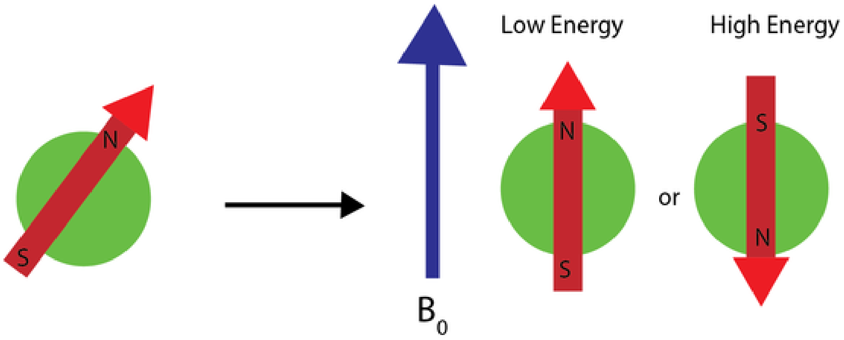

Figure 1-1.An effect of applying external magnetic field

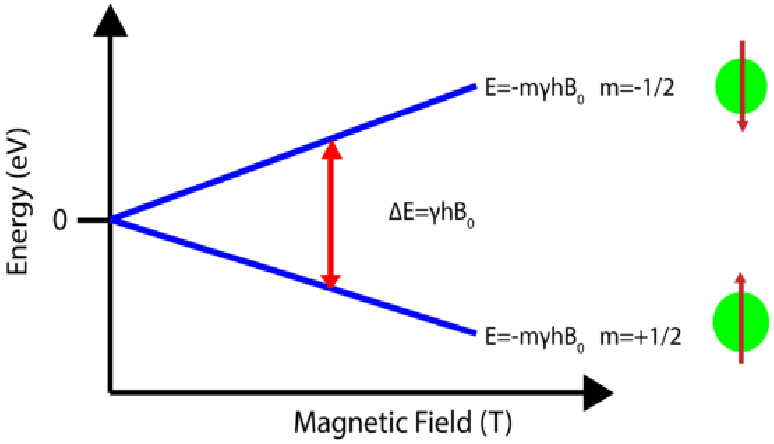

Figure 1-2. Zeeman splitting. The splitting grows proportionally to the magnetic field

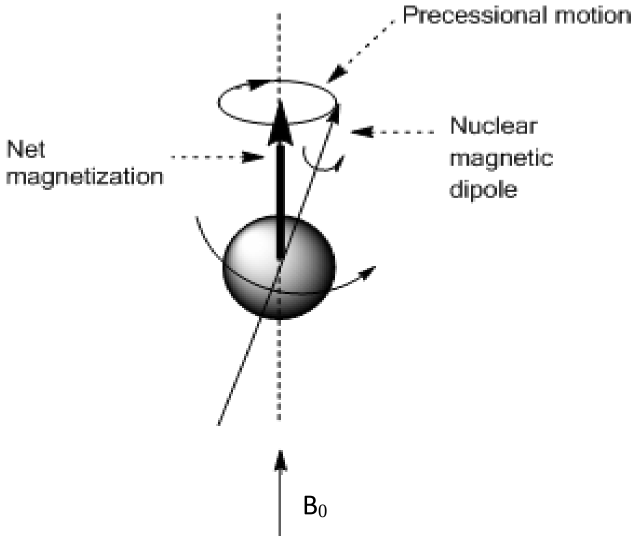

Figure 1-3. Lamor precession. The spin magnetic moment experiences a torque due to the presence of the magnetic field which causes it to precess

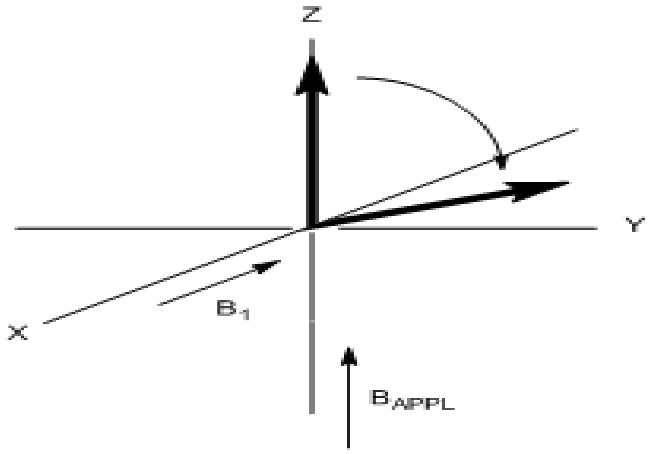

Figure 1-4. Application of the secondary magnetic field causes precession about that axis, causing the net magnetization to rotate into the x-y plane

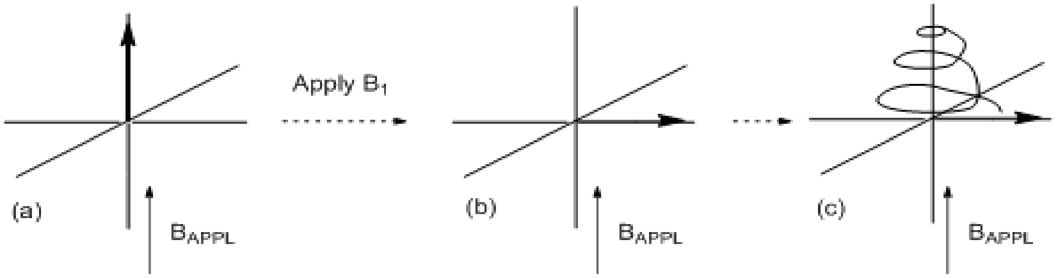

Figure 1-5. Relaxation process of the net magnetization to equilibrium when B_1 is turned off

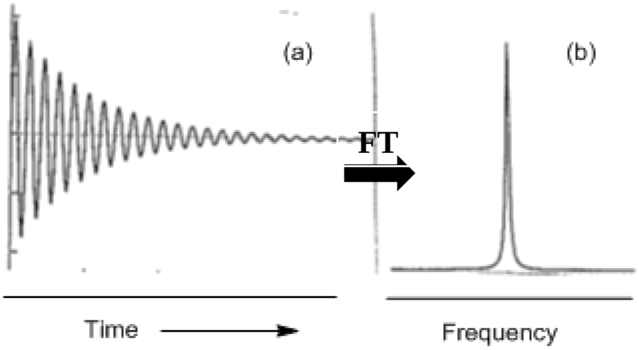

Figure 1-6. Converting FID from time domain to frequency domain

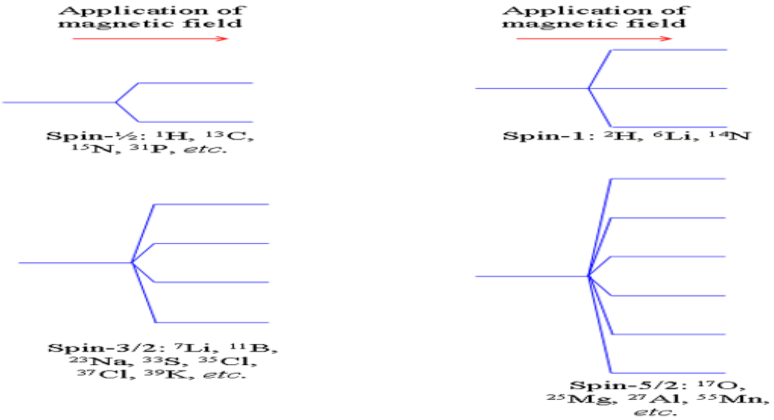

Figure 1-7. Energy splitting diagram for quadrupole nuclei when external magnetic field applied

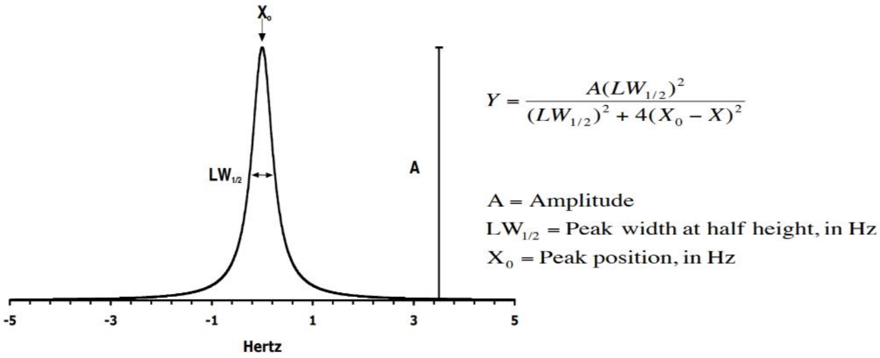

Figure 1-8. NMR spectrum. Important parameters are the line position, intensity, and width

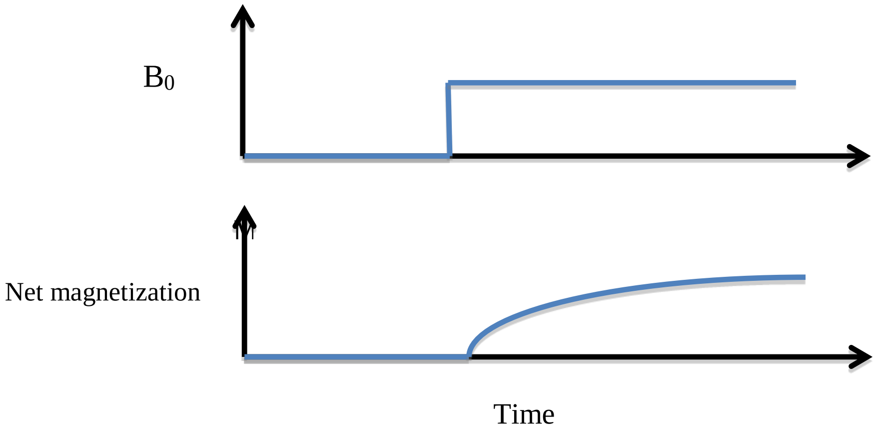

Figure 1-9. The longitudinal spin magnetization builds up to establish a new equilibrium state

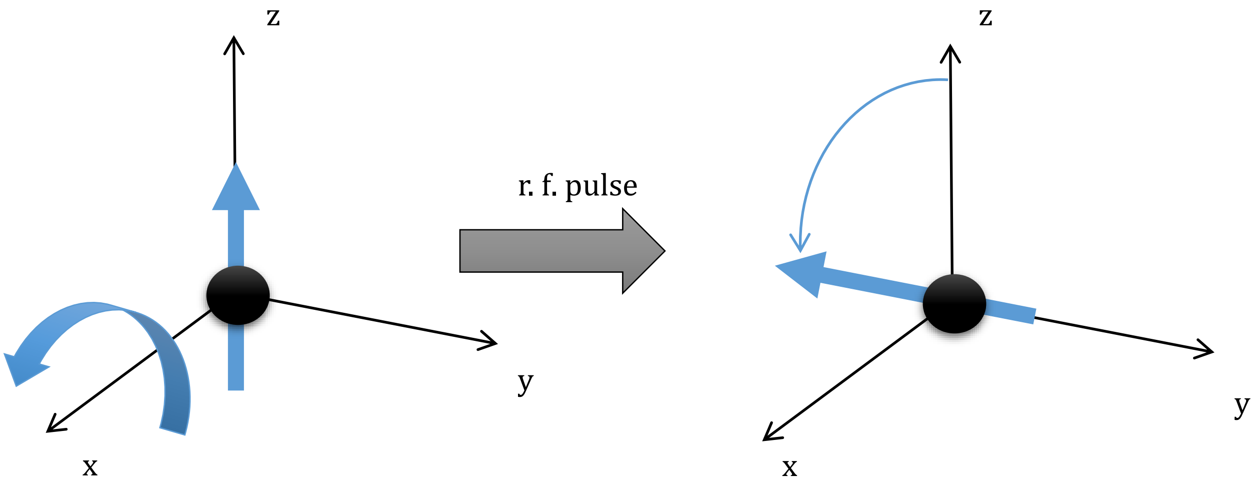

Figure 1-10. The magnetization will rotate from z-axis to –y-axis when an r.f pulse is applied

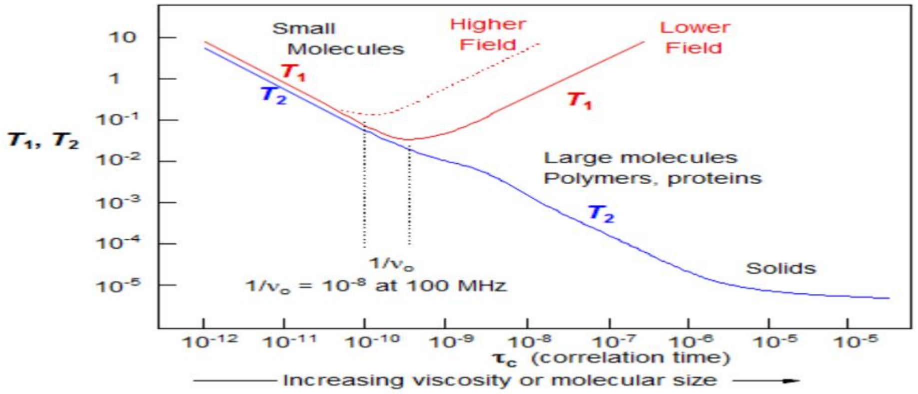

Figure 1-11. T1 and T2 as a function of molecular correlation time

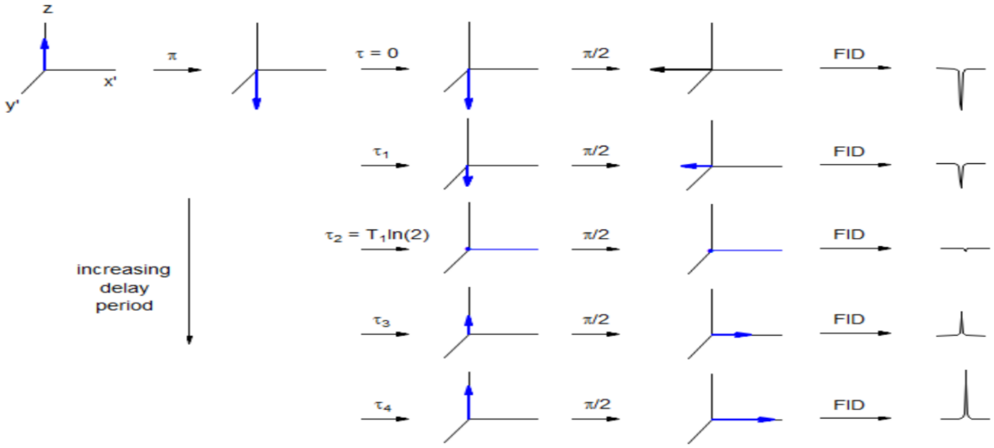

Figure 1-12. Inversion recovery experiment to measure T1

Table 1-2. The approximate relative magnitudes of NMR interactions

Interaction	Magnitude(Hz)
Zeeman	10^8
Quadrupolar	10^6
Chemical shift	10^3
Dipole	10^3
J-coupling	10

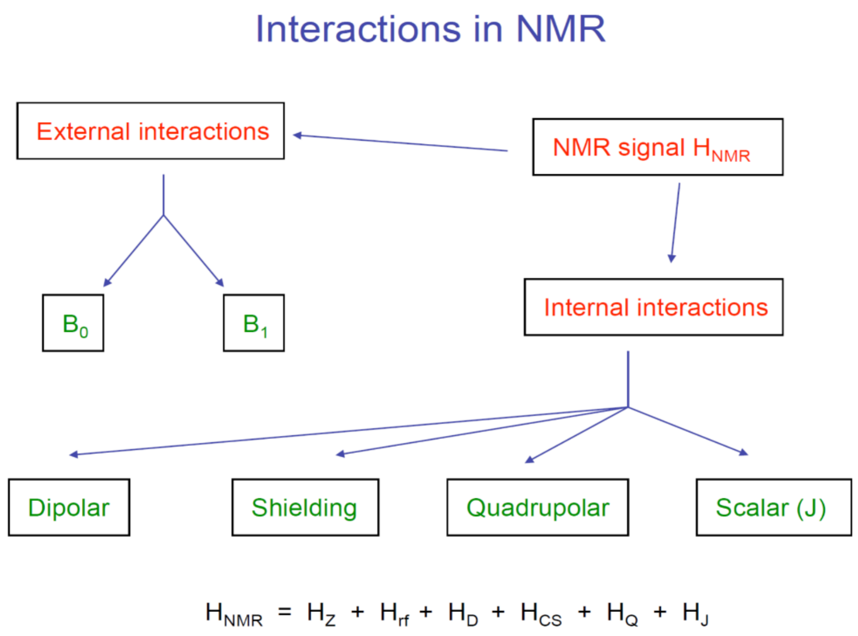

$$H_{NMR} = H_Z + H_{rf} + H_D + H_{CS} + H_Q + H_J$$

Figure 1-13. Common NMR interactions including interactions between the spin and magnetic fields and the interactions between spins

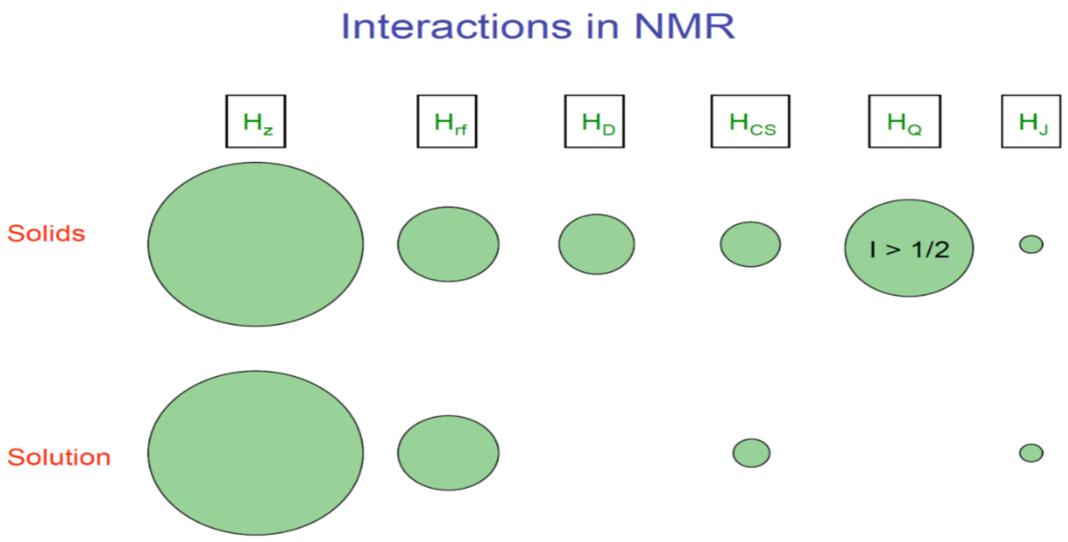

Figure 1-14. The magnitudes of NMR interactions in different sample phases due to rotational averaging

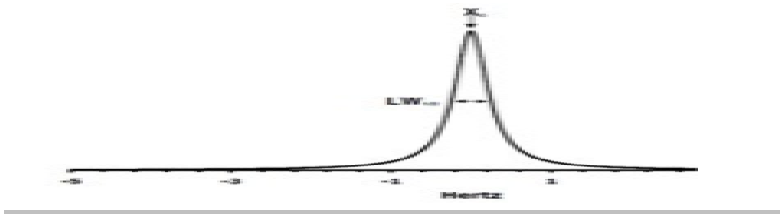

Figure 1-15. Solution NMR spectrum gives a single narrow line due to fast to rotational averaging

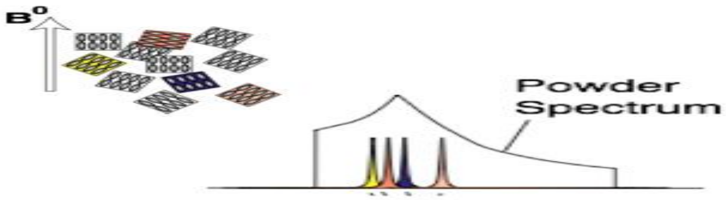

Figure 1-16. Amorphous SSNMR spectrum gives a broad peak with an asymmetric line shape due to the presence of all possible orientations of the crystallites

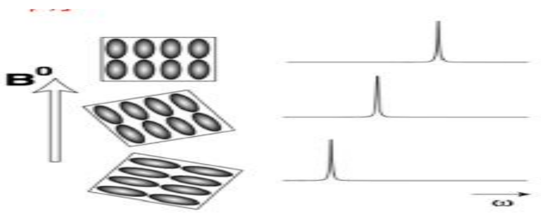

Figure 1-17. Single crystal SSNMR spectrum with the crystal sample oriented with different orientations

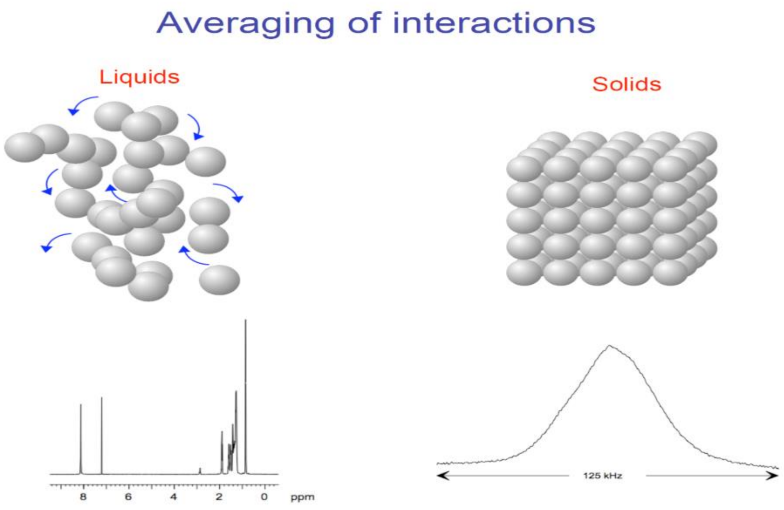

Figure 1-18. Averaging of rotational interactions in NMR spectroscopy

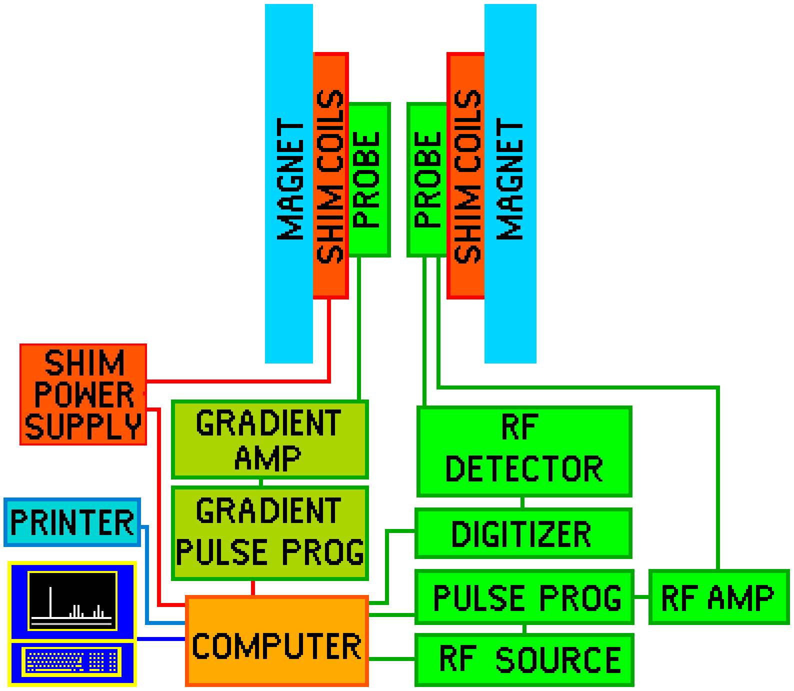

Figure 1-19. NMR spectrometer components

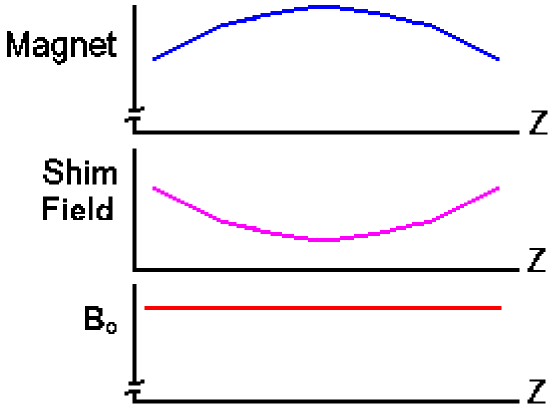

Figure 1-20. The shim field creates an opposing magnetic field to cancel out inhomogeneity in B0 over the volume of the sample

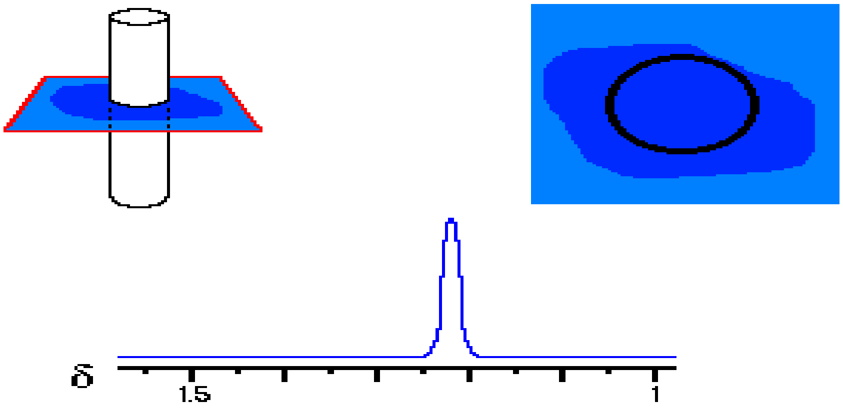

Figure 1-21. A homogenous magnetic field results in a narrow NMR spectrum

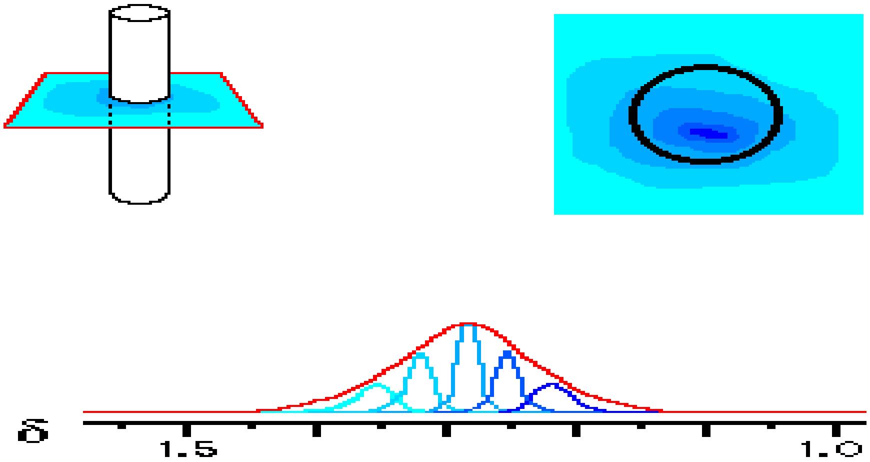

Figure 1-22. An inhomogeneous magnetic field results in a broader NMR spectrum

References

(1) Skoog, D. A., Holler, F. J., Crouch, S. R. *Principles of Instrumental Analysis*, 7th ed.; Saunders College Pub, 1998. Print: Philadelphia, 2017.

(2) Rabi, I.; Zacharias, J.; Millman, S.; Kusch, P. A New Method of Measuring Nuclear Magnetic Moment. *Phys. Rev.* **1938**, *53*, 318. https://doi.org/10.1103/PhysRev.53.318.

(3) Nuclear_Magnetic_Resonance_II @ chem.libretexts.org https://chem.libretexts.org/Core/Physical_and_Theoretical_Chemistry/Spectroscopy/Magnetic_Resonance_Spectroscopies/Nuclear_Magnetic_Resonance/Nuclear_Magnetic_Resonance_II.

(4) Levitt, M. H. *Spin Dynamics: Basics of Nuclear Magnetic Resonance*, 2nd ed.; 2008.

(5) Institute of Chemistry, The Hebrew University of Jerusalem. http://chem.ch.huji.ac.il/nmr/whatisnmr/whatisnmr.html.

(6) www.bu.edu/chemistry/files/cic/nmr/documents/CICNMR_basicconcepts.pdf.

(7) Hans J. Reich. *Relaxation in NMR Spectroscopy*; Wisconsin, 2017.

(8) Koch, P. *Spin-Lattice and Spin-Spin Relaxation Spin-Lattice Relaxation Mechanisms*; 2015.

(9) Grzesiek, S. *Notes on Relaxation and Dynamics*; Switzerland, 2003.

(10) Stevanato, G. Long-Lived States in Multi-Spin Systems. Ph.D. Dissertation, UNIVERSITY OF SOUTHAMPTON, 2015.

(11) Reich, H. J. *Relaxation in NMR Spectroscopy*; Wisconsin, 2017.

(12) Griswold, I. J.; Dahlquist, F. W. Bigger Is Better: Megadalton Protein NMR in Solution. *Nat. Struct. Biol.* **2002**, *9* (8), 567–568. https://doi.org/10.1038/nsb0802-567.

(13) Foster, M. P.; Mcelroy, C. A.; Amero, C. D. Solution NMR of Large Molecules and

Assemblies. *Biochemistry* **2008**, *46* (2), 331–340. https://doi.org/10.1021/bi0621314.

(14) Korb, J. P.; Vorapalawut, N.; Nicot, B.; Bryant, R. G. Relation and Correlation between NMR Relaxation Times, Diffusion Coefficients, and Viscosity of Heavy Crude Oils. *J. Phys. Chem. C* **2015**, *119* (43), 24439–24446. https://doi.org/10.1021/acs.jpcc.5b07510.

(15) Wand, A. J.; Ehrhardt, M. R.; Flynn, P. F. High-Resolution NMR of Encapsulated Proteins Dissolved in Low-Viscosity Fluids. *Proc. Natl. Acad. Sci. U. S. A.* **1998**, *95* (December), 15299–15302. https://doi.org/10.1073/pnas.95.26.15299.

(16) Brus, J.; Czernek, J.; Urbanova, M.; Kobera, L.; Jegorov, A. An Efficient 2D11B-11B Solid-State NMR Spectroscopy Strategy for Monitoring Covalent Self-Assembly of Boronic Acid-Derived Compounds: The Transformation and Unique Architecture of Bortezomib Molecules in the Solid State. *Phys. Chem. Chem. Phys.* **2017**, *19* (1), 487–495. https://doi.org/10.1039/c6cp06555d.

(17) Ashbrook, S. *The Power of Solid-State NMR*; Oxford, UK, 2009.

(18) Schanda, P.; Ernst, M. Studying Dynamics by Magic-Angle Spinning Solid-State NMR Spectroscopy : Principles and Applications to Biomolecules. **2017**, 1–46. https://doi.org/10.1016/j.pnmrs.2016.02.001.

(19) Charpentier, T. An Introduction to Solid State NMR and Its Interactions: Calculation of Solid-State NMR Parameters Using the GIPAW Method. From Tensor to NMR Spectra. **2009**.

(20) Laws, D. D.; Bitter, H.-M. L.; Jerschow, A. Solid-State NMR Spectroscopic Methods in Chemistry. *Angew. Chemie Int. Ed.* **2002**, *41* (17), 3096–3129. https://doi.org/10.1002/1521-3773(20020902)41:17<3096::AID-ANIE3096>3.0.CO;2-X.

(21) Tripon, C.; Aluas, M.; Filip, X.; Filip, C. Polarization Transfer from Remote Protons in 13C

CP/MAS. *J. Magn. Reson.* **2006**, *183* (1), 68–76. https://doi.org/10.1016/j.jmr.2006.07.019.

(22) Alia, A.; Ganapathy, S.; De Groot, H. J. M. Magic Angle Spinning (MAS) NMR: A New Tool to Study the Spatial and Electronic Structure of Photosynthetic Complexes. *Photosynth. Res.* **2009**, *102* (2–3), 415–425. https://doi.org/10.1007/s11120-009-9478-3.

(23) Samoson, A.; Tuherm, T.; Past, J. Ramped-Speed Cross Polarization MAS NMR. *J. Magn. Reson.* **2001**, *149* (2), 264–267. https://doi.org/10.1006/jmre.2001.2302.

(24) Taylor, R. E. 13C CP/MAS: Application to Glycine. *Concepts Magn. Reson. Part A Bridg. Educ. Res.* **2004**, *22* (2), 79–89. https://doi.org/10.1002/cmr.a.20015.

(25) A. Ramamoorthy. *NMR Spectroscopy of Biological Solids*, 1st ed.; 2005.

(26) Institute of Chemistry, The Hebrew University of Jerusalem. http://chem.ch.huji.ac.il/nmr/whatisnmr/whatisnmr.html.

(27) Joseph P. Hornak. *The Basic of NMR*; Rochester Institute of Technology, 2017.

(28) Shenoy, R. K.; Ramakrishna, J.; Jeffrey, K. R. A Solid State Pulsed NMR Spectrometer. *Pramana* **1980**, *14* (5), 363–371. https://doi.org/10.1007/BF02847843.

(29) Jungnickel J.L.;ForbesJ.W. Quantitative Measurement of Hydrogen Types by Intergrated Nuclear Magnetic Resonance Intensities. *Anal. Chem.* **1963**, 35.

(30) Staneva, J.; Denkova, P.; Todorova, M.; Evstatieva, L. Quantitative Analysis of Sesquiterpene Lactones in Extract of Arnica Montana L. by 1H NMR Spectroscopy. *J. Pharm. Biomed. Anal.* **2011**, *54* (1), 94–99. https://doi.org/10.1016/j.jpba.2010.08.018.

(31) Pieri, V.; Belancic, A.; Morales, S.; Stuppner, H. Identification and Quantification of Major Steviol Glycosides in Stevia Rebaudiana Purified Extracts by 1H NMR Spectroscopy. *J. Agric. Food Chem.* **2011**, *59* (9), 4378–4384. https://doi.org/10.1021/jf104922q.

(32) Yang, M.; Wang, J.; Kong, L. Quantitative Analysis of Four Major Diterpenoids in

Andrographis Paniculata by 1H NMR and Its Application for Quality Control of Commercial Preparations. *J. Pharm. Biomed. Anal.* **2012**, *70*, 87–93. https://doi.org/10.1016/j.jpba.2012.05.037.

(33) Agrahari, V.; Meng, J.; Purohit, S. S.; Oyler, N. A.; Youan, B. B. C. Real-Time Analysis of Tenofovir Release Kinetics Using Quantitative Phosphorus (31P) Nuclear Magnetic Resonance Spectroscopy. *J. Pharm. Sci.* **2017**, *106* (10), 3005–3015. https://doi.org/10.1016/j.xphs.2017.03.043.

(34) Levy, G. C.; Pehk, T.; Srinivasan, P. R. Quantitative15N NMR Spectroscopy. *Org. Magn. Reson.* **1980**, *14* (2), 129–132. https://doi.org/10.1002/mrc.1270140210.

(35) Okaru, A. O.; Brunner, T. S.; Ackermann, S. M.; Kuballa, T.; Walch, S. G.; Kohl-himmelseher, M.; Lachenmeier, D. W. Application of 19 F NMR Spectroscopy for Content Determination of Fluorinated Pharmaceuticals. **2017**. https://doi.org/10.1155/2017/9206297.

(36) Malz, F.; Jancke, H. Validation of Quantitative NMR. *J. Pharm. Biomed. Anal.* **2005**, *38*, 813–823. https://doi.org/10.1016/j.jpba.2005.01.043.

Part I. APPLICATIONS OF SOULTION STATE NMR SPECTROSCOPY IN PHARMACEUTICAL SCIENCES

Overview

Drug delivery is a method or a process for transporting a pharmaceutical compound to the part of the body where it's needed. Delivering the drug to the human body is an important component in pharmaceutical sciences. Several drug delivery systems have been investigated and utilized for a long period of time. These include oral, topical, and injection. Although these systemic administration methods are common and prevalent, they have some drawbacks. Some drugs may not travel easily through cells and tissues while others may lose their efficiency as they pass through the digestive system. Some drugs might cause side effects on the heathy tissues and organs. Moreover, some drugs may have solubility issues since they are partially soluble or not soluble at all in biological fluids.

In order to avoid these drawbacks, new drug delivery systems, which use a carrier based system as an alternative route for systemic administration system, are being developed. There are several types of carrier based systems and each type has its unique advantages and disadvantages. In this dissertation, we focused our studies on nano/micro formulations as a drug delivery system, specifically when the drug is encapsulated inside a nano/micro formulation. By going to this smart drug delivery system, several advantages can be gained. First, the physical properties of the drug, such as solubility, can be improved. The drug can be targeted where it can be delivered to the site where it is needed without passing through any organs. Hence, it will eliminate the side effects of the drug. Moreover, the release of the drug from nano/micro formulation can be controlled by designing the formulation in a certain way so we can have a slow release of the drug over a long period of time. Finally, using nano/micro formulation can allow the drug to be triggered in the presence of biomarkers. For example, when there is a cancer cell in human body, there would be a slight change in the pH around that cell. When the formulation is close to that cell, it will notice a pH change and then release the drug.

Studying the amount of the drug that is encapsulated inside these formulations and the rate of the drug release are critical steps in drug development. We explore the use of qNMR spectroscopic technique as a new tool to quantify the amount of the drug encapsulated and released.

NMR spectroscopy has become a well-established and widely popular technique among pharmaceutical scientists. Nowadays, NMR is routinely used in the identification of drugs, the determination of multicomponent drug compositions, isomeric composition determination, drug degradation studies, impurities level determination and elucidation of their structure, quality assessment as well as counterfeit drugs determination. In part I of this dissertation, several applications of NMR spectroscopy in pharmaceutical science will be presented and discussed.

In chapter 3, we investigate the potential of a real-time solution-state quantitative boron nuclear magnetic resonance (^{11}B qNMR) method for the analysis of boron-containing therapeutics molecules and formulations. Thus, a ^{11}B qNMR method was developed and validated for the quantification of bortezomib (BTZ).

In chapter 4, quantitative analysis of fluorinated drug (maraviroc) has been studied in order to quantify the amount of the drug released from microparticles into simulated biological fluids using fluorine (^{19}F) NMR Spectroscopy.

In chapter 5, NMR spectroscopy was implemented as a characterization tool for monitoring the reaction progression.

Objectives

The overall objectives of this part of the dissertation are:

1. To develop an accurate, alternative method to misleading drug release profiles in situ using NMR spectroscopy.
2. To validate the methods for ^{11}B and ^{19}F solution-state quantitative nuclear magnetic resonance (qNMR) for the real-time quantification of drug release.
3. To utilize ^{11}B NMR spectroscopy as a characterization tool for the reaction progression of the derivative of Phynelboronic acid (PBA).

Chapter 2 . QUANTITATIVE NMR SPECTROSCOPY

2.1 The basics of quantitative NMR (qNMR)

The first application of qNMR was in 1963 by Jungnickel and Forbes [1]and Hollis[2]. Jungnickel and Forbes determined the intramolecular proton ratio in different organic solvents while Hollis determined the amount of three components namely: aspirin, caffeine, and phenacetine in separate mixtures. In the past decades, qNMR was an efficient tool to quantify essentially organic chemicals and proton qNMR specifically was mostly commonly used. Nowadays, qNMR has become a well-established and widely popular technique among numerous fields such as the pharmaceutical and food industries [3–5]. The implementation of qNMR in several fields brings more complex molecules, which makes proton qNMR relatively challenging. Therefore, the usage of other active nuclei would be a suitable option to perform qNMR accurately[6–8].

Several advantages of qNMR allow this technique to compete among other chromatographic methods. For instance, the area of integrated signal peak is directly proportional to the number of nuclei contributing to the signal. It is a non-destructive and highly predictable technique in which no intensity calibration is required. It has short measuring times and fast acquisition. Sample preparation and handling are relatively easy. In NMR spectroscopy, the characterization of analytes in mixtures are routinely conducted without a need for prior isolation or purification.

The fundamental theory of qNMR is based on the direct proportional relationship between the signal response (integrated signal area) (Ix) for a compound X and the number of nuclei (Nx) producing the NMR signal[9].

The qNMR principle is governed by Equation (2-1), where Ks represents the NMR spectrometer constant. For a given NMR spectrum, Ks is identical for all resonance lines so the ratio of I_x and I_y is equivalent to the ratio of N_x and N_y Equation (2-2). The molar ratio of a given compound in a mixture of analytes can be determined using Equation (2-3), where n_x/n_y is the molar ratio of compound x and y. Hence, the amount fraction of compound X in a mixture of components m can be found by using Equation (2-4). An internal standard with known purity is required in order to determine the purity of compound x in a mixture using Equation (2-5), where p_x, M_x , and m_x are the purity, the molecular weight, and the mass of compound X respectively. Whereas p_{std}, M_{std} , and m_{std} are the purity, the molecular weight, and the mass of the standard.

$$I_x = K_s \times N_x \qquad (2\text{-}1)$$

$$\frac{I_x}{I_y} = \frac{N_x}{N_y} \qquad (2\text{-}2)$$

$$\frac{n_x}{n_y} = \frac{I_x}{I_y}\frac{N_y}{N_x} \qquad (2\text{-}3)$$

$$\frac{n_x}{\sum_{i=1}^{m} n_i} = \frac{I_x/N_x}{\sum_{i=1}^{m} I_i/N_i} \times 100\% \qquad (2\text{-}4)$$

$$\mathrm{P_x} = \frac{\mathrm{I_x}}{\mathrm{I_{std}}}\frac{\mathrm{N_{std}}}{\mathrm{N_x}}\frac{\mathrm{M_x}}{\mathrm{M_{std}}}\frac{\mathrm{m_{std}}}{\mathrm{m_x}}\mathrm{P_{std}} \qquad (2\text{-}5)$$

2.2 Validation of qNMR

2.2.1 Linearity and calibration curve

Linearity is described as the concentration range within which a given method provides a linear proportional relationship between NMR peaks' area under curve (AUC) and the molecules of interest concentrations. Frequently, calibration curve is established using different concentrations prepared by serial dilution of a standard. NMR peak's area under curve is then plotted in relation to the molecules of interest concentrations. The intercept, slope, and coefficient of determination (R^2) values are obtained by linear regression analysis.

2.2.2 Limit of quantification (LOQ) and limit of detection (LOD)

Limit of quantification is the lowest concentration of a substance in a sample that can be quantitatively identified precisely, whereas the limit of detection is the lowest amount of a substance that can be detected but not quantified. LOQ and LOD values can be determined using the numerical method based on Equations (2-6&7) or can be determined visually from the spectra. The LOQ and LOD values obtained from NMR are not as precise as other analytical technique such as HPLC, but it is still comparable.

$$\text{LOD} = \frac{3.3\times\sigma}{S} \qquad (2\text{-}6)$$

$$\text{LOQ} = \frac{10\times\sigma}{S} \qquad (2\text{-}7)$$

2.2.3 Specificity

Specificity is the method's ability to identify the analyte peak in the presence or absence of other contaminants. It is one of the first parameters that has to be evaluated to discover whether the method is appropriate or not.

2.2.4 Accuracy and Precision

The accuracy of an analytical method describes the closeness of measured values (sample values) to a true value (population value) with no systematic errors. Precision represents the agreement in the measurements when repeated with no random errors.

2.2.5 Robustness

The robustness of an analytical method measures the ability of the method to stay unaffected when certain parameters change. The robustness of qNMR method can be analyzed by varying different parameters such as: temperature, relaxation delay, magnetic field, pulse width, and proton decoupling. Results should be reported as relative standard error %RSE. According to ICH guidelines, for the robustness determination, %RSE should be less than 2%.

Chapter 3 . DIRECT AND REAL-TIME QUANTIFICATION OF BORTEZOMIB RELEASE FROM ALGINATE MICROPARTICLES USING BORON (^{11}B) NUCLEAR MAGNETIC RESONANCE SPECTROSCOPY

3.1 Introduction

Boron is an interesting element, which is located in group 13. It has atomic number five and an electronic configuration of [He] $2s^2$ $2p^1$. Boron is a metalloid, which has properties of a metal and nonmetal. Moreover, it is a neighbor for carbon in the periodic table. Because of the closeness to the carbon, boron and carbon share some useful similarities as well as important differences. Like carbon, boron can form a small size compound, which is suitable for approaching key binding sites. The most fascinating feature of boron from a chemist's point of view is that boron forms a very complex series of hydrides just as carbon does. It also can form four covalent bonds like carbon. Although boron and carbon share some noteworthy properties, there are remarkable differences between their properties. While boron hydrides are composed of clusters and cages, carbon hydrides are composed of chains and rings. Since boron is a metalloid, it behaves like a metal when it forms oxides and salts such as B_2O_3 and $B_2(SO_4)_3$ respectively. On the other hand, it behaves as a nonmetal when it forms acids such as boric acid $B(OH)_3$. Even though boron is a trivalent metal, it does not act like pure metal. It has a strong affinity to electrons due to the empty P_z orbital (Figure3-1)[10]. Hence, boron and most of its compounds are classified as electron-deficient, which results in unusual structures. Due to the unique charge distribution of boron compounds, they can form non-covalent bonds, which is an essential feature for biochemical reactions. Carbon compounds on the other hand typically form covalent bonds. Additionally, boron compounds show distinctive hydrophobic behavior, which makes them gain an interesting attraction to organic molecules.

Boron is produced mainly in Turkey and the United States. Until recently, the use of boron-containing compounds was mostly limited to common household appliances such as borosilicate glass, fiberglass textiles and insulation, washing powders, tile glazes and boric acid[11,12]. Recent decades have witnessed significant progress in boron chemistry, which have greatly expanded the use of boron-containing compounds from material to therapeutics. Researchers and the pharmaceutical industry are currently interested in boron compounds as an alternative to carbon compounds, which may lead to a new generation of boron drugs. Today, boron-based therapeutics are being widely investigated and represent an emerging new class of drug molecules. These molecules possess several biomedical applications as imaging agents for both optical and nuclear imaging, as well as therapeutic agents with anticancer, antiviral, antibacterial, antifungal and other disease-specific activities[13].

Boron-containing molecules have been overlooked as potential therapeutics primarily because of the misconception that the element boron is toxic. The “fear” of boron may have generated from boric acid, an ingredient for ant poison. However, it is well established that boric acid has an LD_{50} of 2660 mg/Kg (rat, oral), which resembles table salt 3000 mg/Kg (rat, oral)[14]. Moreover, boric acid is currently used as preservative in eye wash and vaginal creams[15]. Other studies have reported that boric acid inhibits the proliferation of prostate cancer cell lines, DU-145 and LNCaP, in a dose-dependent manner[16,17]. Furthermore, boron is known to be an essential plant nutrient that is present in many nuts, vegetables and fruits. This might explain the 0.3-4.2 mg daily intake of boron by Americans, according to Reiney et al[18]. Further evidence of the lack of an inherent toxicity of the element boron has been demonstrated by the recent FDA approval of boron containing drugs, such as Crisaborole (2016), Tavaborole (2014) and Bortezomib (2003). Many more boron-containing drugs are currently undergoing clinical trials and have demonstrated very promising safety and efficacy profiles. For example, Talabostat (PT100), a specific inhibitor of dipeptidyl peptidase-4 (DPP4), is a boron-containing compound currently in a phase III clinical trial for patients with stage IIIB/IV non-small-cell lung cancer who have failed a platinum-based chemotherapy regimen[19]. In a recently completed phase III clinical trial, Ixazomib, a peptide boronic acid derivatives, in combination with lenalidomide-dexamethasone significantly improved the overall survival rate and the progression-free survival in patients with relapsed/refractory multiple myeloma[20].

Boron neutron capture therapy (BNCT), a form of cancer radiation therapy, is gaining renewed attention due, in part, to significant progress in novel boron compounds and boron cluster chemistry[21]. For instance, boronophenylalanine (BPA)-based compounds have been investigated in clinical trials for the treatment of glioblastoma as well as head and neck tumors[22,23]. Another BNCT clinical trial has shown the potency of this therapy against malignant melanoma and the potential for in-hospital neutron irradiator (IHNI) to enable the delivery of BNCT in hospitals[24]. Furthermore, boron clusters such as closomers (derivatives of $B_{12}OH_{12}$) are being considered as novel BNCT delivery strategy[25]. Boron containing compounds are also receiving special interest for their potential in diagnosis and imaging[13].

In vitro, the study of drug release kinetics from nano/microformulations is an important step to quality control of drug delivery system. Due to the small size of nano/microformulations, it is very challenging to separate them from release media efficiently. Among other experimental methods, the dialysis method remains one of the most commonly used methods to study drug release kinetics from nano/microformulations[26]. The widespread use of the dialysis method is probably due to its simplicity, the lack of additional separation required between released drug and formulation debris, as well as the ability to analyze dialysis samples by, practically, any analytical method (UV-Vis, HPLC, LC-MS, NMR, etc.). Nonetheless, numerous studies have shed some light on the dialysis method's limitations for the accurate, real-time approximation of drug released from nano/microformulations[27,28]. Based on comparing the experimental results and simulation of dialysis method, the result of release quantification can be entirely misleading[29]. This limitation could be due to the two-step process involved in the dialysis method. To overcome this pitfall, the researchers thought that an ideal solution must be initiated and established for fast, accurate and real time method. Various strategies, including numerical deconvolution[28], optical techniques[30] and mathematical modeling[29] have previously been proposed. Facts discussed above motivated us to investigate the use of qNMR, as an alternative to the dialysis method, for the accurate and real-time quantification of boron contacting drugs release from microparticles formulation.

3.2 General Research Approach

In the current study, we investigate the potential of a real-time solution-state quantitative boron nuclear magnetic resonance (^{11}B qNMR) method for the analysis of boron-containing therapeutics molecules and formulations. Thus, a ^{11}B qNMR method was developed and validated for the quantification of bortezomib (BTZ) (Figure3-2)[31]. BTZ is the first proteasome inhibitor approved for use in human for the treatment of multiple myeloma[32]. The developed qNMR method was then used to study the real-time release of BTZ from a spray-dried alginate microparticle formulation. Furthermore, BTZ real-time release kinetics were compared to the traditional dialysis method, generally used for drug release studies in micro/nanoformulations. With the expansion in boron-focused pharmaceutical research, along with the expected approval of new boron containing drugs, this study may provide an additional tool for the analysis of boron-based pharmaceutical formulations/compounds. This study may also contribute to the growing discussion on the use and validity of dialysis methods for evaluating drug release kinetics. In fact, among other experimental methods, the dialysis method remains one of the most commonly used methods to study drug release kinetics from nano/microformulations[26].

3.3 Quantitative NMR theory and pharmaceutical applications

Nuclear magnetic resonance (NMR) spectroscopy is a substantial, powerful, and broadly used form of spectroscopy in analytical method development[33,34]. Over the past decades, NMR has proved to be a remarkably successful analytical technique for structural determination. In contrast to other spectroscopic methods, NMR spectroscopy is a non-destructive and highly predictable technique in which no intensity calibration is required. It can have short measuring times, and sample preparation and handling are relatively easy. Furthermore, the characterization of analyte mixtures can be routinely conducted in NMR spectroscopy without a need for prior isolation or purification. The fundamental theory of qNMR is based on the direct proportional relationship between the signal response (integrated signal area) (I_x) for a compound X and the number of nuclei (N_x) producing the NMR signal[9].

$$I_x = K_s \times N_x \qquad (3\text{-}1)$$

qNMR is governed by equation (3-1), where K_s represents the NMR spectrometer constant. For a given NMR spectrum, K_s is identical for all resonances lines, which allows the determination of the mole fraction of a given compound in a mixture of analytes[35].

Owing to the wide range of possible applications, the remarkable accuracy, robustness and less experimental hurdles, qNMR is becoming a well-established and widely popular technique among pharmaceutical scientists. Nowadays, qNMR is routinely used in the identification of drugs, the determination of multicomponent drugs composition, isomeric composition determination, drug degradation studies, impurities level determination and elucidation of their structure, quality assessment as well as the counterfeit drugs determination[36–39]. Commonly qNMR nuclei used in pharmaceutical applications are ^{1}H and ^{13}C[40,41]. This is partly due to the high proportion of carbon and hydrogen atoms in natural and synthetic compounds, compared to other NMR active atoms. Other studies have investigated NMR active heteroatoms such as ^{19}F, ^{31}P and ^{15}N in the quantification and characterization of therapeutic molecules[6,7,42]. In this study, we investigate the use of ^{11}B qNMR for the characterization and quantification of boron-containing drugs. Boron has two naturally occurring isotopes (^{10}B [20%] and ^{11}B [80%]) and both are detectable by NMR with spins values greater than 1/2. In fact, ^{11}B has a spin of 3/2, a quadrupole moment of 4.06 fm^2 and a relative gyromagnetic ratio of 0.32 (compared to ^{1}H). ^{10}B has a spin value of 3 a quadrupole moment of 8.46 fm^2, and a relative gyromagnetic ratio of 0.107[43]. The low quadrupole moment of ^{11}B makes it a better nuclei for qNMR of non-enriched samples than ^{10}B. In fact, ^{11}B has a higher receptivity (sensitivity relative to ^{1}H) (0.13) and yields sharper signals compared to ^{10}B (0.0039)[44–46]. One major advantage of ^{11}B qNMR is the higher natural abundance of ^{11}B (80%) compared to ^{13}C (1.1%)[4743]. In addition, ^{11}B qNMR offers the advantage of a wider range of chemical shift (-120 to 90 ppm) compared to ^{1}H. In fact, ^{1}H has a narrow range of chemical shift (typically 0 to 15 ppm), which often leads to signal overlap and increased spectral complexity due to coupling of neighboring protons[48] (Figure3-3). Furthermore, due to the low density of boron atoms in currently approved boron containing therapeutic molecules (one B atom/molecule), ^{11}B qNMR can avoid interference from homonuclear coupling as well as signal overlap[49]. Moreover, because of the lack of boron atoms in solvents typically used in pharmaceutical applications, ^{11}B qNMR experiments can virtually be performed in any solvent without the risk of solvent signal interference, given that the solubility and stability are established in those solvents. This versatility in ^{11}B qNMR solvent choice is more economically favorable as this could avoid the use of special and/or expensive solvents.

3.4 Material and methods

3.4.1 Reagents

Bortezomib was obtained from ZhongShuo Pharmaceutical Technology Development Co.,Ltd. (Beijing, China). Boron trifluoride diethyl etherate ($BF_3.OEt_2$), acetonitrile, methanol, ethanol, acetone, dimethyl sulfoxide (DMSO), chloroform-d ($CDCl_3$), boric acid, 4-propylphenylboronic acid (PBA) and alginic acid sodium salt (from brown algae, medium viscosity) were purchased from Sigma-Aldrich (St. Louis, MO, USA). Deionized water (DI water) was obtained through a Millipore Milli-Q water purification system (Millipore Corp., Danvers, MA) and all other chemicals were of analytical grades and used as obtained from suppliers.

3.4.2 ^{11}B qNMR method development

In this study, the integrated ^{11}B qNMR peak area of BTZ was of interest in order to accurately quantify the amount of drug. ^{11}B qNMR spectroscopy was carried out on a Varian 400 MHz spectrometer (Palo Alto, CA, USA) with a Varian 2-channel probe. VnmrJ software (version 4.2A) was used for data acquisition and processing. The ^{11}B spectra were acquired at frequency 128.268MHz. Wilmad® quartz NMR tubes (600 MHz, diam. 5 mm, L7 in, Sigma-Aldrich, St. Louis, MO, USA) were used for spectral acquisition in order to eliminate the contribution of borosilicate glass in the spectrum. An inversion recovery experiment was performed to optimize the spin-lattice relaxation time, which was found to be 0.4s. We found that T1 is around 0.08s Usually, most NMR active nuclei are fully relaxed after 5 times of T1[35]. According to the Equation (3-2) below, the linewidth of the NMR signal is directly dependent on T2* (the apparent spin-spin relaxation time). Large molecules such as a polymer tend to have very small T2 values.

$$Line\ width = (\pi T_2 *)^{-1} \qquad (3\text{-}2)$$

Therefore, it is expected that the integrated peak for a polymeric formulation of BTZ will be very broad in comparison to free BTZ (in solution), due to slow tumbling[6]. Shimming was applied to each sample to maintain the same linewidth in each spectrum. For all ^{11}B NMR experiments, the number of accumulated transients, the pulse width and the complex point were 512 and 90° (11µs), 2048 respectively. While the spectral width and FID acquisition time were 2565.7 and 0.080s. The total acquisition time for each spectrum was around five minutes. The sample spinning frequency was 20 Hz, which is a typical way of acquiring NMR spectra to improve the resolution, with no observable sidebands. Neither zero-filling, window function nor proton decoupling were applied. Experiments were performed in triplicate and average integrated peak area values were determined. $BF_3.OEt_2$ (15% in $CDCl_3$) was used as ^{11}B q-NMR external standard and its chemical shift ($\delta \sim 0$ ppm) and peak resolution were assessed prior to any BTZ spectral acquisition. Typically, 650 µL of BTZ sample are placed in the quartz NMR tubes and ^{11}B NMR experiments are conducted at 37ºC using a standard VT, unless specified otherwise. Baseline correction, phase adjustment, and integral calculation were carried out manually using MestReNova Lite (11.02.2, Escondido, CA, USA) and Matlab (2013-rdp, Natick, MA, USA).

Following a screening in DI water, acetonitrile, methanol, ethanol, acetone, dimethyl sulfoxide (DMSO) and chloroform-d ($CDCl_3$), methanol was selected as the optimal solvent for BTZ ^{11}B qNMR method development and validation. The solvent screening was conducted by assessing the ^{11}B spectrum resolution of BTZ samples (50 mg/ml) of BTZ prepared in these solvents. The solubility of BTZ in the screening solvents and the intensity of any eventual boric acid contaminant's ^{11}B NMR peak were also considered as critical parameters in the optimal solvent selection process. BTZ samples were prepared in methanol at concentrations ranging from

0.19 to 50 mg/ml (0.49 to 130.15 mM) by serial dilutions of a stock solution (50 mg/ml). When not in use, samples were sealed and kept under refrigeration at – 20 ºC.

3.5 Validation of ^{11}B qNMR Method

^{11}B qNMR method was validated according to the International Conference on Harmonization (ICH) guidelines Q2(R1)[50]. Thus, several parameters (linearity, LOD, LOQ, specificity, precision, accuracy and robustness) were evaluated and the statistical variations within ^{11}B qNMR peak areas and/or BTZ concentrations were presented as percent relative standard error (%RSE).), as expressed in the Equation below.

$$\%\mathrm{RSE} = \frac{s}{\bar{x}\sqrt{n}} \times 100 \qquad (3\text{-}3)$$

3.5.1 Linearity and calibration curve: Linearity is described as the concentration range within which the ^{11}B qNMR method provides a linear proportional relationship between ^{11}B NMR peaks' area under curve (AUC) and BTZ concentrations. BTZ calibration curve was established using nine different concentrations (0.19- 50 mg/ml) prepared by serial dilution of a standard (50 mg/ml) in methanol. ^{11}B NMR peak's area under curve was then plotted in relation to BTZ concentrations. The intercept, slope, and coefficient of determination (R^2) values were obtained by linear regression analysis in GraphPad (version 6.0, La Jolla, CA, USA).

3.5.2 Limit of quantification (LOQ) and limit of detection (LOD): Limit of quantification is the lowest concentration of a substance in a sample that can be quantitatively identified precisely, whereas the limit of detection is the lowest amount of a substance that can be detected but not quantified. LOQ and LOD values were determined using the numerical method based on Equations (3-4&5). The standard deviation of the response [σ] and the slope of the calibration curve [S] were obtained from the linear regression performed in GraphPad (version 6.0, La Jolla, CA, USA).

$$\text{LOD} = \frac{3.3\times\sigma}{S} \qquad (3\text{-}4)$$

$$\text{LOQ} = \frac{10\times\sigma}{S} \qquad (3\text{-}5)$$

3.5.3 Specificity: Specificity is the method's ability to identify the analyte peak in the presence or absence of other contaminants. In this study, ^{11}B qNMR method's specificity was tested in the presence of boric acid and 4-propylphenylboronic acid (PBA). Thus, BTZ's ^{11}B qNMR spectrum was acquired and compared to spectra containing the contaminants. A method specific to BTZ should clearly distinguish the drug from the contaminants, in term of chemical shift values.

3.5.4 Accuracy and Precision: The accuracy of an analytical method describes the closeness of measured values (sample values) to a true value (population value) with no systematic errors. Precision represents the agreement in the measurements when repeated with no random errors. The accuracy of ^{11}B qNMR method was evaluated using four (4) quality control (QC) samples (3, 5, 11 and16 mg/ml) and results were expressed as percent mean recovery and percent relative standard error (%RSE). The same QC samples were utilized to assess the intra-day and inter-day precision of ^{11}B qNMR and results were reported as %RSE. Each QC sample was analyzed in triplicate (n=3) throughout the accuracy and precision study.

3.5.5 Robustness: The robustness of an analytical method measures the ability of the method to stay unaffected when certain parameters change. The robustness of ^{11}B qNMR method was analyzed by varying four (4) parameters including: temperature (ºC), relaxation delay (s), pulse width (µs), and proton decoupling. Each experiment was performed in triplicate and results are reported as %RSE. For the robustness determination, %RSE should be less than 2%.

3.6 Alginate microparticles preparation

Alginate microparticle formulation of BTZ was prepared according to the method of Meng et al., with minor modifications[51]. Thus, alginic acid sodium salt and BTZ were added to 40 ml of a solution of 15% methanol (in DI water, pH 7.2) at a ratio of 4:1. The mixture was stirred at room temperature (25 ºC) until both the drug and polymer were completely dissolved. The solution was then spray-dried on a Buchi Mini Spray Dryer, Model 290 (Buchi Laboratoriums - Technik AG, Flawil, Switzerland). The spray dryer inlet temperature was T=120 ºC, the outlet temperature at the collector was 30 ºC, the aspirator was maintained at 85%, the pump rate was 10% and the nozzle cleaner was set at 7. Dried microparticles powder was collected from the instrument and stored at 4 ºC for further analysis.

3.7 Physico-chemical characterization

3.7.1 Size and surface charge: BTZ microparticles size and zeta potential (ζ-potential) measurements were conducted by dynamic light scattering (DLS) on Malvern instrument 3600 Zetasizer Nano (Worcestershire, UK). Practically, 1 ml of sample suspension (in DI water) was prepared in disposable size measurement cuvette and briefly sonicated (20 s) by bath sonication (Qsonica LLC, Newtown, CT, USA). Surface charge density (ζ-potential) measurements were conducted by transferring samples into DTS 1070 zetasizer disposable folded capillary cells (Malvern Instruments, Northampton, MA, USA). Size and ζ-potential cuvettes were then placed in the cell area and experiments were performed at 25°C on the Zetasizer instrument. Data acquisition and analysis were conducted using Zetasizer software (version 6.01, Worcestershire, UK). Prior to any DLS measurements, the instrument was calibrated using nanosphere™ size standards (60.0±4 nm) and ζ-potential transfer standards (−42.0±4.2 mV), obtained from Malvern Instruments (Northampton, MA, USA).

3.7.2 Fourier transform infrared spectroscopy (FTIR): IR spectroscopy was conducted following published methods[52,53]. IR spectra were acquired on Nicolet IS10 FTIR instrument (Thermo Fisher Scientific, Madison, WI, USA) equipped with a Zinc selenide (ZnSe) crystal. The instrument was used in the Attenuated Total Reflectance (ATR) mode. A resolution of 4 cm^{-1} and a sample scan of 228 were fixed as basic acquisition parameters. Transmittance IR spectra were acquired between 4000 and 650 cm^{-1}. For better spectral resolution, all samples were allowed to make intimate contact with the ATR ZnSe crystal's surface by pressing them with a built-in pressure clamp. FTIR spectra were collected and analyzed with OMNIC Specta Software (Thermo Fisher Scientific, Madison, WI, USA). Typically, the average IR spectrum acquisition time was 6 minutes.

3.7.3 Scanning electron microscopy (SEM): To analyze BTZ microparticles' morphology, SEM imaging was conducted on a Field-Emission Environmental SEM Philips XL30 instrument (Hillsboro, OR, USA). Thus, a small amount of dried microparticles was sprayed onto a stub covered with an adhesive conductive carbon tab. Excess material was removed using a paintbrush and the sample was sputter coated with a thin layer of gold. Images were acquired at an accelerating voltage of 5 kV[6].

3.7.4 Drug loading (%LD): We have previously explored the use of NMR for drug encapsulation and loading determination[52]. In this study, BTZ percent loading (w/w) into alginate microparticles was determined by ^{11}B qNMR. Briefly, 15 mg of alginate microparticles are dispersed in 600 µL of methanol and the mixture is sonicated for 5 minutes and stored at 4 ºC for 24 h, to allow a complete release of BTZ from the microparticle formulation. The mixture is further transferred into a quartz NMR tube and ^{11}B NMR experiment is performed on a Varian 400 MHz spectrometer (Palo Alto, CA, USA), as explained above. The experiment is conducted in triplicate and the average BTZ concentration is determined from a calibration curve, based on the ^{11}B NMR spectrum's area under curve (AUC). Percent %LD is then determined through Equation (3-6).

$$\%\mathrm{LD} = \frac{\text{Average BTZ concentration (mg/ml)}}{\text{Alginate microparticle concentration (mg/ml)}} \times 100 \qquad (3\text{-}6)$$

3.8 Drug release kinetics

One potential benefit of the ^{11}B qNMR method is accurate and real-time quantification of boron-containing drugs' release from nano/microparticles formulations. In this study, BTZ real-time release from an alginate microparticle formulation was assessed by ^{11}B qNMR and the release profile was compared to a control condition performed in a dialysis bag. Briefly, a homogenous dispersion of alginate microparticles (25 mg/ml) was prepared in methanol and immediately transferred into a quartz NMR tube. Time dependent BTZ release (% drug release) was further determined by acquiring ^{11}B qNMR spectra at predetermined time points (0.5, 1, 2, 4, 8, 16 and 24 h), at 37 ºC. In a separate experiment, an alginate microparticle sample was prepared at 25 mg/ml in methanol and immediately placed into a dialysis bag (Spectra/Por® Float-A-Lyzer G2, MWCO 8-10 kD; Spectrum Laboratories, Inc., Rancho Dominguez, CA, USA). The dialysis tube was further immersed into a methanol bath (15 ml), and the mixture was placed in a thermostatic water bath at 37 ºC, under shaking at 60 rpm. Sample aliquots (1 ml) were collected at predetermined time points (0.5, 1, 2, 4, 8, 16 and 24 h) from the receiver chamber and BTZ concentration was determined by ^{1}B qNMR. The sink condition was maintained by adding 1 ml of free methanol solution in the outer dialysis compartment following each sample collection. All experiments were conducted in triplicate (n=3) and the time dependent BTZ release (% drug release) curve was determined from the calibration curve (Figure 3-4), based on the ^{11}B NMR spectrum's area under curve (AUC).

The model-independent mathematical approach was applied to assess the similarity or differences of BTZ release profiles between the dialysis and NRR tubes. Thus, a pair-wise comparison of both release curves was conducted using the US FDA similarity (f_2) and dissimilarity (f_1) factors. f_1 measures the percent error while f_2 measures the sum-squared error between a test and reference compound's overall time points[52]. According to FDA guidelines, f_1 values lower than 15 (0-15) and f_2 values higher than 50 (50-100) support the similarity of two dissolution or release profiles. Consequently, f_1 and f_2 values deviating from those ranges support a significant difference between two dissolution or drug release profiles[54].

$$f_1 = \left(\frac{\left[\sum_{j=1}^{n} \left|R_j - T_j\right|\right]}{\left[\sum_{j=1}^{n} R_j\right]}\right) \times 100 \qquad (3\text{-}7)$$

$$f_2 = 50 \times \log\left\{\left[1 + \left(\frac{1}{n}\right)\sum_{j=1}^{n}\left|R_j - T_j\right|^2\right]^{-0.5} \times 100\right\} \qquad (3\text{-}8)$$

In Equations (3-7&8), n represents the sampling number, R and T are the percent dissolved of the reference and test products, respectively, at each time j. Furthermore, to elucidate BTZ drug release mechanism from alginate microparticles, various release kinetics models including zero order, first order, Weibull, Korsmeyer-Peppas, Higuchi, Hixson–Crowell, Hopfenberg and Baker–Lonsdale, were fitted to the release profiles. The appropriate (optimal) release kinetic model was selected based on higher coefficient of determination (R^2) and lower Akaike Information Criterion (AIC) values[54]. AIC value is typically used to measure the goodness of fit between different models, based on maximum likelihood[55,56].

3.9 Results and discussion

3.9.1 Solvent screening for 11B qNMR method development

Figure 3-4 is a summary of BTZ ^{11}B NMR spectra acquired in various screening solvents. Solvents were screened in order to identify the optimal solvent capable of solubilizing BTZ and yielding a single, not noisy, and well-resolved ^{11}B NMR peak. It was observed that BTZ (non-mannitol formulated) does not dissolve in DI water, acetonitrile and acetone. The lack of solubility in water could be due to BTZ's hydrophobicity (logP = 1.53). Furthermore, ^{11}B NMR of BTZ dispersion in those solvents did not yield any well-resolved detectable NMR signal.

Although BTZ was completely dissolved in DMSO, $CDCl_3$ and ethanol, the resulting ^{11}B NMR signals were very broad and noisy. In addition, a strong boric acid peak (δ = 19 ppm) was observed in ^{11}B NMR signal acquired in ethanol indicating possible reactivity with the solvent. Conversely, methanol was found to, not only, completely dissolve BTZ, but yielded a symmetrical, well-resolved and detectable ^{11}B NMR signal with almost no boric acid peak. The BTZ chemical shift in methanol was δ = 13 ppm. Similar findings were also reported by Tabrizi et al. following BTZ screening in deuterated water (D_2O), saline solution, methanol, acetonitrile plus 20% D_2O and DMSO[57]. BTZ signal was well resolved in methanol probably due to the solvent's lower viscosity (0.545 mPa.s) compared to that of DMSO (2.0 mP.s), ethanol (1.074 mPa.s) and $CDCl_3$ (0.57 mPa.s). In fact, it is well known that as the NMR solvent's viscosity increases, the molecular tumbling slows down and a line broadening occurs in the spectrum due to the quadrupole splitting (as observed most readily in the spectrum of BTZ in DMSO)[58,59]. Therefore, a less viscous solvent, such as methanol, that favors a faster correlation time would be preferred for these kinds of studies. In addition to the viscosity effect, BTZ peak broadening could be due to the formation of a 6-membered heterocyclic ring known as boroxine. Boronic acid containing molecules such as BTZ are well known to self-condensate and easily undergo boroxine formation, which substantially reduces molecular tumbling and leads to NMR peak broadening[60–64]. Boroxine formation in BTZ is perhaps more favorable in hydrophobic solvents and that may also explain the difference in BTZ peak resolution between $CDCl_3$ and Methanol, although both solvents have similar viscosity values[64].

Furthermore, it was shown that BTZ boroxine ring formation induces several differences in the spatial orientation of the three boron atoms involved in the self-condensation. In fact, instead of the generally accepted planar structure of the boroxine moiety, the boroxine ring was found to be consisting of either two boron atoms in trigonal configuration and one in tetrahedral coordination and/or two boron atoms in the tetrahedral configuration accompanied by one boron atom in a trigonal geometry. These differences in the boron spatial orientation lead to changes in the quadrupolar constants and ^{11}B NMR chemical shift, which in turn, could lead to peak broadening[51]. Therefore, all subsequent ^{11}B NMR spectral acquisitions were conducted in methanol. Nonetheless, ^{11}B NMR signals of BTZ acquired in methanol were slightly broad. The broadening of ^{11}B NMR signals was previously shown to be due to the large quadrupolar moment of boron (^{11}B) nuclei[61].

3.9.2 Linearity, detection and quantification limits

The ^{11}B qNMR method was developed and validated based on ICH Q2(R1) guidelines[50]. The method was linear in the concentration range tested (0.19- 50 mg/ml or 0.49-130.14 mM) and the coefficient of determination (R^2) was 0.9995 (Figure3-5). The method's LOD and LOQ were 0.72 mg/ml (1.87 mM) and 2.17 mg/ml (5.65 mM), respectively. These values were significantly higher than values reported for UV spectroscopy (LOD = 0.099 μg/ml and LOQ = 0.301 μg/ml)[65] and HPLC (LOD = 0.084 μg/ml and LOQ = 0.25 μg/ml)[62] methods of BTZ. Nonetheless, the LOD and LOQ values obtained were consistent with the range of other qNMR methods reported in the field of pharmaceutical research[63,64]. In general, qNMR methods have a lower sensitivity compared to other analytical methods such as UV spectroscopy and HPLC. In fact, higher LOD and LOQ values have previously been reported for ^{1}H qNMR[66], ^{31}P qNMR[6] and ^{19}F qNMR[42] methods compared to their respective HPLC methods[67–69]. Nonetheless, following the intravenous administration of a 1.3 mg/m^2 dose, the median estimated maximum plasma concentration of Bortezomib was 509 ng/mL (ranging from109 to 1300 ng/mL)[70]. Therefore, the current ^{11}B qNMR method will only be relevant for the detection of Bortezomib plasma concentration in certain patients with high plasma concentration of the drug (between 720 ng/ml and 1300 ng/mL) and might not be applicable to the patients population with lower plasma centration of the drug (between 109 ng/mL and 720 ng/ml).

3.9.3 Specificity

The ^{11}B qNMR method was found to be specific for BTZ. In fact, boric acid and PBA ^{11}B NMR chemical shifts did not interfere with BTZ's. Thus, BTZ's ^{11}B NMR peak was symmetrical, had a consistent chemical shift value ($\delta = 13$ ppm) and could accurately be quantified even in the presence of other boron containing contaminants. While boric acid spectrum showed a single peak, it was observed that PBA's ^{11}B NMR spectrum shows two distinctive peaks. One of those peaks ($\delta \sim 30$ ppm) was attributed to the boron atom in PBA while the chemical shift at ~ 19 ppm was assigned to boric acid. The presence of boric acid in PBA could be the result of a partial degradation of PBA or a contamination from the supplier. Figure 3-6 summarizes the results of ^{11}B qNMR method specificity study.

3.9.4 Precision and accuracy

The precision and accuracy results show that ^{11}B qNMR method of BTZ is accurate with all percent mean recovery values within 100 ± 10% and %RSE values <2%, for both intra-day and inter-day recovery studies (Table 3-1) and (Figure3-7). The method was also precise and %RSE values for intra-day and inter-day precision analysis were <2%, for all four QC samples tested (Table 3-2). These results were consistent with ICH guidelines and confirmed the closeness of agreement (reproducibility) between the AUC values of ^{11}B qNMR spectra for each QC sample.

3.9.5 Robustness

The ^{11}B qNMR method's robustness was assessed by varying critical NMR instrumental parameters. According to their previous work on qNMR method validation, Malz et al. showed that changes in various NMR parameters can significantly influence the chemical shift, the signal-to-noise ratio or signal intensity. In this study, the ^{11}B qNMR method was robust and was not affected by stepwise changes in temperature, relaxation delay, pulse width and proton decoupling. Method robustness results, summarized in (Table 3-3) and (Figures 3-8, 10, 11), show that all %RSE were < 2%.

3.10 Application of ^{11}B qNMR method for the real-time *in vitro* release of BTZ from alginate microparticles formulation.

3.10.1 BTZ/Alg microparticle formulation development and characterization:

Following the preparation of spray-dried BTZ/Alg microparticles, average particle size and ζ-potential measurements were conducted on the Zetasizer Nano instrument. Figure 3-12 (A&B) summarizes the size and surface charge density analysis of the microparticle formulation. Although it is routinely used for nanomaterial characterization, the Zetasizer Nano instrument is suitable for microparticles surface charge density and size measurements (≤ 10 μm)[71]. BTZ/Alg microparticles' average particle size was 2.36 ± 0.19 μm and the polydispersity index (PDI) was 0.253. These values were consistent with typical average particle size and PDI values observed in spray drying[72]. PDI values lower than 0.05 are characteristic of monodispersed samples[73]. Moreover, PDI values ranging from 0.1 to 0.7 represent nearly monodisperse preparations, whereas PDI > 0.7 suggest broadly distributed samples[74]. Thus, the BTZ/Alg microparticle formulation was nearly monodisperse. The microparticles were negatively charged and the average ζ-potential was -57.1 ± 2.2 mV. The strong negative charge is probably due to the carboxylate group of alginic acid sodium salt, which is expected to be fully deprotonated (ionized) in neutral pH conditions (alginic acid's pKa ~ 3.4 to 4.4)[75]. The SEM image (Figure 3-12 C) revealed that individual BTZ/Alg microparticles are spherical in shape with varying size and morphology. Nonetheless, the average particle size was consistent with the Zetasizer measurements.

BTZ was successfully encapsulated inside the alginate microparticles and the %LD, determined by ^{11}B qNMR, was 30 ± 1.76% w/w. Furthermore, FTIR spectra (Figure 3-13) confirmed the presence of both the polymer and drug in the microparticle formulation. In fact, the BTZ/Alg microparticle IR spectrum showed features between 2800 cm^{-1} and 2950 cm^{-1} consistent with the symmetric and asymmetric stretch mode of CH_2 in BTZ[53]. Bands at 1600 cm^{-1}, 1650 cm^{-1}, 1500 cm^{-1} and 700 cm^{-1} in BTZ/Alg microparticle IR spectrum were attributed to amide I, amide II, the B-OH bond and the aromatic ring of BTZ, respectively[52,76]. The broad band between 3100 cm^{-1} and 3700 cm^{-1} in BTZ/Alg microparticle IR spectrum was assigned to OH stretch in sodium alginate[52]. Likewise, the strong bands at 1010 cm^{-1} and 1400 cm^{-1} in BTZ/Alg microparticle IR spectrum were due to C–O and C–C stretching vibrations and C–OH deformation vibrations in sodium alginate[77]. All of these features observed in BTZ/Alg microparticle IR spectrum were consistent with the bands observed in Alg and BTZ IR spectra.

3.10.2 BTZ in vitro drug release and kinetic modeling

The drug release profiles from BTZ/Alg microparticles (Figure 3-14) showed distinctive differences between the direct ^{11}B qNMR (Figure3-15) and the dialysis methods (Figure 3-16). First, a significant burst release of BTZ was observed in the case of direct ^{11}B qNMR measurements in the NMR tube, which was suppressed in the dialysis method. Thus, the dialysis method might not be able to accurately approximate the early burst release profile from fast dissolving (degrading) nano/microparticles drug delivery systems. Secondly, an equilibrium (steady state) in BTZ release profile was achieved in the ^{11}B qNMR method at ~ 4 h, while it took twice as long (~ 8 h) to reach an equilibrium in the dialysis method. That is, the dialysis method might not be accurately approximating the rate of drug release from nano/microparticles drug delivery systems. Thirdly, after the steady states are reached (> 8 h), a significant difference in the total amount of BTZ released was observed between both methods. Overall, a more than 20% difference in the total amount of BTZ released was observed at equilibrium. Moreover, for each time point, the dialysis method consistently underestimated the total amount of BTZ released from BTZ/Alg microparticles. The significant difference between both drug release profiles was also supported by the model-independent method using the FDA dissimilarity (f_2 = 13.85) and similarity ($f_1 = 54.45$) factors. According to the FDA guideline, f_1 values lower than 15 (0-15) and f_2 values higher than 50 (50-100) show the similarity of two release profiles[54]. The differences observed between the dialysis and direct ^{11}B qNMR methods could be due to the two-step process required for drug molecules to partition into the receiver compartment in the dialysis method. In fact, unlike in the direct ^{11}B qNMR method, the partition of BTZ drug molecules into the dialysis receiver compartment is a consequence of the release from the BTZ/Alg microparticle formulation into the inner dialysis chamber followed by a diffusion through the dialysis membrane pores. Because of this inherent diffusion barrier, there is constantly a discrepancy in drug concentrations across the dialysis membrane. Similar observations were reported using ^{1}H qNMR and ^{31}P qNMR[6,35].

Due to the limitation mentioned above, the dialysis method could complicate data interpretation and lead to incorrect conclusions regarding the formulation boron based drug release kinetics[29]. In fact, in addition to differences related to the amount of BTZ released in both methods, both methods yielded different mechanism and kinetics of drug release (Table 3-4). The drug release profile from the direct ^{11}B qNMR method was better explained by the Baker–Lonsdale kinetic model (R^2 = 0.98 and AIC = 39.661). The Baker–Lonsdale kinetic model was initially developed from the Higuchi kinetic model and describes the controlled drug release from a spherical matrix. Although the Hixson–Crowell kinetic model also fitted BTZ drug release profile from the direct ^{11}B qNMR method with an identical coefficient of determination (R^2 = 0.98), this model had a significantly higher AIC value (AIC = 55.6) and was therefore rejected. Furthermore, the drug release profile from the dialysis method was better explained by the Hopfenberg kinetic model (R^2 = 0.999 and AIC = 19.031). Traditionally, the Hopfenberg kinetic model has been used to explain drug release profiles from matrix eroding drug particles[52]. More specifically, Hopfenberg kinetic model assumes matrix erosion to be the rate-limiting step of drug release, instead of time dependent diffusional resistance (internal or external) to the eroding matrix[78].

3.11 Conclusion

In this study, we have developed a ^{11}B qNMR method for the simple, rapid, precise and real time quantification of bortezomib (BTZ) drug release from an alginate microparticle formulation. The ^{11}B qNMR method was validated according to the ICH Q2R(1) guidelines and was linear (up to 130.14 mM), specific for BTZ, precise, accurate and robust. The LOD and LOQ values were 1.87 mM and 5.65 mM, respectively, and were consistent with the range of other quantitative NMR (qNMR) methods. When compared to the traditional, indirect dialysis method of *in vitro* drug release analysis, the direct ^{11}B qNMR method was found to be better at:

(1) precisely quantifying the early burst released from the microparticle formulation

(2) accurately determining the rate of drug release from the microparticle formulation as well as the time required to attain the equilibrium state

(3) accurately quantifying the total amount of drug released at each time point.

Furthermore, the direct ^{11}B qNMR method was found to be relatively easy to setup and less time consuming, compared to the dialysis method. As preconceived notions of boron toxicity begin to dissipate and more boron containing drugs continue to be approved for therapy, diagnosis or imaging, boron specific analytical methods, such as ^{11}B qNMR, will find more common acceptance, allowing additional applications including structure elucidation, drug release and dissolution, stability testing, degradation studies, impurity identifications and counterfeit determination.

Some of the major limitations of the current ^{11}B qNMR method study include the relatively high LOD value (720 ng/ml) which makes the method only clinically relevant to a portion of the patients population with high plasma concentration of BTZ (between 720 ng/ml and 1300 ng/mL). In addition, due to solubility limitations, peak resolution and spectra broadening observed with other solvents, the non-mannitol formulated BTZ's ^{11}B qNMR method development was not applicable to other bio-relevant solvents such as phosphate buffer solution, simulated gastric fluids and saline solutions. Follow up studies will investigate the suitability of a ^{11}B qNMR method for the clinically available mannitol formulation of BTZ in these bio-relevant solvents. These future studies will also include the XRPD, ^{11}B Solid State NMR (SSNMR) and the atomic force microscopy characterization of a modified, stimuli-responsive BTZ/Alg microparticles drug delivery system.

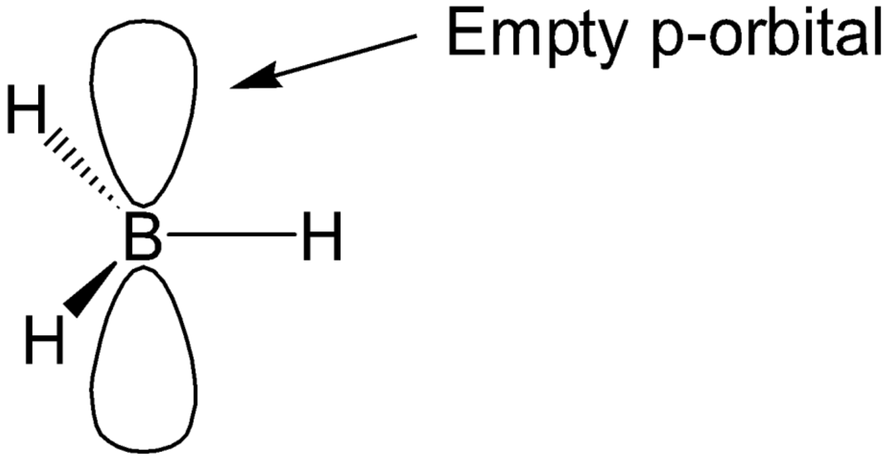

Figure 3-1. Empty P_z orbital

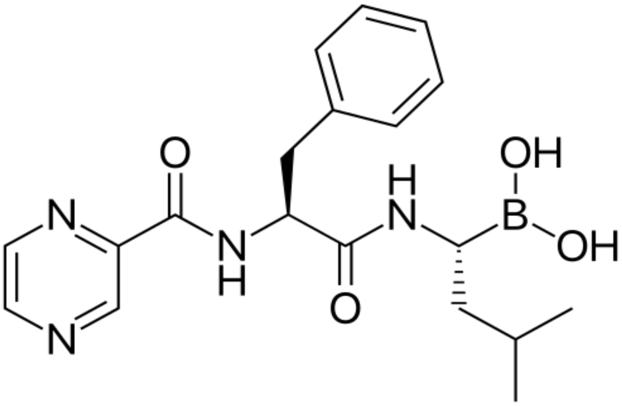

Figure 3-2. Bortezomib an anti-cancer drug

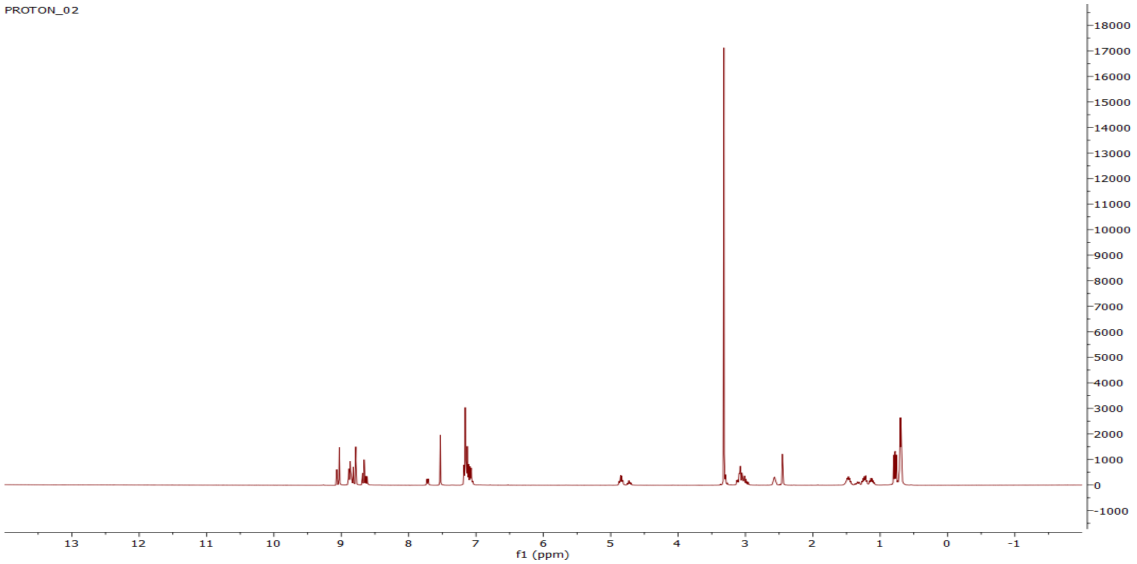

Figure 3-3. 1H NMR spectrum of Bortezomib

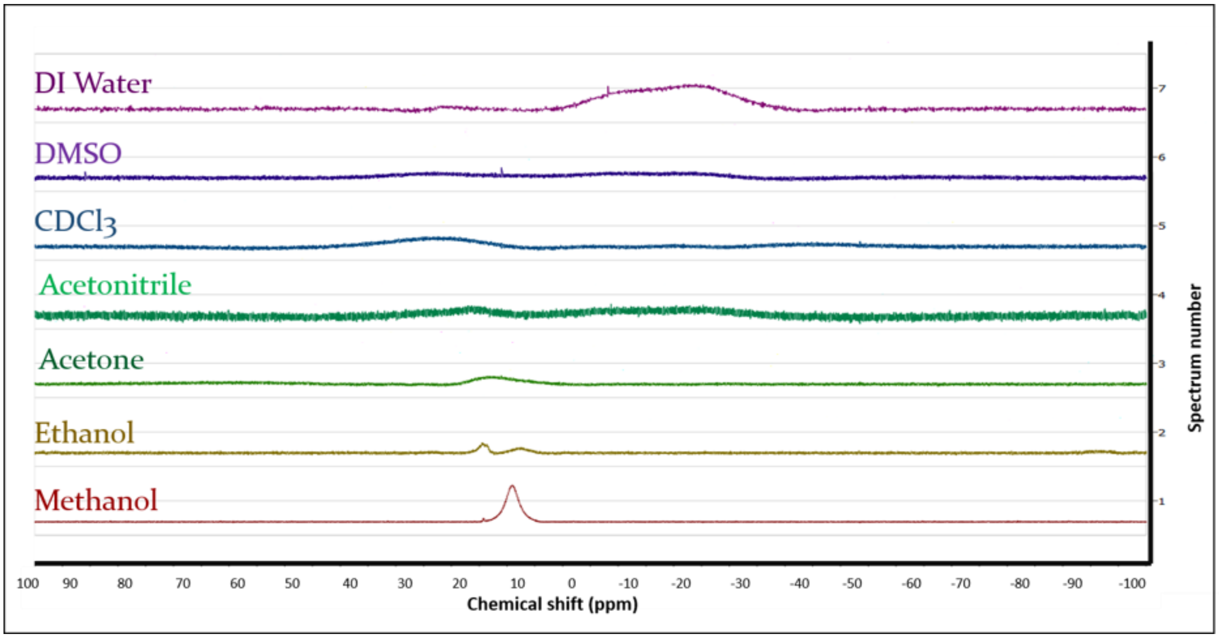

Figure 3-4. BTZ ^{11}B NMR spectra in selected screening solvents

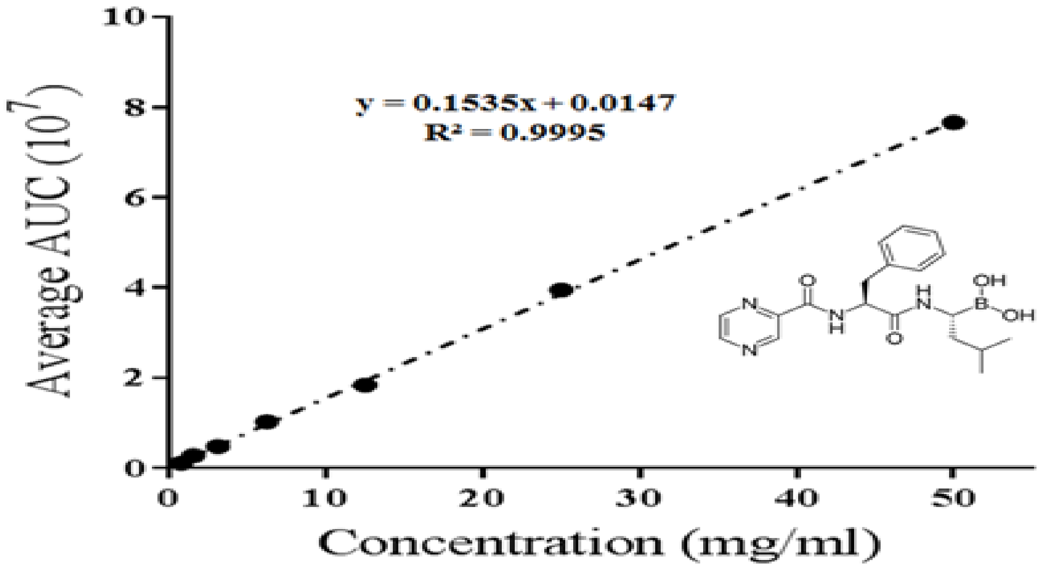

Figure 3-5. Linearity and calibration curve of ^{11}B qNMR method for BTZ. Each data point is an average of three replicated experiments (n=3)

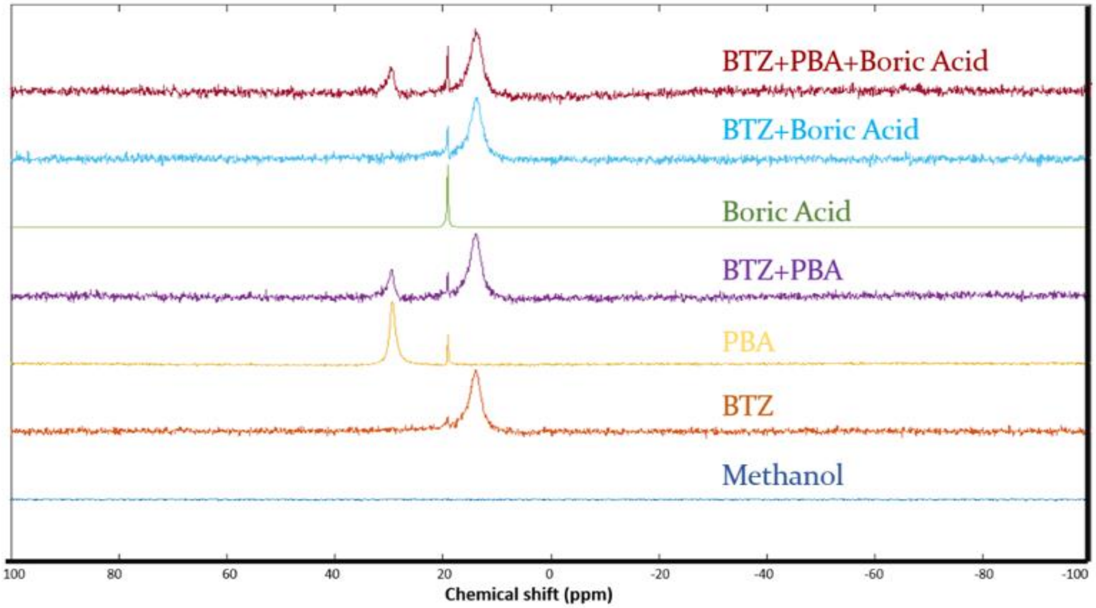

Figure 3-6. **S**pecificity of ^{11}B qNMR method for BTZ in the presence of Boric acid and PBA contaminants

Table 3-1. Accuracy of ^{11}B qNMR method represented as percent mean recovery

[a] Relative standard error

Concentration (mg/ml)	% Mean recovery ± %RSE[a] (n = 3)		
	Intra-day	Inter-day	
	Within-day (Day 1)	Day 2	Day 3
3	100.22 ± 1.52	106.45 ± 1.04	106.56 ± 0.59
6	95.68 ± 0.34	99.23 ± 0.43	103.00 ± 1.44
11	102.56 ± 0.34	101.49 ± 0.73	103.57 ± 0.20
16	97.13 ± 0.67	97.64 ± 0.15	99.72 ± 0.48

Table 3-2. Precision of ^{11}B qNMR method represented as percent relative
[a] Area Under Curve
[b] Relative Standard Error

Concentration (mg/ml)	Precision as %RSE[b] (n = 3)					
	Intra-day		Inter-day			
	Within-day (Day 1)		Day2		Day3	
	AUC[a] (10^7)	%RSE[b]	AUC[a] (10^7)	%RSE[b]	AUC[a] (10^7)	%RSE[b]
3	0.49		0.52		0.51	
	0.49	1.44	0.52	0.99	0.52	0.56
	0.47		0.50		0.51	
6	0.90		0.93		0.95	
	0.90	0.35	0.93	0.42	0.97	1.4
	0.91		0.94		1.00	
11	1.75		1.74		1.77	
	1.76	0.33	1.71	0.72	1.76	0.20
	1.74		1.76		1.78	
16	2.43		2.42		2.45	
	2.37	0.68	2.42	0.15	2.47	0.48
	2.41		2.41		2.49	

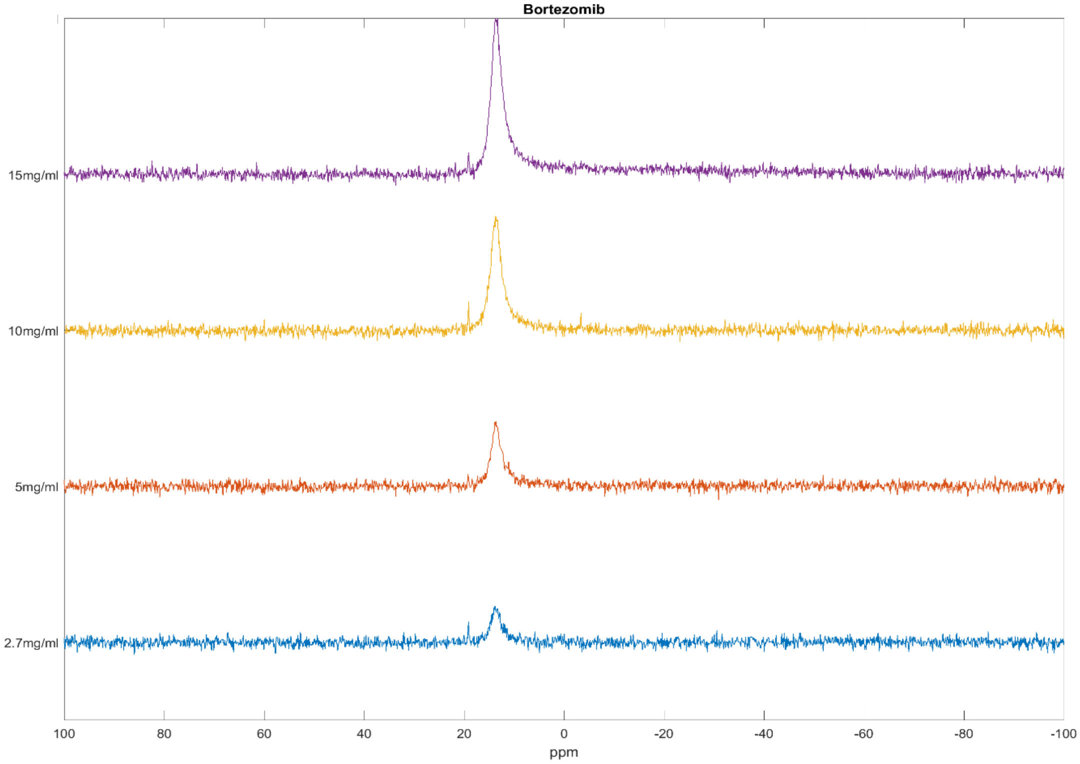

Figure 3-7. Accuracy and precision of ^{11}B qNMR method

NMR parameter		Robustness as %RSE[b] (n = 3)	
		Average area under curve AUC[a] (10^7)	%RSE[b]
Temperature (°C)	35	1.31	0.29
	37	1.29	0.44
	39	1.25	1.16
Pulse width (μs)	10.8	0.96	0.31
	11.0	1.01	0.27
	11.2	0.97	1.11
Relaxation delay (s)	0.2	0.86	0.61
	0.4	1.03	0.43
	0.6	1.06	0.14
Proton decoupling	Decoupled	1.04	0.64
	Coupled	0.98	0.49

Table 3-3. Robustness of ^{11}B qNMR

[a] Area Under Curve

[b] Relative Standard Error

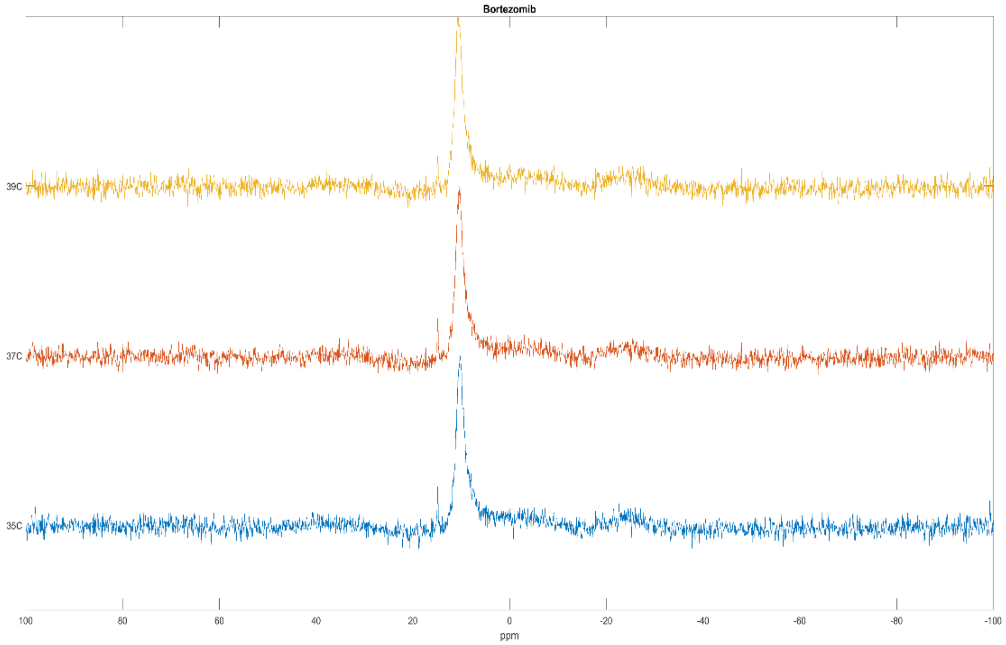

Figure 3-8. ^{11}B NMR spectra of BTZ at different temperatures

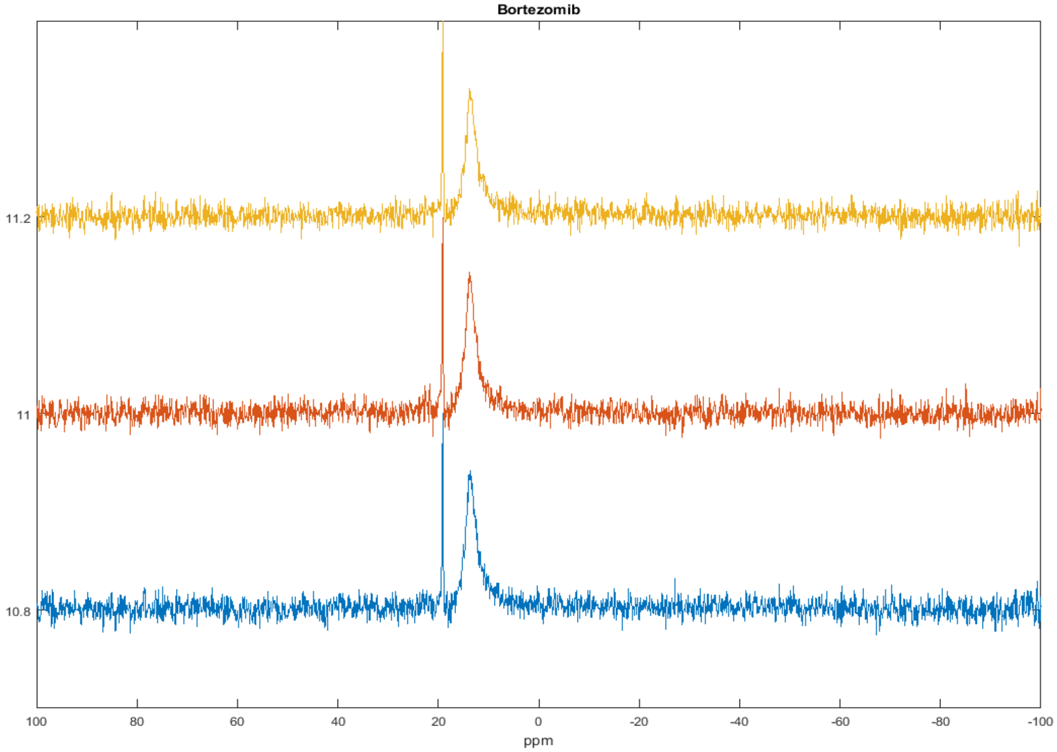

Figure 3-9. ^{11}B NMR spectra of BTZ with different pulse widths.

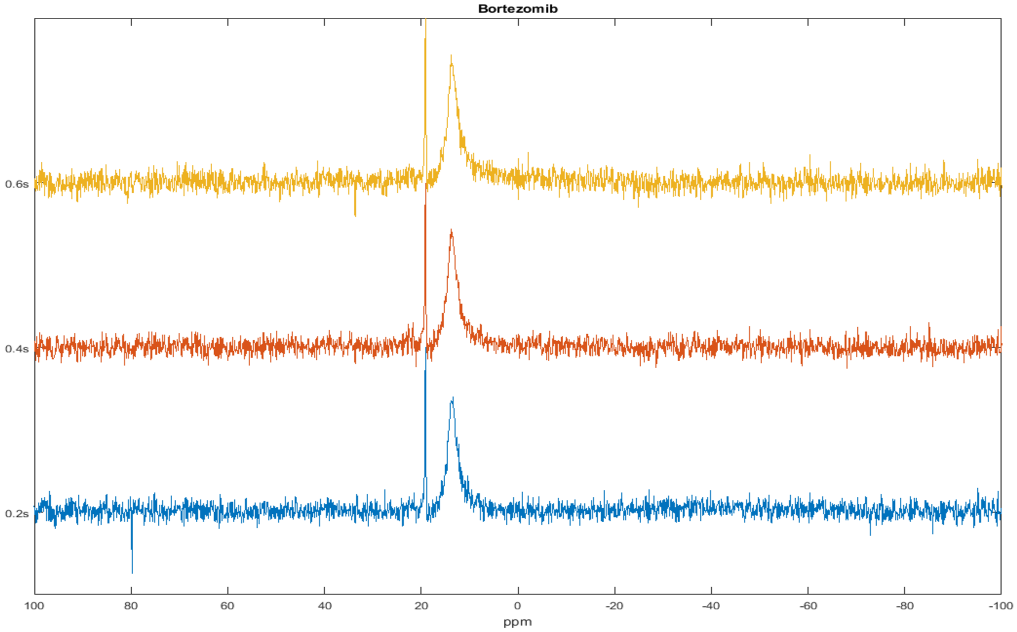

Figure 3-10. ^{11}B NMR spectra of BTZ at different relaxation delays

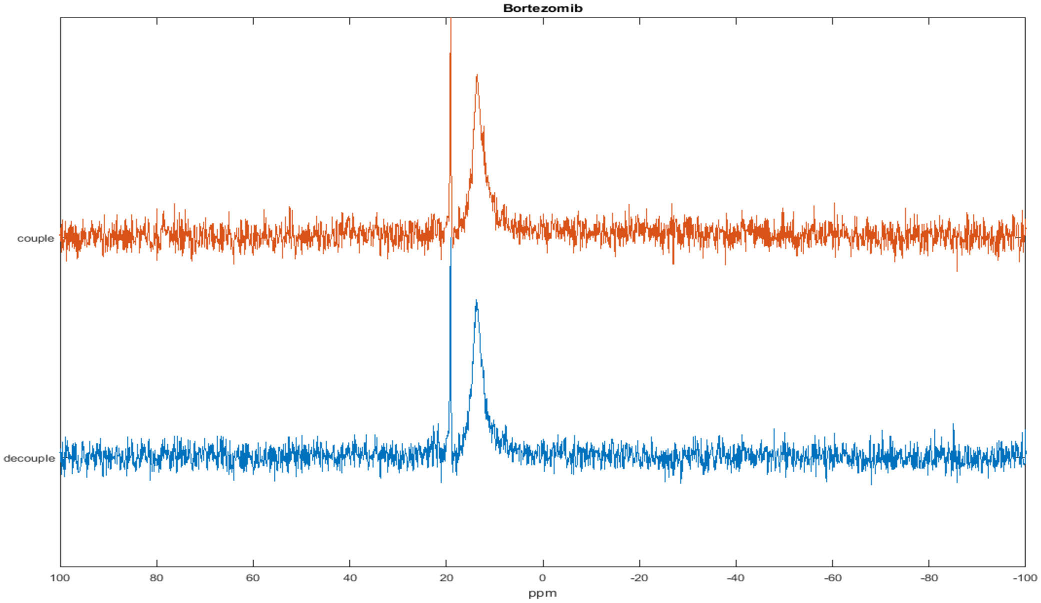

Figure 3-11. ^{11}B NMR spectra of BTZ proton coupled and decoupled

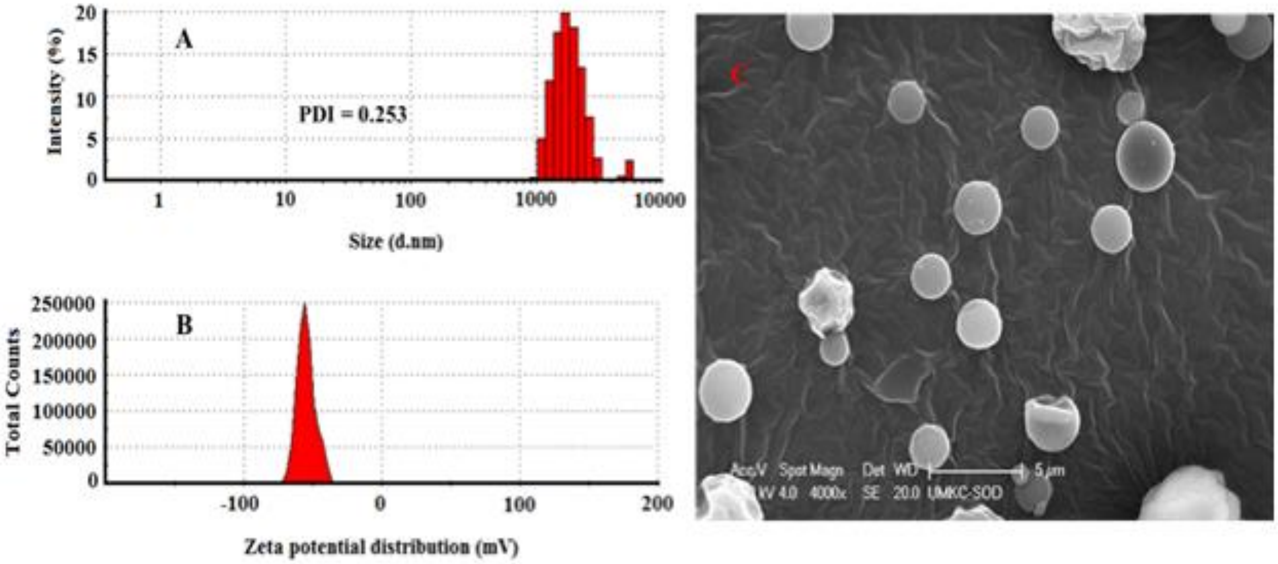

Figure 3-12. Average particle size (A), surface charge density (B) and SEM image (C) of BTZ/Alg microparticle formulation. SEM image scale bar is 5 µm

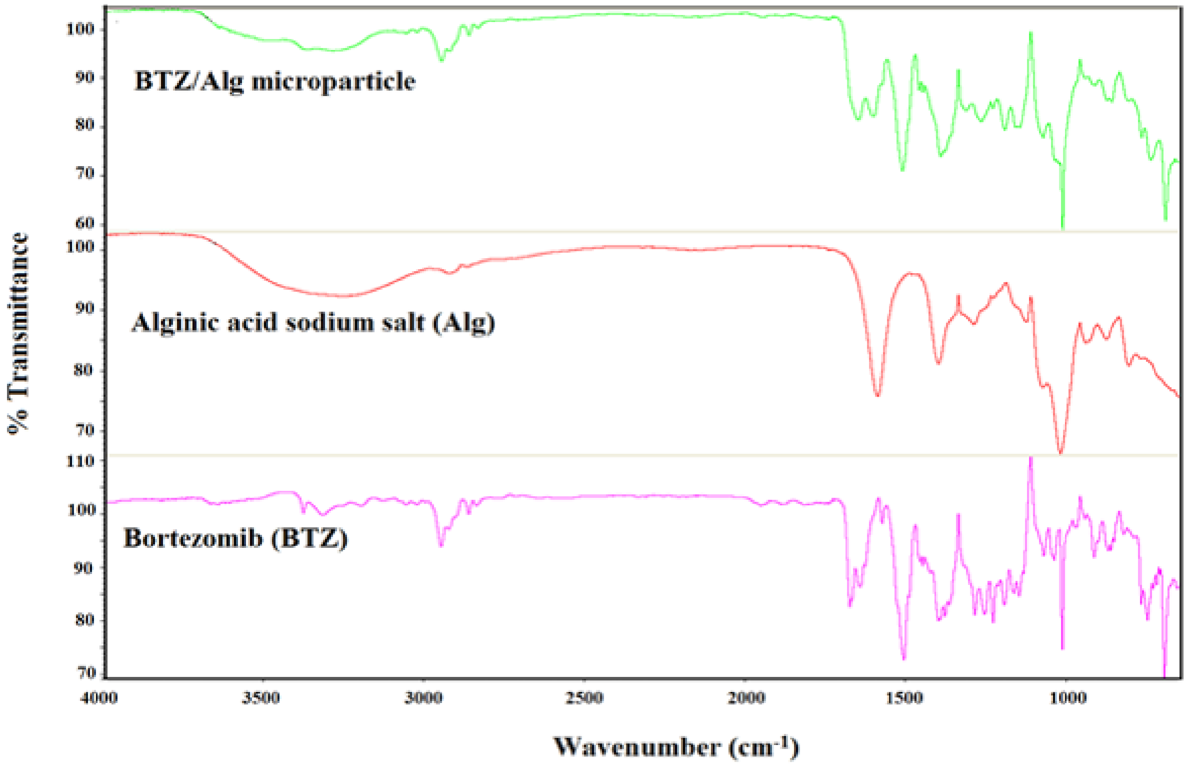

Figure 3-13. FTIR spectra of BTZ, alginic acid sodium salt (Alg) and BTZ/Alg microparticles

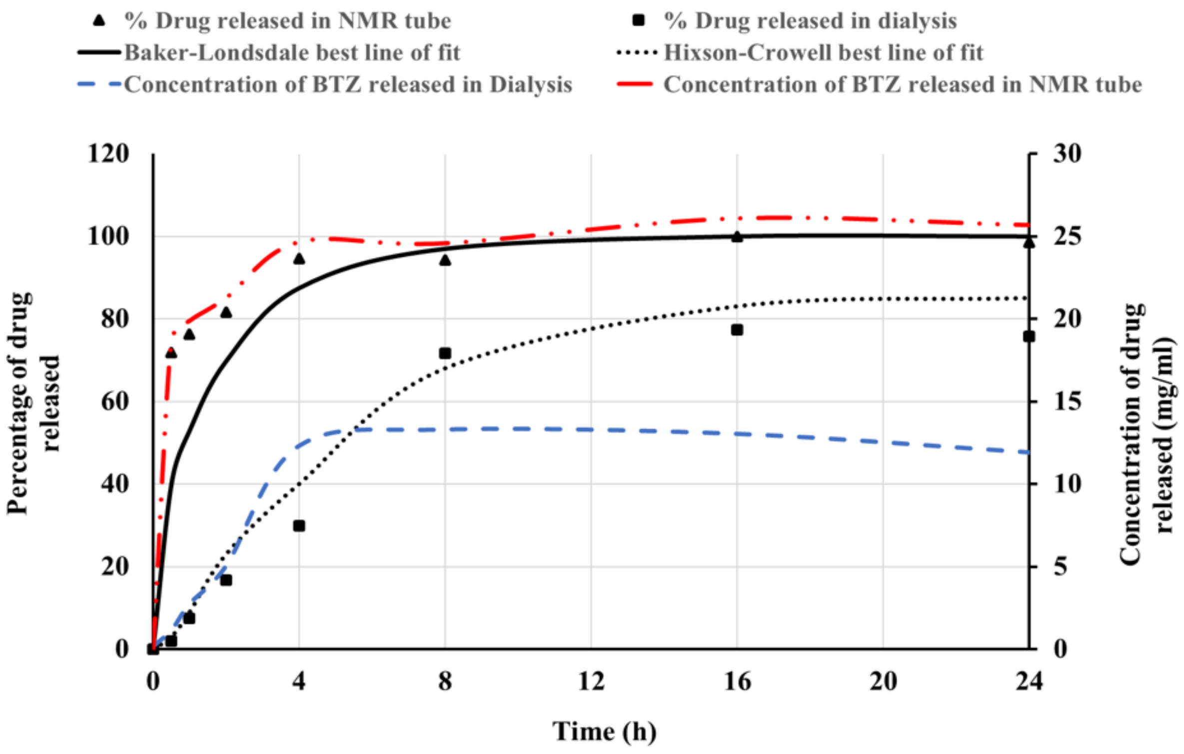

Figure 3-14. Percent cumulative drug release (%w/w) profiles of BTZ from BTZ/Alg microparticles by direct ^{11}B qNMR and dialysis methods. Actual drug concentration (mg/ml) released and best lines of fit are also represented. Each data point is an average of three replicated experiments (n=3)

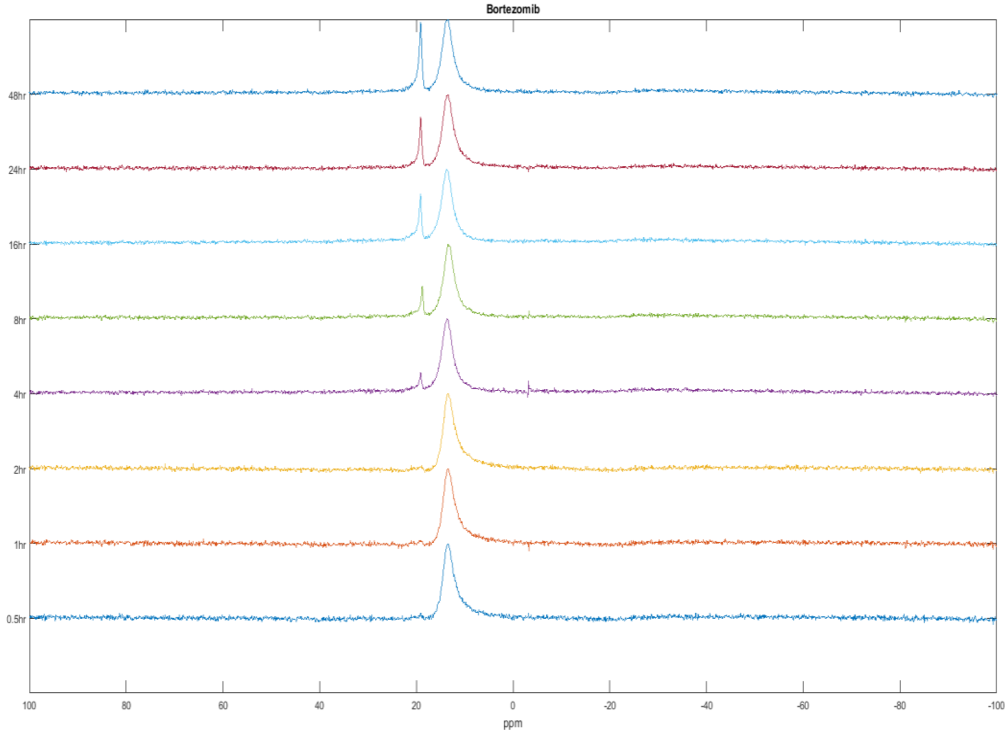

Figure 3-15. Drug release (%w/w) profiles of BTZ from BTZ/Alg microparticles by direct ^{11}B qNMR over time

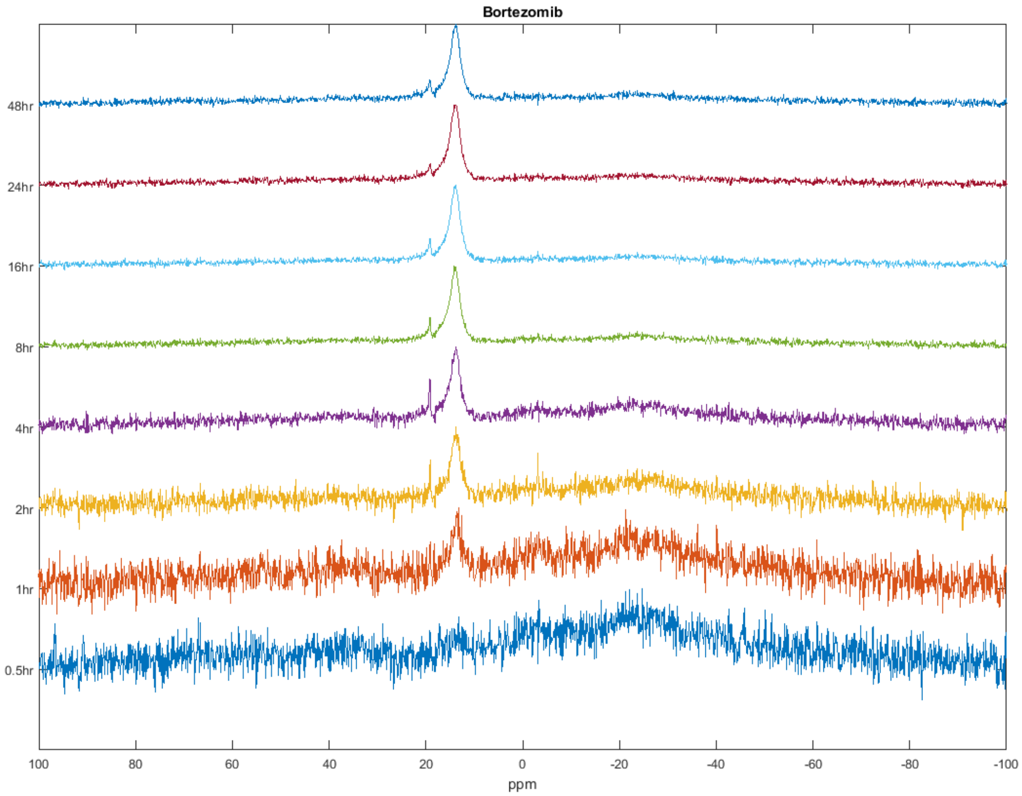

Figure 3-16. Drug release (%w/w) profiles of BTZ from BTZ/Alg microparticles by dialysis methods

Table 3-4. **:** Kinetic models describing BTZ *in vitro* release profiles from BTZ/Alg microparticles by the direct ^{11}B qNMR and dialysis methods

[a] Coefficient of determination, [b] Akaike information criterion

Kinetic Model	Direct ^{11}B qNMR method			Indirect dialysis method		
	Parameters	R^{2a}	AIC[b]	Parameters	R^{2a}	AIC[b]
Zero order	$k_0 = 3.069$	0.557	85.401	$k_0 = 2.860$	0.686	77.136
First order	$k_1 = 1.902$	0.834	52.412	$k_1 = 0.174$	0.977	54.548
Weibull	$\alpha = 0.661$	0.972	25.610	$\alpha = 19.082$	0.994	33.008
	$\beta = 0.337$			$\beta =1.773$		
Higuchi	$k_H = 28.481$	0.887	66.588	$k_H = 22.746$	0.938	53.5188
Korsmeyer-Peppas	$k_{KP} = 77.581$	0.969	26.120	$k_{KP} = 16.711$	0.955	44.332
	n = 0.098			n = 0.681		
Hixson–Crowell	$k_{HC} = 0.100$	0.980	55.600	$k_{HC} = 0.050$	0.986	37.616
Hopfenberg	$k_{HB} = 0.040$	0.821	41.382	$k_{HB} = 0.121$	0.999	19.031
	n = 4060.463			n = 0.773		
Baker–Lonsdale	$k_{BL} = 0.062$	0.980	39.661	$k_{BL} = 0.012$	0.964	38.945

References

(1) Jungnickel, J.L.;Forbes, J. W. Quantitative Measurement of Hydrogen Types by Intergrated Nuclear Magnetic Resonance Intensities. *Anal. Chem.* **1963**, 35.

(2) Hollis, D. P. Quantitative Analysis of Aspirin, Phenacetin, and Caffeine Mixtures by Nuclear Magnetic Resonance Spectrometry. *Anal. Chem.* **1963**, *35*.

(3) Staneva, J.; Denkova, P.; Todorova, M.; Evstatieva, L. Quantitative Analysis of Sesquiterpene Lactones in Extract of Arnica Montana L. by 1H NMR Spectroscopy. *J. Pharm. Biomed. Anal.* **2011**, *54* (1), 94–99. https://doi.org/10.1016/j.jpba.2010.08.018.

(4) Pieri, V.; Belancic, A.; Morales, S.; Stuppner, H. Identification and Quantification of Major Steviol Glycosides in Stevia Rebaudiana Purified Extracts by 1H NMR Spectroscopy. *J. Agric. Food Chem.* **2011**, *59* (9), 4378–4384. https://doi.org/10.1021/jf104922q.

(5) Yang, M.; Wang, J.; Kong, L. Quantitative Analysis of Four Major Diterpenoids in Andrographis Paniculata by 1H NMR and Its Application for Quality Control of Commercial Preparations. *J. Pharm. Biomed. Anal.* **2012**, *70*, 87–93. https://doi.org/10.1016/j.jpba.2012.05.037.

(6) Agrahari, V.; Meng, J.; Purohit, S. S.; Oyler, N. A.; Youan, B. B. C. Real-Time Analysis of Tenofovir Release Kinetics Using Quantitative Phosphorus (31P) Nuclear Magnetic Resonance Spectroscopy. *J. Pharm. Sci.* **2017**, *106* (10), 3005–3015. https://doi.org/10.1016/j.xphs.2017.03.043.

(7) Levy, G. C.; Pehk, T.; Srinivasan, P. R. Quantitative15N NMR Spectroscopy. *Org. Magn. Reson.* **1980**, *14* (2), 129–132. https://doi.org/10.1002/mrc.1270140210.

(8) Okaru, A. O.; Brunner, T. S.; Ackermann, S. M.; Kuballa, T.; Walch, S. G.; Kohl-himmelseher, M.; Lachenmeier, D. W. Application of 19 F NMR Spectroscopy for Content

Determination of Fluorinated Pharmaceuticals. **2017**. https://doi.org/10.1155/2017/9206297.

(9) Malz, F.; Jancke, H. Validation of Quantitative NMR. *J. Pharm. Biomed. Anal.* **2005**, *38*, 813–823. https://doi.org/10.1016/j.jpba.2005.01.043.

(10) http://www.softschools.com/formulas/chemistry/boron_trifluoride_formula/402/.

(11) Woods, W. G. An Introduction to Boron : History , Sources , Uses , and Chemistry. *Env. Heal. Perspect* **1994**, *101* (7), 5–11. https://doi.org/10.1289/ehp.94102s75.

(12) Hunter, P. Not Boring at All. Boron Is the New Carbon in the Quest for Novel Drug Candidates. *EMBO Rep.* **2009**, *10* (2), 125–128. https://doi.org/10.1038/embor.2009.2.

(13) Das, B. C.; Thapa, P.; Karki, R.; Schinke, C.; Das, S.; Kambhampati, S.; Banerjee, S. K.; Van Veldhuizen, P.; Verma, A.; Weiss, L. M.; et al. Boron Chemicals in Diagnosis and Therapeutics. *Future Med. Chem.* **2013**, *5* (6), 653–676. https://doi.org/10.4155/fmc.13.38.

(14) Zhong, Q.; Zhang, C.; Zhang, Q.; Miele, L.; Zheng, S.; Wang, G. Boronic Prodrug of 4-Hydroxytamoxifen Is More Efficacious than Tamoxifen with Enhanced Bioavailability Independent of CYP2D*6 Status. *BMC Cancer* **2015**, *15* (1), 1–9. https://doi.org/10.1186/s12885-015-1621-2.

(15) Baker, S. J.; Ding, C. Z.; Akama, T.; Zhang, Y. K.; Hernandez, V.; Xia, Y. Therapeutic Potential of Boron-Containing Compounds. Future Med Chem. **2009**, *1*, 7. https://doi.org/10.4155/fmc.09.71.

(16) Barranco, W. T.; Eckhert, C. D. Cellular Changes in Boric Acid-Treated DU-145 Prostate Cancer Cells. *Br. J. Cancer* **2006**, *94* (6), 884–890. https://doi.org/10.1038/sj.bjc.6603009.

(17) Barranco, W. T.; Eckhert, C. D. Boric Acid Inhibits Human Prostate Cancer Cell Proliferation. *Cancer Lett.* **2004**, *216* (1), 21–29.

https://doi.org/10.1016/j.canlet.2004.06.001.

(18) Rainey, C. J.; Nyquist, L. A.; Christensen, R. E.; Strong, P. L.; Culver, B. D.; Coughlin, J. R. Daily Boron Intake from the American Diet. *J. Am. Diet. Assoc.* **1999**, *99* (3), 335–340. https://doi.org/10.1016/S0002-8223(99)00085-1.

(19) Eager, R. M.; Cunningham, C. C.; Senzer, N.; Richards, D. A.; Raju, R. N.; Jones, B.; Uprichard, M.; Nemunaitis, J. Phase II Trial of Talabostat and Docetaxel in Advanced Non-Small Cell Lung Cancer. *Clin. Oncol.* **2009**, *21* (6), 464–472. https://doi.org/10.1016/j.clon.2009.04.007.

(20) Hou, J.; Jin, J.; Xu, Y.; Wu, D.; Ke, X.; Zhou, D.; Lu, J.; Du, X.; Chen, X.; Li, J.; et al. Randomized, Double-Blind, Placebo-Controlled Phase III Study of Ixazomib plus Lenalidomide-Dexamethasone in Patients with Relapsed/Refractory Multiple Myeloma: China Continuation Study. *J. Hematol. Oncol.* **2017**, *10* (1), 137. https://doi.org/10.1186/s13045-017-0501-4.

(21) Nedunchezhian, K. Boron Neutron Capture Therapy - A Literature Review. *J. Clin. DIAGNOSTIC Res.* **2016**, *10* (12), ZE01-ZE04. https://doi.org/10.7860/JCDR/2016/19890.9024.

(22) Coderre, J.A., Elowitz, E.H., Chadha, M., Bergland, R., Capala, J., Joel, D.D., Liu, H.B., Slatkin, D.N., Chanana, A. . D. Boron Neutron Capture Therapy for Glioblastoma Multiforme Using P-Boronophenylalanine and Epithermal Neutrons: Trial Design and Early Clinical Results. *J. Neurooncol.* **1997**, *33* (1–2), 141–152.

(23) Barth, R. F. Boron Neutron Capture Therapy at the Crossroads: Challenges and Opportunities. *Appl. Radiat. Isot.* **2009**, *67* (7–8), S3–S6. https://doi.org/10.1016/j.apradiso.2009.03.102.

(24) Yong, Z.; Song, Z.; Zhou, Y.; Liu, T.; Zhang, Z.; Zhao, Y.; Chen, Y.; Jin, C.; Chen, X.; Lu, J.; et al. Boron Neutron Capture Therapy for Malignant Melanoma: First Clinical Case Report in China. *Chinese J. Cancer Res.* **2016**, *28* (6), 634–640. https://doi.org/10.21147/j.issn.1000-9604.2016.06.10.

(25) Ma, L.; Hamdi, J.; Wong, F.; Hawthorne, M. F. Closomers of High Boron Content: Synthesis, Characterization, and Potential Application as Unimolecular Nanoparticle Delivery Vehicles for Boron Neutron Capture Therapy. *Inorg. Chem.* **2006**, *45* (1), 278–285. https://doi.org/10.1021/ic051214q.

(26) Kaphingst, K. A.; Persky, S.; Lachance, C. NIH Public Access. **2010**, *14* (4), 384–399. https://doi.org/10.1080/10810730902873927.

(27) Zambito, Y.; Pedreschi, E.; Di Colo, G. Is Dialysis a Reliable Method for Studying Drug Release from Nanoparticulate Systems? - A Case Study. *Int. J. Pharm.* **2012**, *434* (1–2), 28–34. https://doi.org/10.1016/j.ijpharm.2012.05.020.

(28) Zhou, Y.; He, C.; Chen, K.; Ni, J.; Cai, Y.; Guo, X.; Wu, X. Y. A New Method for Evaluating Actual Drug Release Kinetics of Nanoparticles inside Dialysis Devices via Numerical Deconvolution. *J. Control. Release* **2016**, *243*, 11–20. https://doi.org/10.1016/j.jconrel.2016.09.031.

(29) Modi, S.; Anderson, B. D. Determination of Drug Release Kinetics from Nanoparticles: Overcoming Pitfalls of the Dynamic Dialysis Method. *Mol. Pharm.* **2013**, *10* (8), 3076–3089. https://doi.org/10.1021/mp400154a.

(30) Xie, L.; Beyer, S.; Vogel, V.; Wacker, M. G.; Mäntele, W. Assessing the Drug Release from Nanoparticles: Overcoming the Shortcomings of Dialysis by Using Novel Optical Techniques and a Mathematical Model. *Int. J. Pharm.* **2015**, *488* (1–2), 108–119.

https://doi.org/10.1016/j.ijpharm.2015.03.080.

(31) Https://en.wikipedia.org/wiki/Bortezomib#/media/File:Bortezomib.svg.

(32) Field-Smith, A.; Morgan, G. J.; Davies, F. E. Bortezomib (Velcadetrade Mark) in the Treatment of Multiple Myeloma. *Ther Clin Risk Manag* **2006**, *2* (3), 271–279.

(33) Kostidis, S.; Addie, R. D.; Morreau, H.; Mayboroda, O. A.; Giera, M. Quantitative NMR Analysis of Intra- and Extracellular Metabolism of Mammalian Cells: A Tutorial. *Anal. Chim. Acta* **2017**, *980*, 1–24. https://doi.org/10.1016/j.aca.2017.05.011.

(34) Weber, M.; Hellriegel, C.; Rueck, A.; Wuethrich, J.; Jenks, P.; Obkircher, M. Method Development in Quantitative NMR towards Metrologically Traceable Organic Certified Reference Materials Used as ^{31}P QNMR Standards. *Anal. Bioanal. Chem.* **2015**, *407* (11), 3115–3123. https://doi.org/10.1007/s00216-014-8306-6.

(35) Zhang, C.; Zhang, T.; Oyler, N. A.; Youan, B. B. C. Direct and Real-Time Quantification of Tenofovir Release from Ph-Sensitive Microparticles into Simulated Biological Fluids Using1H Nuclear Magnetic Resonance. *J. Pharm. Sci.* **2014**, *103* (4), 1170–1177. https://doi.org/10.1002/jps.23886.

(36) Pauli, G. F.; Jaki, B. U.; Lankin, D. C. Quantitative 1H NMR: Development and Potential of a Method for Natural Products Analysis. *J. Nat. Prod.* **2005**, *68* (1), 133–149. https://doi.org/10.1021/np0497301.

(37) Jones, C.; Ravenscroft, N. NMR Assays for Carbohydrate-Based Vaccines. *NMR Spectrosc. Pharm. Anal.* **2008**, *38*, 341–368. https://doi.org/10.1016/B978-0-444-53173-5.00014-7.

(38) Holzgrabe, U. Quantitative NMR Spectroscopy in Pharmaceutical R&D. *eMagRes* **2015**, *4* (1), 45–56. https://doi.org/10.1002/9780470034590.emrstm1399.

(39) Wells, R. J.; Hook, J. M.; Al-Deen, T. S.; Hibbert, D. B. Quantitative Nuclear Magnetic

Resonance (QNMR) Spectroscopy for Assessing the Purity of Technical Grade Agrochemicals: 2,4-Dichlorophenoxyacetic Acid (2,4-D) and Sodium 2,2-Dichloropropionate (Dalapon Sodium). *J. Agric. Food Chem.* **2002**, *50* (12), 3366–3374. https://doi.org/10.1021/jf0114379.

(40) Yang, Q.; Qiu, H.; Guo, W.; Wang, D.; Zhou, X.; Xue, D.; Zhang, J.; Wu, S.; Wang, Y. Quantitative ^{1}H-NMR Method for the Determination of Tadalafil in Bulk Drugs and Its Tablets. *Molecules* **2015**, *20* (7), 12114–12124. https://doi.org/10.3390/molecules200712114.

(41) Okamura,E.; Kimura,T.; Nakahara,M.; Tanaka, M.; Handa,T.; Saito,H. 13C NMR Method for the Determination of Peptide and Protein Binding Sites in Lipid Bilayers and Emulsions. *J. Phys. Chem. B* **2001**, *105* (50), 12616–12621. https://doi.org/10.1021/jp012583k.

(42) Zhang, F.-F.; Jiang, M.-H.; Sun, L.-L.; Zheng, F.; Dong, L.; Shah, V.; Shen, W.-B.; Ding, Y. Quantitative Analysis of Sitagliptin Using the ^{19} F-NMR Method: A Universal Technique for Fluorinated Compound Detection. *Analyst* **2015**, *140* (1), 280–286. https://doi.org/10.1039/C4AN01681E.

(43) Bendel, P. Biomedical Applications of 10B and 11B NMR. *NMR Biomed.* **2005**, *18* (2), 74–82. https://doi.org/10.1002/nbm.886.

(44) Wrackmeyer B. Organoboron Chemistry. In Modern Magnetic Resonance; Springer, Dordrecht, 2008; pp 455–457. https://doi.org/https://doi.org/10.1007/1-4020-3910-7_56.

(45) thenmrlab http://chem.ch.huji.ac.il/nmr/techniques/1d/row2/b.html. (2/2/2018).

(46) pyPulsar http://www-lcs.ensicaen.fr/pyPulsar/index.php/List_of_NMR_isotopes. (2/2/2018),.

(47) Malet-Martino, M. C.; Martino, R. Uses and Limitations of Nuclear Magnetic Resonance

(NMR) Spectroscopy in Clinical Pharmacokinetics. *Clin Pharmacokinet* **1991**, *20* (5), 337–49.

(48) Okaru, A. O.; Brunner, T. S.; Ackermann, S. M.; Kuballa, T.; Walch, S. G.; Kohl-Himmelseher, M.; Lachenmeier, D. W. Application of 19F NMR Spectroscopy for Content Determination of Fluorinated Pharmaceuticals. *J. Anal. Methods Chem.* **2017**, *2017*, 7. https://doi.org/10.1155/2017/9206297.

(49) Malet-Martino, M. C.; Martino, R. Magnetic Resonance Spectroscopy: A Powerful Tool for Drug Metabolism Studies. *Biochimie* **1992**, *74* ((9-10)), 785–800. https://doi.org/10.1097/YCO.0000000000000159.

(50) Ich. ICH Topic Q2 (R1) Validation of Analytical Procedures : Text and Methodology. *Int. Conf. Harmon.* **2005**, *1994* (November 1996), 17. https://doi.org/http://www.ich.org/fileadmin/Public_Web_Site/ICH_Products/Guidelines/Quality/Q2_R1/Step4/Q2_R1__Guideline.pdf.

(51) Meng, J.; Agrahari, V.; Ezoulin, M. J.; Purohit, S. S.; Zhang, T.; Molteni, A.; Dim, D.; Oyler, N. A.; Youan, B.-B. C. Spray-Dried Thiolated Chitosan-Coated Sodium Alginate Multilayer Microparticles for Vaginal HIV Microbicide Delivery. *AAPS J.* **2017**, *19* (3), 692–702. https://doi.org/10.1208/s12248-016-0007-y.

(52) Coulibaly, F. S.; Ezoulin, M. J. M.; Purohit, S. S.; Ayon, N. J.; Oyler, N. A.; Youan, B. B. C. Layer-by-Layer Engineered Microbicide Drug Delivery System Targeting HIV-1 Gp120: Physicochemical and Biological Properties. *Mol. Pharm.* **2017**, *14* (10), 3512–3527. https://doi.org/10.1021/acs.molpharmaceut.7b00555.

(53) Coulibaly, F. S.; Youan, B. B. C. Concanavalin A-Polysaccharides Binding Affinity Analysis Using a Quartz Crystal Microbalance. *Biosens. Bioelectron.* **2014**, *59*, 404–411.

https://doi.org/10.1016/j.bios.2014.03.040.

(54) Costa, P., & Lobo, J. M. S. Modelling and Comparison of Dissolution Profiles. *Eur. J. Pharm. Sci.* **2001**, *13*, 123–133. https://doi.org/10.1016/S0928-0987(01)00095-1.

(55) Ripplinger, J.; Sullivan, J. Does Choice in Model Selection Affect Maximum Likelihood Analysis? *Syst. Biol.* **2008**, *57* (1), 76–85. https://doi.org/10.1080/10635150801898920.

(56) Vrieze, S. I. Model Selection and Psychological Theory: A Discussion of the Differences between the Akaike Information Criteria (AIC) and the Bayesian Information Criteria (BIC). *Psychol. Methods* **2012**, *17* (2), 228–243. https://doi.org/10.1037/a0027127.Model.

(57) Tabrizi, M. E. A. B and H-NMR Evaluation of Chemical Interactions between Two Polyphenols; Epigallocatechingallate and Quercetin with Bortezomib. *Biosci. Biotechnol. Res. Asia* **2014**, *11* (2), 577–586. https://doi.org/10.13005/bbra/1309.

(58) Korb, J. P.; Vorapalawut, N.; Nicot, B.; Bryant, R. G. Relation and Correlation between NMR Relaxation Times, Diffusion Coefficients, and Viscosity of Heavy Crude Oils. *J. Phys. Chem. C* **2015**, *119* (43), 24439–24446. https://doi.org/10.1021/acs.jpcc.5b07510.

(59) Wand, A. J.; Ehrhardt, M. R.; Flynn, P. F. High-Resolution NMR of Encapsulated Proteins Dissolved in Low-Viscosity Fluids. *Proc. Natl. Acad. Sci. U. S. A.* **1998**, *95* (December), 15299–15302. https://doi.org/10.1073/pnas.95.26.15299.

(60) Brus, J.; Czernek, J.; Urbanova, M.; Kobera, L.; Jegorov, A. An Efficient 2D11B-11B Solid-State NMR Spectroscopy Strategy for Monitoring Covalent Self-Assembly of Boronic Acid-Derived Compounds: The Transformation and Unique Architecture of Bortezomib Molecules in the Solid State. *Phys. Chem. Chem. Phys.* **2017**, *19* (1), 487–495. https://doi.org/10.1039/c6cp06555d.

(61) Nishiura, K.; Urawa, Y.; Soda, S. N -Arylation of Benzimidazole with Arylboronate,

Boroxine and Boronic Acids. Acceleration with an Optimal Amount of Water. *Adv. Synth. Catal.* **2004**, *346* (13–15), 1679–1684. https://doi.org/10.1002/adsc.200404193.

(62) Marinaro, W. A.; Schieber, L. J.; Munson, E. J.; Day, V. W.; Stella, V. J. Properties of a Model Aryl Boronic Acid and Its Boroxine. *J. Pharm. Sci.* **2012**, *101* (9), 3190–3198. https://doi.org/10.1002/jps.23207.

(63) Ivanov, A. S.; Shishkov, S. V.; Zhalnina, A. A. Synthesis and Characterization of Organic Impurities in Bortezomib Anhydride Produced by a Convergent Technology. *Sci. Pharm.* **2012**, *80* (1), 67–75. https://doi.org/10.3797/scipharm.1109-02.

(64) ock, C. W., Bhat, K. L., Larkin, J. D., & Markham, G. D. Thermodynamics of Boroxine Formation from the Aliphatic Boronic Acid Monomers R–B(OH)2 (R = H, H3C, H2N, HO, and F): A Computational Investigation. *J Phys Chem A* **2011**, *115* ((26)), 7785–93.

(65) Katsutoshi Nishiura, Y. U., S. S. N-Arylation of Benzimidazole with Arylboronate, Boroxine and Boronic Acids. Acceleration with an Optimal Amount of Water. *Adv. Synth. Catal.* **2004**, *346* (1679–1684), 13–15.

(66) Smith, W. L. Boron-11 Nmr. *J. Chem. Educ.* **1977**, *54* (8), 469. https://doi.org/10.1021/ed054p469.

(67) CHANDRA K SEKHAR, P. S., G.RAMESH REDDY, P.VIJAYA BABU, N. L. S. A NEW UV-METHOD FOR DETERMINATION OF BORTEZOMIB IN BULK AND PHARMACEUTICAL DOSAGE FORM. *Int J Pharm Bio Sci* **2013**, *3* (1), 623–627.

(68) Kamalzadeh, Z.; Babanezhad, E.; Ghaffari, S.; Mohseni Ezhiyeh, A.; Mohammadnejad, M.; Naghibfar, M.; Bararjanian, M.; Attar, H. Determination of Bortezomib in API Samples Using HPLC: Assessment of Enantiomeric and Diastereomeric Impurities. *J Chromatogr Sci* **2017**, *55* (7), 697–705.

(69) Hasada, K.; Yoshida, T.; Yamazaki, T.; Sugimoto, N.; Nishimura, T.; Nagatsu, A.; Mizukami, H. Quantitative Determination of Atractylon in Atractylodis Rhizoma and Atractylodis Lanceae Rhizoma By1H-NMR Spectroscopy. *J. Nat. Med.* **2010**, *64* (2), 161–166. https://doi.org/10.1007/s11418-010-0393-x.

(70) Safe, S. H.; Gasiewicz, T.; Whitlock, J. P. Mechanism of Action. **2011**, 61–91. https://doi.org/10.1007/978-3-642-70556-4_3.

(71) Islam, P.; Water, J. J.; Bohr, A.; Rantanen, J. Chitosan-Based Nano-Embedded Microparticles: Impact of Nanogel Composition on Physicochemical Properties. *Pharmaceutics* **2017**, *9* (1), 1–12. https://doi.org/10.3390/pharmaceutics9010001.

(72) Sosnik, A.; Seremeta, K. P. Advantages and Challenges of the Spray-Drying Technology for the Production of Pure Drug Particles and Drug-Loaded Polymeric Carriers. *Adv. Colloid Interface Sci.* **2015**, *223*, 40–54. https://doi.org/10.1016/j.cis.2015.05.003.

(73) Ngamcherdtrakul, W.; Morry, J.; Gu, S.; Castro, D. J.; Goodyear, S. M.; Sangvanich, T.; Reda, M. M.; Lee, R.; Mihelic, S. A.; Beckman, B. L.; Hu, Z.; Gray, J. W.; Yantasee, WNgamcherdtrakul, W.; Morry, J.; Gu, S.; Castro, D. J.; Goodyear, S. M.; Sangvanic, W. Cationic Polymer Modified Mesoporous Silica Nanoparticles for Targeted SiRNA Delivery to HER2+ Breast Cancer. *Adv Funct Mater* **2015**, *25* (18), 2646–2659.

(74) Stetefeld, J.; McKenna, S. A.; Patel, T. R. Dynamic Light Scattering: A Practical Guide and Applications in Biomedical Sciences. *Biophys. Rev.* **2016**, *8* (4), 409–427. https://doi.org/10.1007/s12551-016-0218-6.

(75) Shinde UA, N. M. Characterization of Gelatin-Sodium Alginate Complex Coacervation System. *Indian J Pharm Sci.* **2009**, *71* (3), 313–317. https://doi.org/10.4103/0250-474X.56033.

(76) Romanos, J.; Beckner, M.; Stalla, D.; Tekeei, A.; Suppes, G.; Jalisatgi, S.; Lee, M.; Hawthorne, F.; Robertson, J. D.; Firlej, L.; et al. Infrared Study of Boron-Carbon Chemical Bonds in Boron-Doped Activated Carbon. *Carbon N. Y.* **2013**, *54*, 208–214. https://doi.org/10.1016/j.carbon.2012.11.031.

(77) Leal, D.; Matsuhiro, B.; Rossi, M.; Caruso, F. FT-IR Spectra of Alginic Acid Block Fractions in Three Species of Brown Seaweeds. *Carbohydr. Res.* **2008**, *343* (2), 308–316. https://doi.org/10.1016/j.carres.2007.10.016.

(78) Fu, Y.; Kao, W. J. Drug Release Kinetics and Transport Mechanisms of Non-Degradable and Degradable Polymeric Delivery Systems. *Expert Opin. Drug Deliv.* **2010**, *7* (4), 429–444. https://doi.org/10.1517/17425241003602259.

Chapter 4 . QUANTITATIVE ANALYSIS OF MARAVIROC RELEASE FROM MICROPARTICLES INTO SIMULATED BIOLOGICAL FLUIDS USING FLUORINE (^{19}F) NUCLEAR MAGNETIC RESONANCE SPECTROSCOPY

4.1 Introduction

It has been estimated that the number of persons living with HIV worldwide in 2017 was 36.7 million, out of which new infections are 44% higher in women. Women who acquired HIV-1 through vaginal intercourse represent ∼60% of new infections in endemic regions, and there is no known cure for the condition [1]. Many anti-retroviral (ARV) drugs have been clinically and FDA approved for the treatment of HIV, and a recent addition to this set of ARVs is a new class of drug. These new classes are known as entry inhibitors[2]. They prevent the entry of HIV R5 tropic strains into the host body by inhibiting the attachment of the HIV gp120 onto the human CCR5 co-receptors. In other words, they are known as "anti CCR5 antagonists', and the only FDA approved drug in this class is called Maraviroc (MVC).

MVC is a small molecule (Figure 4-1)[3] , and it is a white to yellowish or brownish powder with a chemical name of 4,4-difluoro-N-[(1S)-3-[(1R,5S)-3-(3-methyl-5-propan-2-yl-1,2,4-triazol-4-yl)-8-azabicyclo[3.2.1]octan-8-yl]-1-phenylpropyl]cyclohexane-1-carboxamide,and chemical formula $C_{29}H_{41}F_2N_5O$. It is a chemokine receptor antagonist that works by blocking the interaction between the HIV viral envelope complex (gp120 and gp41) and CCR5 by allosteric inhibition[2]. MVC is sparingly soluble in water (~ 0.0106 mg/mL), slightly soluble in some organic solvents, and highly soluble across physiological pH (1-7)[2].

MVC has been developed by Pfizer for oral administration only, and the absolute oral bioavailability of a 100 mg dose is 23%[4]. About 65% of MVC is metabolized in the liver, and hepatotoxicity with allergic features including life-threatening events has been reported with the use of MVC in clinical trials, and post marketing [2]. Nonetheless, the FDA has approved the use of MVC with a label warning for possible hepatotoxic side effects.

Vaginal microbicides are a potentially useful way to prevent the sexual transmission of HIV in order to bypass the metabolism of MVC in the liver and subsequently the hepatotoxic side effect MVC might have. MVC formulation intended for vaginal drug delivery of MVC has been investigated and results have been published in peer review journals. Malcolm et al. investigated the pharmacokinetics and efficacy of a vaginally administered MVC gel in rhesus macaques[4], while in another study, Ball and Woodrow developed an electrospun solid dispersions of MVC for rapid intravaginal preexposure prophylaxis of HIV. They were able to successfully formulate MVC up to 28 wt% into electrospun solid dispersions made from either polyvinylpyrrolidone or poly(ethylene oxide) nanofibers or microfibers[4]. Furthermore, in 2018, Vincen et al. conducted a phase 1 trial to evaluate the safety and pharmacokinetics of pod-intravaginal rings (IVR) using a triple combination antiretroviral where MVC was a part of this combination[5]. They found that the pod-IVRs were safe and generally well tolerated in all treatment periods, and there were no concerning safety findings by participant report, examination with colposcopy, evaluation of vaginal microbiome (VMB), or histology from vaginal biopsy[5].

In this study, we developed and validated a ^{19}F qNMR method that was effective in studying the real-time release of MVC from a spray-dried alginate microparticle formulation in a vaginal and seminal stimulated environment. Additionally, MVC real-time release kinetics were compared to the traditionally used dialysis method for drug release studies from nano or micro formulations. With the promising future that MVC could be ultimately formulated and licensed as a vaginal microbicide, this study may provide an additional tool for the analysis of and quantification of MVC and other fluorine containing pharmaceuticals in biologically stimulated environments e.g. vaginal and seminal fluids, blood plasma, etc. This study may also contribute to the growing discussion on the use and effectiveness of the dialysis methods for studying drug release kinetics.

4.2 Quantitative NMR spectroscopy

Quantitative NMR spectroscopy techniques have demonstrated their extraordinary use as an analytical tool in pharmaceutical science. In contrast to other analytical techniques, NMR offers several advantages such as: (i) non-destructive and highly predictable character (ii) short measuring time (iii) easy sample preparation and handling (iv) no need for prior isolation or purification characterization of analyte mixtures.

^{1}H and ^{13}C are the frequently utilized nuclei in pharmaceutical science to study by qNMR due to high accessibility of these atoms in natural and synthetics compounds. However, the signal overlap, which originates when more than one carbon or proton have the same chemical environment, will significantly increase the spectral complexity and hamper qNMR analysis (Figure 4-2)[6]. Therefore, probing other NMR active nuclei such as ^{11}B, ^{31}P, and ^{15}N has been recently done for quantification and characterization of therapeutic molecules[7–9].

There are several motivations of performing ^{19}F qNMR to study the real time quantification of fluorinated drugs. ^{19}F nucleus has a high gyromagnetic ratio (γ) of 40.052 MHz*T^{-1} , comparable to the gyromagnetic ratio of ^{1}H 42.577 MHz*T^{-1} and enormously greater than ^{13}C 10.708 MHz*T^{-1}. Moreover, ^{19}F nucleus has 100% natural isotopic abundance, which is drastically higher than ^{13}C (1.1%). Parallel to proton, ^{19}F nucleus has nuclear spin of ½ which will yield a sharp signal and an easily interpreted spectra. ^{19}F NMR offers the advantage of a wide range of chemical shift from about -300 to 400 ppm compared to proton which has a very narrow chemical shift range (0-15ppm). Additionally, ^{19}F NMR may be more economical than ^{1}H since there is no need for deuterated solvents and the qNMR experiment can be obtained by using any solvent due to the absence of fluorine atoms in commonly used solvents[10–12].

Considering the downside of using ^{1}H and ^{13}C for quantitative analysis, in the current study, an investigation of a specific and direct method was developed and validated for a real-time solution-state quantitative fluorine nuclear magnetic resonance (^{19}F qNMR) method for the analysis of fluorine containing therapeutic molecules.

4.3 Materials and methods

4.3.1 Reagents

MVC was gifted by NIH, through the AIDS reagent program (USA). Addition MVC was purchased from ZhongShuo Pharmaceutical Technology Development Co.,Ltd. (Beijing, China). Alginic acid sodium salt (from brown algae, medium viscosity) were purchased from Sigma-Aldrich (St. Louis, MO, USA). Deionized water (DI water) was obtained through a Millipore Milli-Q water purification system (Millipore Corp., Danvers, MA). All other chemicals were of analytical grades and were used as obtained from suppliers.

4.3.2 ^{19}F qNMR method development

In order to accurately estimate the amount of drug, the integrated peak area of fluorine in MVC was chosen as our interest. ^{19}F qNMR spectroscopy was carried out on a Varian 400 MHz spectrometer (Palo Alto, CA, USA) with a Varian 2-channel probe. VnmrJ software (version 4.2A) was used for data acquisition and processing. The ^{19}F spectra were acquired at frequency 376.147 MHz. Preliminary analysis were performed such as an inversion recovery experiment to optimize the spin-lattice relaxation time, which was found to be ~0.2 s. Typically, most NMR active nuclei are fully relaxed after 5 times of T1, thus the relaxation delay was set to 1 s.

The linewidth of the NMR signal is directly dependent on T_2^* (the apparent spin-spin relaxation time). Large molecules such as polymers or proteins tend to have very small T_2^* values, which gives rise to very broad peaks. Therefore, it is expected that the integrated peak for a polymeric formulation of MVC will be very broad in comparison to free MVC (in solution) due to slow tumbling. Shimming was applied to each sample to maintain the same linewidth in each spectrum.

For all ^{19}F NMR experiments, the number of accumulated transients, and the pulse width were 256 and 45° (12.8μs), respectively, while the spectral width and FID acquisition time were 86486.5 Hz and 0.758s. The total acquisition time for each spectrum was around eight minutes. The sample spinning frequency was 20 Hz. Experiments were performed in triplicate and average integrated peak area values were determined. $C_6H_5CF_3$ (trifluoro-toluene) (in deuterated benzene) was used as ^{19}F q-NMR external standard for referencing and its chemical shift ($\delta \sim -63.72$ ppm) and peak resolution were assessed prior to any BTZ spectral acquisition. Typically, 650 μL of MVC samples were placed in a 5-mm outer diameter NMR tubes (Wilmad-LabGlass, Vineland, NJ, USA) and ^{19}F NMR experiments were conducted at 37ºC using a standard VT unit, unless specified otherwise. Baseline correction, phase adjustment, and integral calculations were carried out manually using MestReNova Lite (11.02.2, Escondido, CA, USA).

4.4 preparation of biological fluids and MVC samples

In this study, simulated vaginal fluid (VFS pH 4.2) and simulated semen fluid (SFS, pH 7.6) were utilized to conduct the drug release. Each fluid was prepared individually according to a published method[13]. Owen et. al. reported that the volume of normal human vaginal fluid is 0.75 mL, and the volume of human ejaculate is 3.4 ml. Therefore, VFS and SFS mixture (VSFS, pH 7.6) at 1:3 ratio was prepared to mimic the scenario of human ejaculate presence[13,14].

4.5 Method validation

^{19}F qNMR method was validated according to the International Conference on Harmonization (ICH) guidelines Q2(R1). Thus, several parameters (linearity, LOD, LOQ, specificity, precision, accuracy and robustness) were evaluated and the statistical variations within ^{19}F qNMR peak areas and/or MVC concentrations were presented as percent relative standard error (%RSE), as explained in chapter 2.

In order to construct the standard curves of the method, six different concentrations of MVC (0.42- 15 mg/ml) were prepared by serial dilution of a standard (15 mg/ml) in VFS and VSFS respectively. ^{19}F NMR peak's area under the curve was then plotted in relation to MVC concentrations in VFS and VSFS. The intercept, slope, and coefficient of determination (R^2) values were obtained by linear regression analysis.

Specificity of ^{19}F qNMR was tested using two different fluorinated compounds .To evaluate the accuracy of ^{19}F qNMR, four (4) quality controls (QC) were used with concentration (15, 10, 7, and 5 mg/ml). Robustness was verified by varying two parameters: pulse width (µs), and relaxation delay (s).

4.6 Preparation of alginate microparticles

Alginate microparticle formulation of MVC was prepared according to a published method, with minor modifications[15]. Accordingly, alginic acid sodium salt and MVC were added to 150 ml of a solution of 15% VFS and VSFS (in DI water, pH 7.2) at a ratio of 4:1. The mixture was stirred at room temperature (25 °C) until both the drug and polymer were completely dissolved. The solution was then spray-dried on a Buchi Mini Spray Dryer, Model 290 (Buchi Laboratoriums Technik AG, Flawil, Switzerland). The spray dryer inlet temperature was T = 120

°C, the outlet temperature at the collector was 32°C, the aspirator was maintained at 85%, the pump rate was 10%, and the nozzle cleaner was set at 7. Dried microparticle powder was collected from the instrument and stored at 4 °C for further analysis.

4.7 Physicochemical characterization

4.7.1 Size and surface charge

MVC microparticle size and zeta potential (ζ-potential) measurements were conducted by dynamic light scattering (DLS) on a Malvern instrument 3600 Zetasizer Nano (Worcestershire, UK). Essentially, 1 mL of sample suspension (in DI water) was prepared in a disposable size measurement cuvette and briefly sonicated (20 s) using an ice bath sonication (Qsonica LLC, Newtown, CT, USA). Surface charge density (ζ-potential) measurements were conducted by transferring a sonicated sample into DTS 1070 Zetasizer disposable folded capillary cells (Malvern Instruments, Northampton, MA, USA). Size and ζ-potential cuvettes were then placed in the cell area one after another, and experiments were performed at 25 °C on the Zetasizer instrument. Data acquisition and analysis were conducted using Zetasizer software (version 6.01, Worcestershire, UK). Preceding any DLS measurements, the instrument was calibrated using nanosphere size standards (60.0 ± 4 nm) and ζ-potential transfer standards (−42.0 ± 4.2 mV) obtained from Malvern Instruments (Northampton, MA, USA).

4.7.2 Fourier transform infrared spectroscopy (FTIR)

The IR spectra were acquired on Nicolet IS10 FTIR instrument (Thermo Fisher Scientific, Madison, WI, USA) equipped with a Zinc selenide (ZnSe) crystal. The instrument was used in the Attenuated Total Reflectance (ATR) mode. A resolution of 4 cm^{-1} and a sample scan of 228 were fixed as basic acquisition parameters. Transmittance IR spectra were acquired between 4000 and 650 cm^{-1}. For better spectral resolution, all samples were allowed to make intimate contact with the ATR ZnSe crystal's surface by pressing them with a built-in pressure clamp. FTIR spectra were collected and analyzed with OMNIC Specta Software (Thermo Fisher Scientific, Madison, WI, USA). Typically, the average IR spectrum acquisition time was 6 minutes.

4.7.3 **Scanning electron microscopy (SEM)**

To analyze MVC microparticles' morphology, SEM imaging was conducted on a field-emission environmental SEM Philips XL30 instrument (Hillsboro, OR, USA). Consequently, a small amount of dried microparticles was sprayed onto a stub covered with an adhesive conductive carbon tab. Excess material was removed using a paintbrush, and the sample was sputter-coated with a thin layer of gold. Images were acquired at an accelerating voltage of 5 kV.

4.7.5 Drug release kinetics

In this study, MVC real-time release from an alginate microparticle formulation vaginal fluid stimulant (VFS) and a mixture of vaginal fluid stimulant and seminal fluid stimulant (VSFS) was assessed by ^{19}F qNMR, and the release profile was compared to a control condition performed in a dialysis bag. Concisely, a dispersion of alginate microparticles (10 mg/mL) was prepared in VFS and VSFS and immediately transferred into an NMR tube. Time dependent MVC release (% drug release) was further determined by acquiring 50 ^{19}F NMR spectra in 5 hours release at 37 °C. In a separate experiment, an alginate microparticle sample was prepared at 10 mg/mL in VFS and VSFS and immediately placed into a dialysis bag (Spectra/Por Float-A-Lyzer G2, MWCO 8–10 kDa; Spectrum Laboratories, Inc., Rancho Dominguez, CA, USA). The dialysis tube was further immersed into a VFS and VSFS bath (15 mL), and the mixture was placed in a thermostatic water bath at 37 °C, under shaking at 60 rpm. Sample aliquots (1 mL) were collected at predetermined time points (5, 10, 20, 40, 80, 160, 320, and 640 min) from the receiving compartment, and MVC concentration was determined by ^{19}F qNMR. The sink condition was maintained by adding 1 ml of free VFS and VSFS solution in the outer receiving dialysis compartment following each sample collection. All experiments were conducted in triplicate (n = 3), and the time dependent MVC release (% drug release) curve was determined from the calibration curve, by processing the ^{19}F qNMR spectra and getting the area under the curve (AUC). Unlike the dialysis method, in the direct NMR release method, the drug molecules released from the microparticles formulation do not have to diffuse through a separating membrane before they can be collected and analyzed by qNMR. Thus, drug molecules released in the NMR tube's method are directly analyzed as soon as they are released from the alginate microparticles.

4.8 Results and discussion

4.8.1 ^{19}F-qNMR method development and validation

The ^{19}F qNMR method was developed and validated based on ICH Q2(R1) guidelines. The method was linear in the concentration range tested of MVC in VFS and VSFS (0.43-15 mg/ml or 0.83-29.2 mM) (Figure4-3&4). The linear equations are $y = 5595.1x - 231.98$(in VFS), and $y = 4421.7x - 329.74$ (in VSFS). The coefficient of determination (R^2) in VFS and VSFS are 0.9978 and 0.9995 respectively. Although the LOD and LOQ values, (LOD=0.97mg/ml, LOQ=2.93mg/ml), obtained by ^{19}F NMR spectroscopy are substantially higher than the values reported using UV spectroscopy (0.1028 and 0.315µg/ml)[16], several qNMR methods have been reported in the field of pharmaceutical research and the LOD and LOQ obtained are consistent with the range of ^{19}F qNMR method[7,8]. Comparing qNMR method sensitivity with other analytical methods such as UV and HPLC, qNMR method has lower sensitivity. It has been found that the LOD and LOQ of ^{1}H qNMR, ^{31}P qNMR and ^{11}B qNMR were higher compared to their respective method in HPLC[7,8].

The specificity of the ^{19}F qNMR method of MVC was tested. The peaks of two fluorinate compounds did not interfere with the peak of MVC, and it could be accurately quantified (Figure4-5). The ^{19}F qNMR method of MVC was accurate with all percent mean recovery values within 100 ± 10% and %RSE values <2%, for both intra-day and inter-day recovery studies in VFS and VSFS (Table 4-1&2). The method was also precise and %RSE values for intra-day and inter-day precision analysis were <2% for all four QC samples tested in both VFS and VSFS (Table 4-3&4). These results were consistent with ICH guidelines and confirmed the closeness of agreement (reproducibility) between the AUC values of ^{19}F qNMR spectra for each QC sample.

The ^{19}F qNMR method's robustness was verified by varying three different NMR instrumental parameters. Table 4-5 shows that the method was robust and not affected by changing any parameter as all %RSE were < 2%.

4.8.2 Physicochemical characterization

Following the preparation of spray-dried MVC/Alg microparticles, average particle size and ζ-potential measurements were conducted on the Zetasizer Nano instrument. Figures 4-6 A and B summarize the size and surface charge density analysis of the microparticle formulation. Although it is routinely used for nanomaterial characterization, the Zetasizer Nano instrument is suitable for microparticle surface charge density and size measurements (≤10 μm)[17]. The MVC/Alg microparticle average particle size was 2.522 ± 0.19 μm, and the polydispersity index (PDI) was 0.559. The microparticles were negatively charged, and the average ζ-potential was −61.3.1 ± 2.2 mV. The strong negative charge is likely due to the carboxylate group of alginic acid sodium salt, which is expected to be fully deprotonated (ionized) in neutral pH conditions (alginic acid's pKa ∼ 3.4–4.4). The SEM image revealed that individual BTZ/Alg microparticles are spherical in shape with varying size and morphology. Nevertheless, the average particle size was consistent with the Zetasizer measurements. In FT-IR spectra (Figure 4-7), all the bands observed in MVC/Alg microparticle were consistent with the bands observed in Alg and MVC IR spectra.

4.8.3 MVC in vitro drug release

The developed and validated ^{19}F qNMR method was applied for the real-time release study and quantification of MVC from alginate microparticles (MP) fabricated using spay drying technique. In the case of the direct ^{19}F qNMR measurements in the NMR tube, a significant burst release of MVC was observed in both VFS and VSFS (Figures 4-8&9). In addition, an equilibrium in the MVC profile was achieved, where ~100% of the drug was released in about 20 minutes.

In order to achieve a more slow and steady release of MVC from our MP formulation, a cross-linking process by ionic interaction with divalent cations, such as Ca^{2+}, Ba^{2+}, and Sr^{2+} can be performed. The cross-linking process is believed to arise as a result of the linkage between these divalent cations and guluronate regions on the alginate backbone[18].

Alternatively, a pH sensitive polymer can be explored in the development of MVC microparticles formulation. A pH sensitive polymer like Eudragit S-100 can be used as a model pH sensitive polymer for the encapsulation of MVC. The rationale is that Eudragit which is soluble above pH 7, and at low pH values (~4.2-5) MVC would release slowly, while at neutral pH (~7.6), there would be a faster release of MVC from Eudragit MPs[19].

4.9 Conclusion

In this study, ^{19}F qNMR method was developed and validated according to the ICH Q2R(1) guidelines. The method was linear, specific for MVC, precise, accurate and robust. The ^{19}F qNMR method was applied to study the real time quantification of MVC drug release from an alginate microparticle formulation. Based on the results obtained by ^{19}F NMR, MVC was released completely within 20 minutes in both VFS and VSFS. Future work will include controlling the release profile of MVC from microparticle using cross linking process and a pH sensitive polymer.

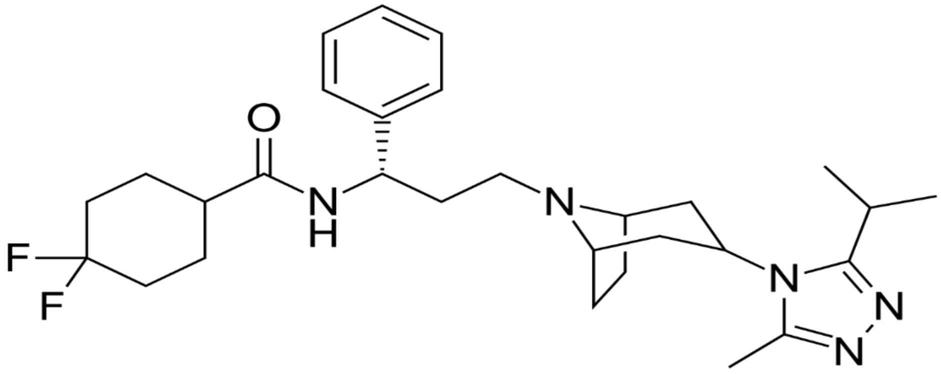

Figure 4-1. Maraviroc

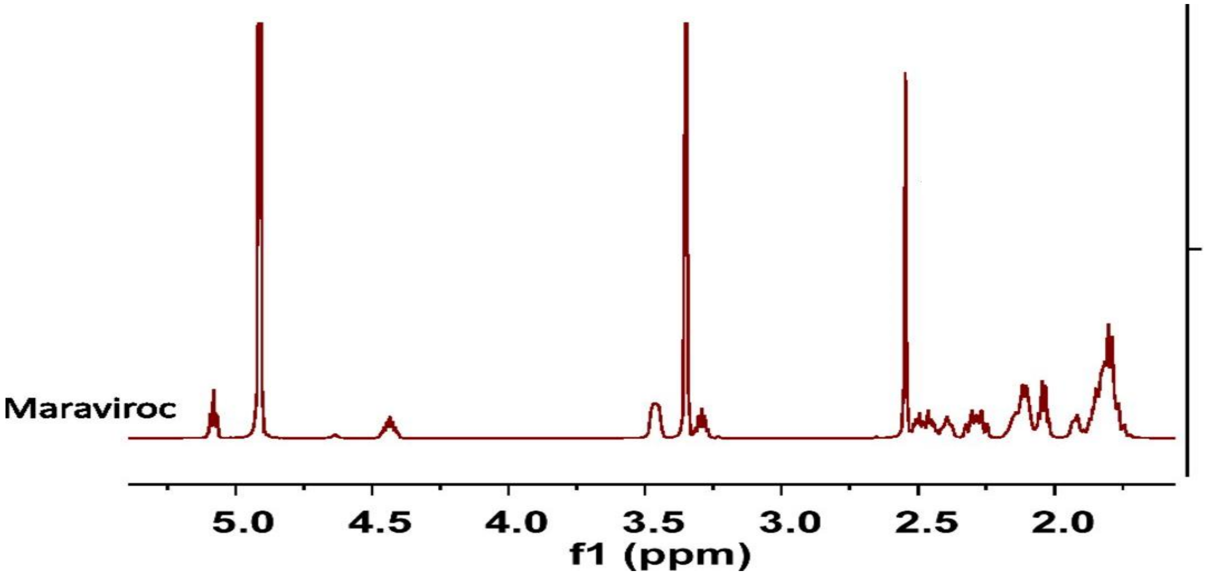

Figure 4-2. Proton NMR spectra of Maraviroc

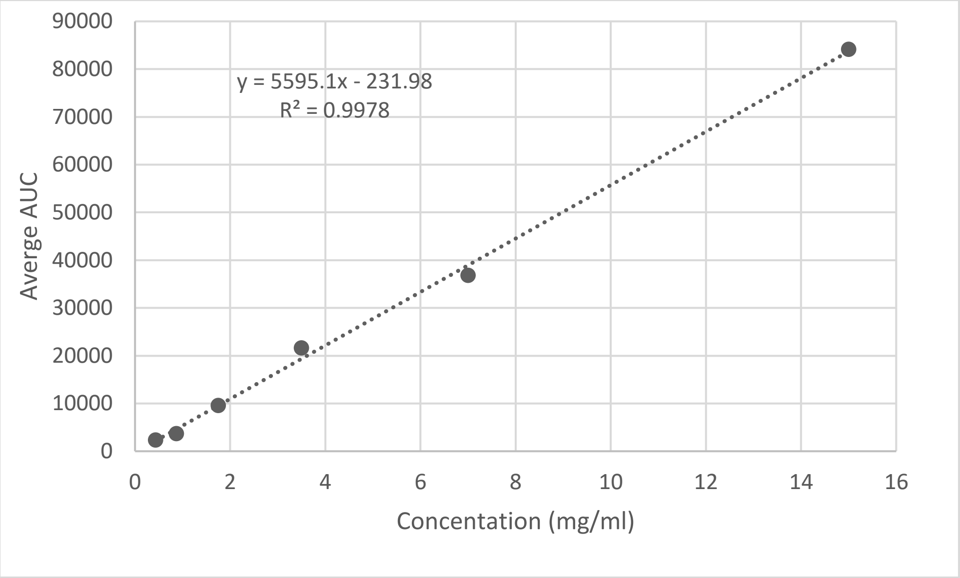

Figure 4-3. Calibration curve of Maraviroc in VFS

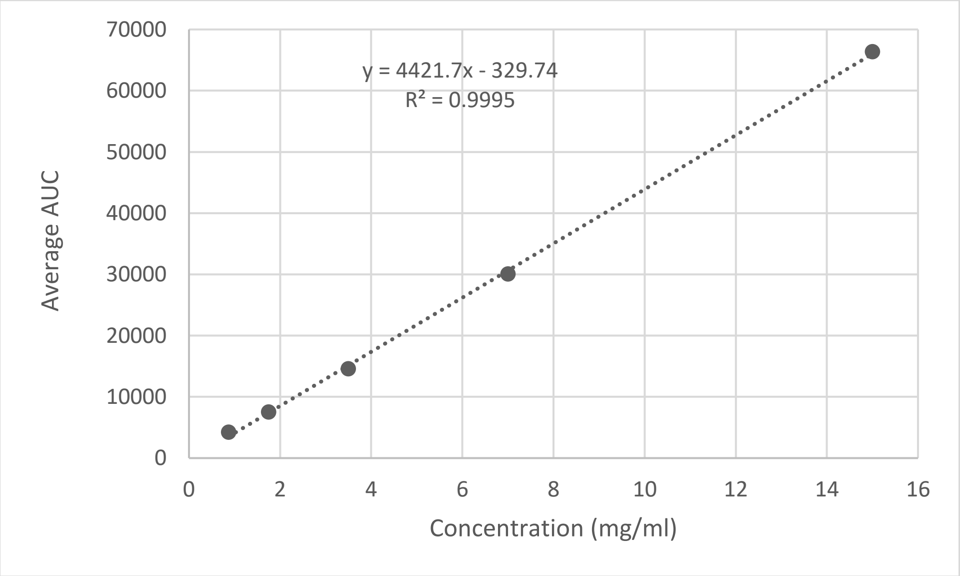

Figure 4-4. Calibration curve for Maraviroc in VSFS

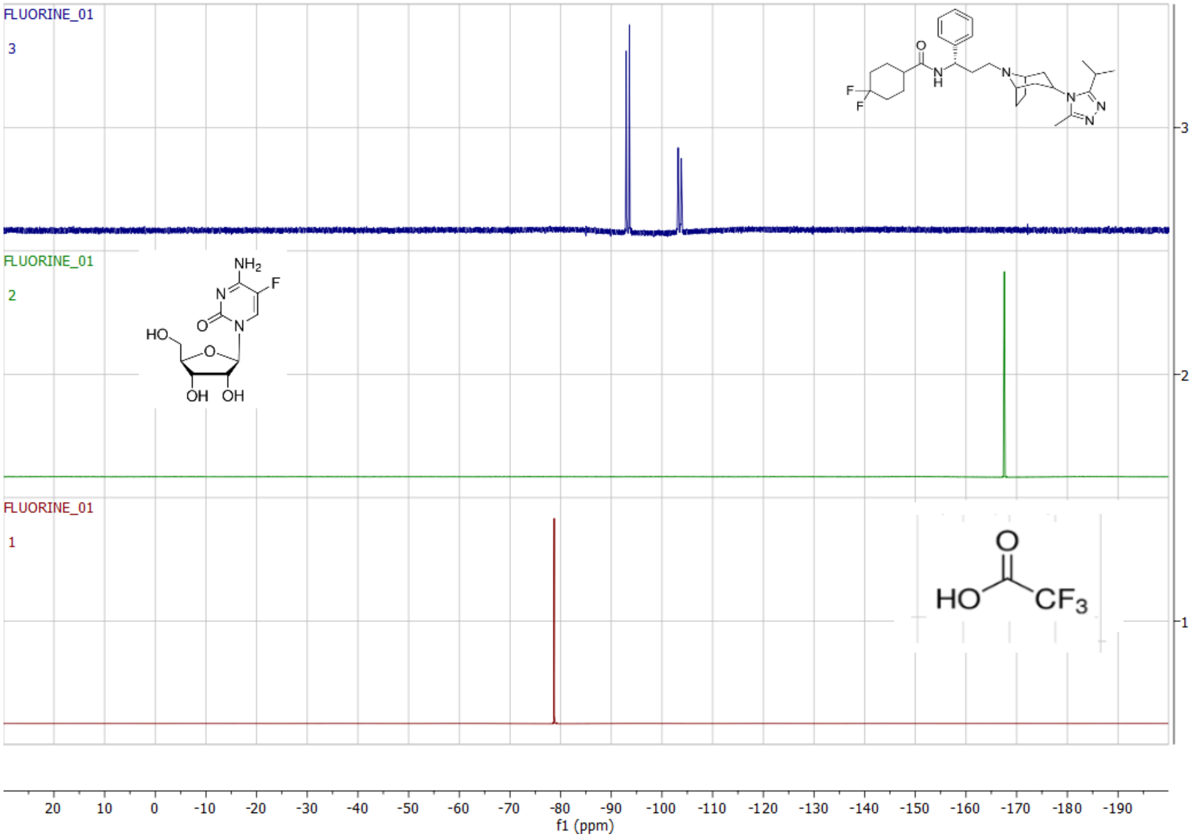

Figure 4-5. Specificity of 19F qNMR method in presence of other possible contaminants

Table 4-1. Accuracy of ^{19}F qNMR method in VFS represented as percent mean recovery

MVC Concentration (mg/ml)	% Mean recovery ± %RSE[a] (n = 3)		
	Intra-day	Inter-day	
	Within-day (Day 1)	Day 2	Day 3
15	100.45±0.9	97.30±0.88	95.40±0.45
10	98.37±0.69	99.14±0.31	74.93±0.31
7	94.70±0.63	94.56±0.26	92.12±1.54
5	98.76±0.73	99.09±0.91	99.53±0.10

Table 4-2. Accuracy of ^{19}F qNMR method in VSFS represented as percent mean recovery

MVC Concentration (mg/ml)	% Mean recovery ± %RSE[a] (n = 3)		
	Intra-day	Inter-day	
	Within-day (Day 1)	Day 2	Day 3
15	±0.9	97.30±0.88	95.40±0.45
10	98.37±0.69	99.14±0.31	74.93±0.31
7	94.70±0.63	94.56±0.26	92.12±1.54
5	98.76±0.73	99.09±0.91	99.53±0.10

Table 4-3. Precision of the ^{19}F qNMR method in VFS represented as percent relative standard error

Concentration (mg/ml)	Intra-day		Inter-day					
	Within-day		day1		day2		day3	
	peak area*10^5	%RSE	peak area*10^5	%RSE	peak area*10^5	%RSE	peak area*10^5	%RSE
15	0.8281	0.9	0.8281	0.9	0.8291	0.9	0.7906	0.9
	0.8503		0.8503		0.8072		0.8023	
	0.8464		0.8464		0.8065		0.8022	
10	0.5513	0.7	0.5513	0.7	0.5518	0.3	0.4204	0.3
	0.5585		0.5585		0.5496		0.4146	
	0.5428		0.5428		0.5556		0.4158	
7	0.3715	0.66	0.3715	0.66	0.3687	0.2	0.3602	0.2
	0.3636		0.3636		0.366		0.3679	
	0.3705		0.3705		0.3694		0.3472	
5	0.27	0.73	0.27	0.73	0.2799	0.9	0.2058	0.9
	0.2749		0.2749		0.2732		0.2059	
	0.2769		0.2769		0.2715		0.2067	

Table 4-4. Precision of the ^{19}F qNMR method in VSFS represented as percent relative standard error

Concentration (mg/ml)	Intra-day		Inter-day					
	Within-day		day1		day2		day3	
	peak area*10^5	%RSE	peak area*10^5	%RSE	peak area*10^5	%RSE	peak area*10^5	%RSE
	0.61		0.61		0.62		0.62	
15	0.58	0.01	0.58	0.01	0.63	0.0003	0.62	4.61E-05
	0.62		0.62		0.62		0.62	
	0.45		0.45		0.45		0.45	
10	0.44	0.003	0.44	0.003	0.45	0.0072	0.45	0.0005
	0.45		0.45		0.44		0.45	
	0.29		0.29		0.29		0.29	
7	0.30	0.01	0.30	0.01	0.29	0.001	0.30	0.004
	0.29		0.29		0.29		0.29	
	0.21		0.21		0.20		0.20	
5	0.20	0.008	0.20	0.008	0.20	0.015	0.20	0.001
	0.20		0.20		0.21		0.20	

Table 4-5. Robustness of ^{19}F qNMR in VFS

NMR parameter		Average area under curve AUC[a] (10^5)	%RSE[b]
Pulse width (μs)	12.4	0.36	0.13
	12.8	0.36	0.03
	13.2	0.36	0.02
Relaxation delay (s)	0.8	0.86	0.01
	1	0.36	0.02
	1.4	0.37	0.09

Table 4-6. Robustness of ^{19}F qNMR in VSFS

NMR parameter		Average area under curve AUC[a] (10^5)	%RSE[b]
Pulse width (μs)	12.4	0.36	0.13
	12.8	0.36	0.03
	13.2	0.36	0.02
Relaxation delay (s)	0.8	0.86	0.01
	1	0.36	0.02
	1.4	0.37	0.09

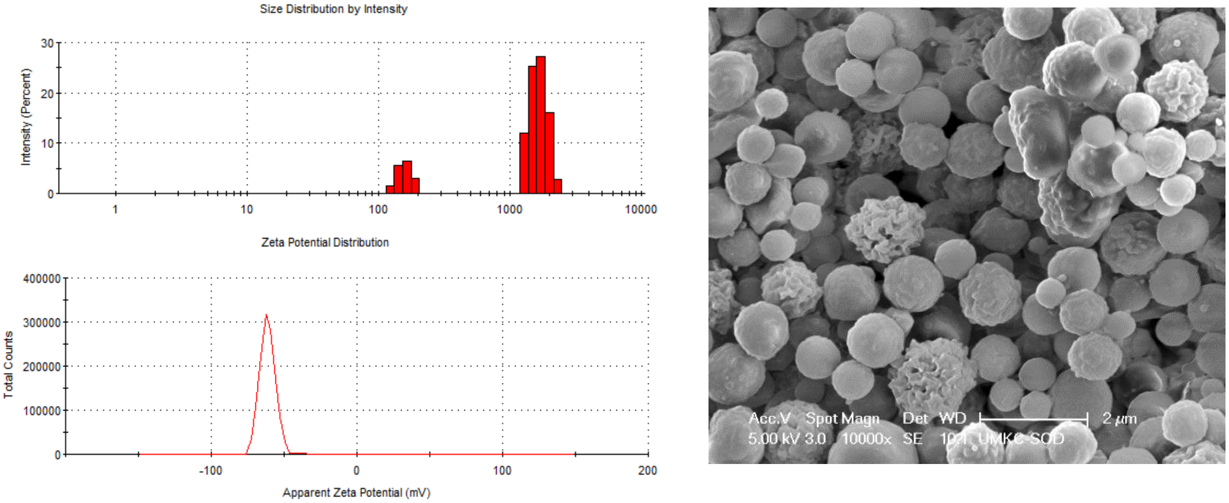

Figure 4-6. Average particle size diameter (A), surface charge density (B), and SEM image of MVC/Alg micorparicle formulation.

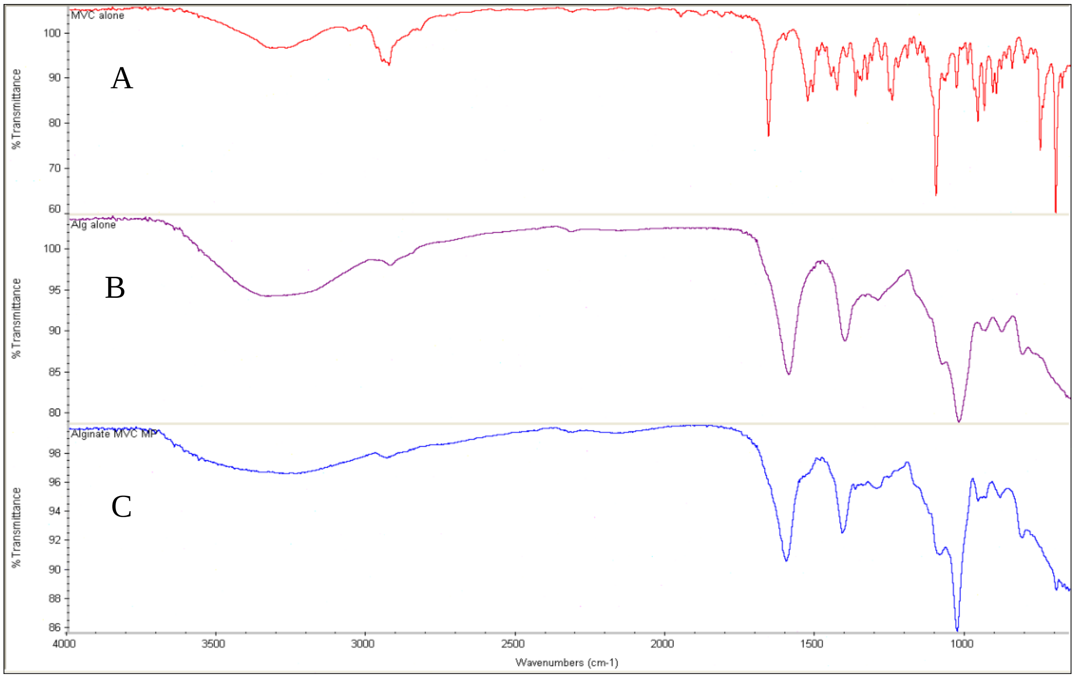

Figure 4-7. FT-IR Spectra of (A) maraviroc, (B) alginate, and (C)alginate microparticles

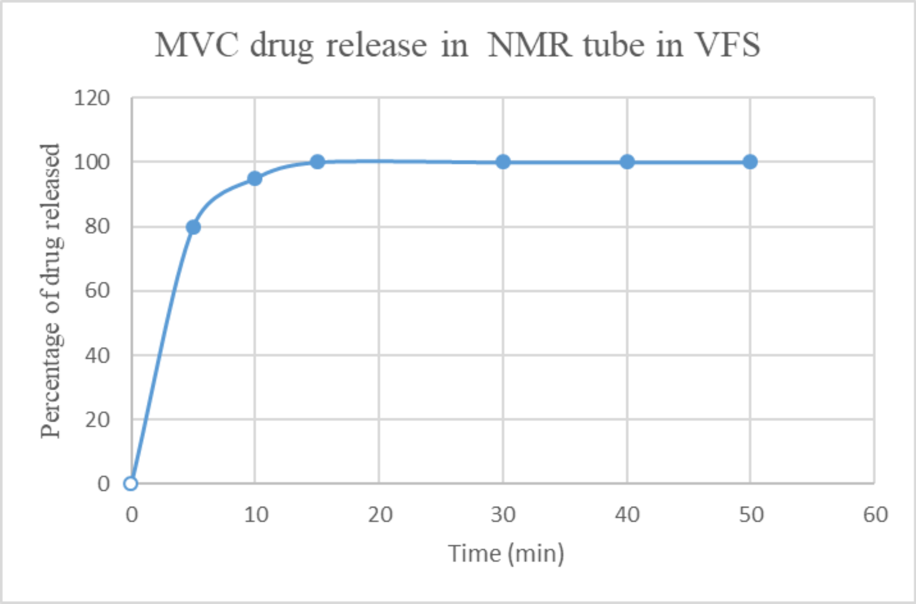

Figure 4-8. Percent cumulative drug release profiles of MVC from MVC/Alg microparticles in VFS

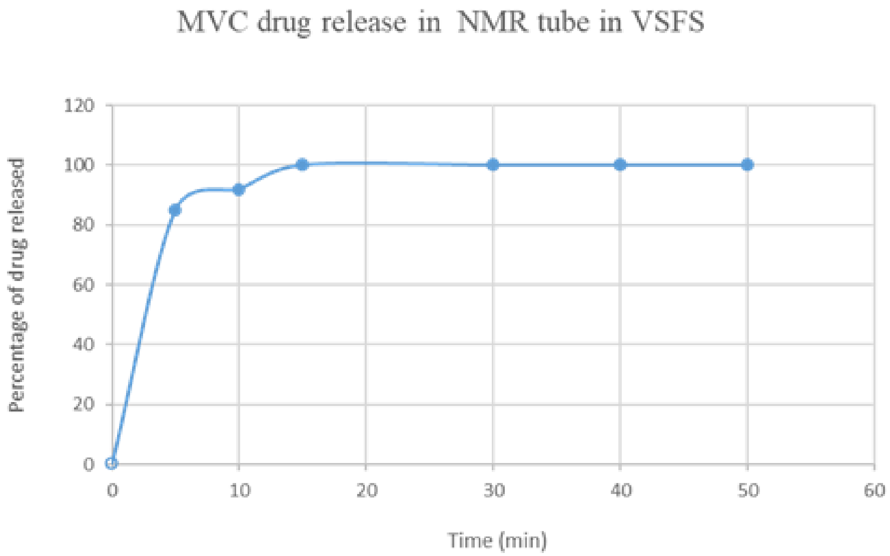

Figure 4-9. Percent cumulative drug release profiles of MVC from MVC/Alg microparticles in VSFS

References

(1) Owusu, E. D. A.; Cofie, N. S.; Nai, E. A.; Klipstein-Grobusch, K.; Brown, C. A.; Mens, P. F.; Grobusch, M. P. Malaria, Sickle Cell Disease, HIV, and Co-Trimoxazole Prophylaxis: An Observational Study. *Int. J. Infect. Dis.* **2018**, *69*, 29–34. https://doi.org/10.1016/j.ijid.2018.01.031.

(2) Lieberman-Blum, S. S.; Fung, H. B.; Bandres, J. C. Maraviroc: A CCR5-Receptor Antagonist for the Treatment of HIV-1 Infection. *Clin. Ther.* **2008**, *30* (7), 1228–1250. https://doi.org/10.1016/S0149-2918(08)80048-3.

(3) maraviroc https://en.wikipedia.org/wiki/Maraviroc.

(4) Ball, C.; Woodrow, K. Electrospun Solid Dispersions of Maraviroc for Rapid Intravaginal Preexposure Prophylaxis of HIV. *Antimicrob. Agents Chemother.* **2014**, *58* (8), 4855–4865. https://doi.org/10.1128/AAC.02564-14.

(5) Vincent, K. L.; Moss, J. A.; Marzinke, M. A.; Hendrix, C. W.; Anton, P. A.; Pyles, R. B.; Guthrie, K. M.; Dawson, L.; Olive, T. J.; Butkyavichene, I.; et al. Safety and Pharmacokinetics of Single, Dual, and Triple Antiretroviral Drug Formulations Delivered by Pod-Intravaginal Rings Designed for HIV-1 Prevention: A Phase I Trial. *PLOS Med.* **2018**, *15* (9), e1002655. https://doi.org/10.1371/journal.pmed.1002655.

(6) Tseng, E.; Fate, G. D.; Walker, G. S.; Goosen, T. C.; Obach, R. S. Biosynthesis and Identification of Metabolites of Maraviroc and Their Use in Experiments to Delineate the Relative Contributions of Cytochrome P4503A4 versus 3A5. *Drug Metab. Dispos.* **2018**, *46* (5), 493–502. https://doi.org/10.1124/dmd.117.079855.

(7) Coulibaly, F. S.; Alnafisah, A. S.; Oyler, N. A.; Youan, B.-B. C. Direct and Real-Time

Quantification Of Bortezomib Release From Alginate Microparticles Using Boron (11 B) Nuclear Magnetic Resonance Spectroscopy. *Mol. Pharm.* **2019**, *16* (3), 967–977. https://doi.org/10.1021/acs.molpharmaceut.8b00873.

(8) Agrahari, V.; Meng, J.; Purohit, S. S.; Oyler, N. A.; Youan, B. B. C. Real-Time Analysis of Tenofovir Release Kinetics Using Quantitative Phosphorus (31P) Nuclear Magnetic Resonance Spectroscopy. *J. Pharm. Sci.* **2017**, *106* (10), 3005–3015. https://doi.org/10.1016/j.xphs.2017.03.043.

(9) Levy, G. C.; Pehk, T.; Srinivasan, P. R. Quantitative15N NMR Spectroscopy. *Org. Magn. Reson.* **1980**, *14* (2), 129–132. https://doi.org/10.1002/mrc.1270140210.

(10) Wang, J.; Sánchez-Roselló, M.; Aceña, J. L.; del Pozo, C.; Sorochinsky, A. E.; Fustero, S.; Soloshonok, V. A.; Liu, H. Fluorine in Pharmaceutical Industry: Fluorine-Containing Drugs Introduced to the Market in the Last Decade (2001–2011). *Chem. Rev.* **2014**, *114* (4), 2432–2506. https://doi.org/10.1021/cr4002879.

(11) Okaru, A. O.; Brunner, T. S.; Ackermann, S. M.; Kuballa, T.; Walch, S. G.; Kohl-Himmelseher, M.; Lachenmeier, D. W. Application of 19F NMR Spectroscopy for Content Determination of Fluorinated Pharmaceuticals. *J. Anal. Methods Chem.* **2017**, 7. https://doi.org/10.1155/2017/9206297.

(12) Ando, S.; Harris, R. K.; Scheler, U. Fluorine-19 NMR of Solids Containing Both Fluorine and Hydrogen. In *Encyclopedia of Magnetic Resonance*; John Wiley & Sons, Ltd: Chichester, UK, 2007; Vol. 9, pp 531–550. https://doi.org/10.1002/9780470034590.emrstm0171.

(13) Owen, D. H.; Katz, D. F. A Vaginal Fluid Simulant. *Contraception* **1999**, *59* (2), 91–95. https://doi.org/10.1016/S0010-7824(99)00010-4.

(14) Owen, D. H. A Review of the Physical and Chemical Properties of Human Semen and the Formulation of a Semen Simulant. *J. Androl.* **2005**, *26* (4), 459–469. https://doi.org/10.2164/jandrol.04104.

(15) Meng, J.; Agrahari, V.; Ezoulin, M. J.; Purohit, S. S.; Zhang, T.; Molteni, A.; Dim, D.; Oyler, N. A.; Youan, B.-B. C. Spray-Dried Thiolated Chitosan-Coated Sodium Alginate Multilayer Microparticles for Vaginal HIV Microbicide Delivery. *AAPS J.* **2017**, *19* (3), 692–702. https://doi.org/10.1208/s12248-016-0007-y.

(16) Notari, S.; Tommasi, C.; Nicastri, E.; Bellagamba, R.; Tempestilli, M.; Pucillo, L. P.; Narciso, P.; Ascenzi, P. Simultaneous Determination of Maraviroc and Raltegravir in Human Plasma by HPLC-UV. *IUBMB Life* **2009**, *61* (4), 470–475. https://doi.org/10.1002/iub.181.

(17) Islam, P.; Water, J.; Bohr, A.; Rantanen, J. Chitosan-Based Nano-Embedded Microparticles: Impact of Nanogel Composition on Physicochemical Properties. *Pharmaceutics* **2016**, *9* (4), 1. https://doi.org/10.3390/pharmaceutics9010001.

(18) Szekalska, M.; Sosnowska, K.; Czajkowska-Kośnik, A.; Winnicka, K. Calcium Chloride Modified Alginate Microparticles Formulated by the Spray Drying Process: A Strategy to Prolong the Release of Freely Soluble Drugs. *Materials (Basel).* **2018**, *11* (9), 1522. https://doi.org/10.3390/ma11091522.

(19) Zhang, C.; Zhang, T.; Oyler, N. A.; Youan, B. B. C. Direct and Real-Time Quantification of Tenofovir Release from Ph-Sensitive Microparticles into Simulated Biological Fluids Using1H Nuclear Magnetic Resonance. *J. Pharm. Sci.* **2014**, *103* (4), 1170–1177. https://doi.org/10.1002/jps.23886.

Chapter 5 . CHARACTERIZATION OF AN ICOSAHEDRAL CLOSOMER-BASED SYNTHETIC LECTIN APPROACH FOR HIV VIRIONS CAPTURE USING 11B NMR SPECTROSCOPY

5.1 Introduction

The Human immunodeficiency virus (HIV) is one of the global epidemics that afflicts human civilization and concerns people worldwide. It is responsible for the acquired immune deficiency syndrome (AIDS). The first case was discovered in United States in 1981[1] . Scientists believed that the monkey was the original source of HIV/AIDS in humans. They discovered that the chimpanzees in West Africa carried the same type of HIV virus known as simian immunodeficiency virus (SIV)[2,3]. Moreover, they found that SIV is closely related to HIV[4]. The virus was transferred to humans when hunters were exposed to infected blood. The lack of knowledge about this virus contributes to increases in HIV/AIDS. The HIV virus attacks the immune system in the human body, mainly CD4 cells (T cells), which is responsible for defending against diseases. Untreated HIV will result in a severe reduction of the CD4 cells; hence it will make the body more likely to get other infections. Ultimately, HIV will destroy all CD4 cells resulting in a very weak body. At that stage, it is a sign that the person has AIDS, which is the last stage of HIV infection. In the mid-1990s, people who had HIV virus reached the AIDS stage rapidly. However, with the medicine progression, HIV can be controlled but not effectively treated by using a medicine called antiretroviral therapy (ART). Taking the medicine regularly delays the advancement of the virus and reduces the possibility of transmitting the virus to others.

When HIV occurs, the virus targets the CD4 cells. There are several phases for HIV viral entry as shown in (Figure 5-1)[5]. The first step of viral entry is binding of the envelope glycoprotein (gp120), which is located on the surface of HIV envelope, to its primary receptor CD4, a glycoprotein found on the surface of immune cells. As a result of this binding, the second step of viral entry will take place by doing some conformational rearrangements and CD4 will build a bridge sheet with the virus. The third step of viral entry is binding to c-c chemokine receptor type 5 (known as CCR-5). Then the fourth step involves the movement of virus particles to a position where a membrane penetration can occur. The fifth and the final step of the viral entry is membrane fusion.

HIV has heavily glycosylated surface glycoproteins (HIV gp120/HIV gp41). It is reported that approximately half of HIV envelope glycoprotein (HIV gp120) molecular mass is composed of carbohydrates, which are mostly mannose oligo-mannose glycans ($Man_{5\text{-}9}$) [6–9]. HIV gp120 high glycan content is believed to promote host cell recognition, immune evasion, enhanced infectivity and resistance [10,11]. HIV prevention strategies targeting glycans on HIV viral envelope and transmembrane glycoproteins (HIV gp120/ HIV gp41) have emerged as potentially viable viral entry inhibition approaches [12]. In general, natural lectins extracted from plants, animals or bacteria have been used to target specific HIV gp120 glycan structures[13]. Binding of natural lectins to oligomannoglycans, covering the underlying amino acids in HIV gp120, could potentially hinder a proper interaction between the virus and its target cells or affect HIV gp120/ HIV gp41 post-binding conformational alterations, which are critical for viral entry and/or infectivity [13]. Among others, Griffithsin, an algae-derived lectin, and BanLec, a fruit lectin extracted from banana, have shown remarkable anti-HIV activity [14] Furthermore, concanavalin A (Con A) immobilized polystyrene nanospheres formulations were shown to strongly bind to HIV gp120 and significantly reduced HIV-1 viral infectivity [15,16].

Due to limitations such as mitogenecity, solubility, resistance and cost of manufacturing associated with natural lectins used as anti-HIV agents, synthetic lectins are increasingly being explored as alternative lectin-based HIV entry inhibitors. Synthetic lectins, which are essentially composed of boronic acids, are cheaper to synthesize, manufacture, purify and commercialize[17]. Conceptually, synthetic lectins exert their antiviral activity taking advantage of the boronic acids functional group's ability to form stable boronic esters with diols, such as those found in carbohydrates on HIV gp120[18]. The formation of stable boronic esters with HIV surface glycans might lead to HIV "virions capture" which might prevent viral entry and replication[16]. Benzoboroxole functionalized polymers, proposed by Mahalingam et al.[17], were shown to significantly inhibit HIV infectivity (EC_{50} = 15 nM at 75 mol % BzB). Furthermore, monophenylboronic acids-based carbohydrate binders were synthesized and tested by Trippier et al. for their antiviral potential[19]. This study was followed up by the synthesis and analysis of a series of bisphenylboronic acids-based carbohydrate binders[20]. Although the mono and bisphenylboronic acids did not demonstrate any pronounced antiviral activities, these compounds did show low cytotoxicity in human T-lymphocyte cells culture. The lack of strong HIV gp120 binding activity demonstrated by mono and bisphenylboronic acids was attributed to their small size and the lack of multivalency in those compounds. By addressing the multivalency and size limitation observed with mono and bisphenylboronic acids, we hypothesized that a phenylboronic acid (PBA) closomer nanoscaffold could strongly bind to HIV gp120. Closomers are derivative of dodecahydroxy-closo-dodecaborate ($[closo - B_{12}OH_{12}]^{2-}$) and have gained increasing attention in drug design and delivery[21,22]. taking advantage of the so-called "vertex differentiation" approaches, closomers virtually allow 12 different cargos attachment to the boron cage[23]. This may open new avenues for combination therapies[24–26] and the development of novel theranostic applications where targeting ligand(s), therapeutic agent(s) and imaging agent(s) are often combined in a single nanocarrier[11,27,28]. Closomers have demonstrated very low toxicity in animal studies[27,29] suggesting that these scaffolds might represent a safe and effective drug delivery alternative to polymeric nanocarriers[30]. Furthermore, the ability to synthesize uniform closomer nanoscaffolds could potentially address the size, composition and structural heterogeneity generally observed in polymeric nanocarriers[31].

5.2 General research approach

The objectives of this project are:

A Phenylboronic Acid (PBA)-immobilized closomer nanocomplex could be used as an entry inhibitor by capturing HIV virions, thus preventing HIV sexual transmission. Phenyl boronic Acid (PBA) are known to form boronic acid in the presence of cis-diol, like the one found in HIV-gp120 glycoproteins. To test this hypothesis:

1. A derivative of Phynel boronic acid (PBA) was synthesized
2. ^{11}B NMR spectroscopy as well as FT-IR spectroscopy were utilized as a characterization tool for the reaction progression.
3. Biological studies will be performed to test the binding affinity between HIV/GP21 and the derivative of PBA.

5.3 Experimental methods

5.3.1 Chemicals and reagents.

Cesium dodecahydrododecaborate $Cs_2[closo-B_{12}H_{12}]$ was obtained from Strem Chemicals (Newburyport, MA, USA). Hydrogen peroxide solution (H_2O_2) 30 % (w/w) in water; Tetrabutylammonium hydroxide (TBA) solution ~40% in water; 4-(Bromomethyl)phenylboronic acid (PBA), N,N-Diisopropylethylamine and Acetonitrile are purchased from Sigma-Aldrich (St. Louis, MO, USA). Dowex® 50 WX8-200 cation-exchange resin was purchased from GFS Chemicals. CM5 sensor chips; HBS-EP buffer [0.01 M HEPES pH 7.40, 15 M NaCl, 3 mM EDTA, 0.005% (v/v), surfactant P20); amine coupling kit [1-Ethyl-3-(3-dimethylaminopropyl) carbodiimide hydrochloride (EDC), 750 mg N-Hydroxysuccinimide (NHS), 115 mg 1.0 M Ethanolamine-HCl pH 8.5]; immobilization buffer [10 mM sodium acetate pH 4.0] and regeneration solutions [50 mM NaOH] were purchased from GE Healthcare Bio-Sciences (Pittsburgh, PA, USA). Human vaginal keratinocytes cell line (VK2/E6E7, ATCC Number CRL-2616) and Murine macrophage [RAW 264.7 (TIB-71)] were obtained from the American Type Culture Collection (Manassas, VA, USA). Resazurin sodium salt, neutral red (NR), sodium nitroprusside dehydrate (SNP), Dulbecco's Phosphate-Buffered Saline (DPBS), acetic acid, ethyl alcohol (ethanol) pure 200 proof ACS reagent (≥99.5%), Triton™ X-100 and lipopolysaccharides (LPS). Dulbecco's Modified Eagle Medium (DMEM) and keratinocyte serum-free medium (1X) (K-SFM) were purchased from Thermo Fisher Scientific (Waltham, MA, USA). 3-(4,5-dimethylthiazol-2-yl)-5-(3-carboxymethoxyphenyl)-2-(4-sulfophenyl)-2H-tetrazolium inner salt (MTS) was purchased from Promega Corporation (Madison, WI, USA). Human Immunodeficiency Virus type 1 recombinant envelope glycoprotein (HIV-1 rgp120) were obtained from NIH AIDS Reagent Program (Germantown, MD, USA).

5.3.2 Experimental section:

Synthetic scheme of PBA closomer nanoscaffold

Figure 5-2 shows the overall synthetic scheme. The reaction is comoposed of two steps, namely hydroxylation and etherfication respectively.

Cage hydroxylation

PBA closomer was synthesized following the method of Hawthorne et al[32]. Briefly, $Cs_2[closo-B_{12}OH_{12}]$ was synthesized by dissolving 2g of $Cs_2[closo-B_{12}H_{12}]$ in 15 ml of H_2O_2 and the mixture was left to reflux at 110 ºC. ^{11}B NMR and IR spectroscopy assessed reaction progress. Two (2) ml of H_2O_2 was added to the reaction mixture every 3 days until reaction completion which is indicated by the complete disappearance of $Cs_2[closo-B_{12}H_{12}]$ singlet at -17.7 ppm and the appearance of a new singlet around -20.3 ppm, characteristic of $Cs_2[closo-B_{12}OH_{12}]$ (Figure 5-3)

$Cs_2[closo-B_{12}OH_{12}]$ is not soluble in organic solvents such as acetonitrile and dichloromethane due to Cs+ counter ion . Therefore, to enhance the solubility of the closomer in organic solvents, Cs was replaced with more hydrophobic counter ions such as TBA (tetra-n-butylammonium). Cationic exchange chromatography was used to convert $Cs_2[closo-B_{12}OH_{12}]$ to $TBA_2[closo-B_{12}OH_{12}]$.(Figure 5-4) shows the cationic exchange chromatography setup.

Cage etherification

As shown in (Figure 5-5), the ether linked closomer was synthesized by following the method of Hawthorne et al[32]. PBA closomer was synthesized by dissolving 0.5g of $TBA_2[closo-B_{12}OH_{12}]$ in 25ml of acetonitrile. 2 ml of N,N-diisopropylethylamine and bromo phenylboronic acid were added. The mixture was left to reflux at 150 ºC for 7 days. Reaction progress was evaluated by ^{11}B NMR and FTIR spectroscopy.

5.4 Structure Characterization

^{11}B NMR spectroscopy was carried out on a Varian 400 MHz spectrometer (Palo Alto, CA, USA) with a Varian 2-channel probe. VnmrJ software (version 4.2A) was used for data acquisition and processing. Wilmad® quartz NMR tubes (600 MHz, diam. 5 mm, L7 in, Sigma-Aldrich, St. Louis, MO, USA) were used for spectral acquisition in order to eliminate the contribution of borosilicate glass in the spectrum. An inversion recovery experiment was performed to optimize the relaxation delay (T1), which was found to be 0.4s. Shimming was applied to each sample to maintain the same linewidth in each spectrum. The number of scans and the pulse width were 512 and 90° (11µs), respectively. The spinning frequency was 20 Hz. $BF_3.OEt_2$ (15% in $CDCl_3$) was used as a ^{11}B q-NMR external standard and its chemical shift ($\delta \sim 0$ ppm). Typically, 650 µL of a sample are placed in the quartz NMR tubes. Baseline correction and phase adjustment were carried out manually using MestReNova Lite (11.02.2, Escondido, CA, USA).

IR spectra were acquired by the Nicolet IS10 FTIR instrument (Thermo Fisher Scientific, Madison, WI, USA) equipped with a Zinc selenide (Z_nS_e) crystal. The instrument was used in the Attenuated Total Reflectance (ATR) mode. A resolution of 4 cm^{-1} and a sample scan of 228 were fixed as basic acquisition parameters. Transmittance IR spectra were acquired between 4000 and 650 cm^{-1}. For better spectral resolution, all samples were allowed to make intimate contact with the ATR Z_nS_e crystal's surface by pressing them with a built-in pressure clamp. FTIR spectra were collected and analyzed with OMNIC Specta Software (Thermo Fisher Scientific, Madison, WI, USA). Typically, the average IR spectrum acquisition time was 6 minutes.

5.5 Results and discussion

To characterize the PBA closomer, ^{11}B NMR spectroscopy as well as FT-IR were utilized. (Figure 5-6) shows ^{11}B NMR spectra of the reaction progression. The singlet peak at -17.7 ppm in day zero spectrum corresponds to the starting material $Cs_2[closo - B_{12}H_{12}]$. As the reaction progressed, the peak of the starting material began to decrease on day two, seven, and ten. Simultaneously, a new peak at -20.3 started to appear which is the product $Cs_2[closo - B_{12}OH_{12}]$. By the end of this reaction, the peak at -17.7 completely disappeared and only a singlet peak at -20.3 ppm was present on day fifteen(Figure 5-6).

Moreover, the reaction was monitored by FT-IR as it confirmed the completion of the reaction as well. The absorption spectra are shown in (Figure 5-7) for the reaction progression. The FTIR spectra collected for the reaction on day one, ten, and fifteen respectively. The appearance and growth of a band at 3250 cm^{-1} was assigned to the OH stretch in B-OH which is a formation of a product $Cs_2[closo - B_{12}OH_{12}]$. On the other hand, the band around 2550 cm^{-1} was attributed to the B-H stretch in $Cs_2[closo - B_{12}H_{12}]$ and it decreased gradually during the reaction until it totally disappeared on day fifteen's spectrum.

Figure 5-8 shows ^{11}B NMR spectra of the cationic exchange chromatography process. The ^{11}B NMR spectrum of $Cs_2[closo - B_{12}H_{12}]$, $Cs_2[closo - B_{12}OH_{12}], and\ TBA_2[closo - B_{12}H_{12}]$were compared to approve the conversion of Cs with TBA. The starting material appears at -17.4 ppm while the product appears at – 20 ppm. When the Cs was replaced, the peak shifted downfield to -18.2 ppm.

The last step, etherification, was also monitored by ^{11}B NMR spectra and FTIR. (Figure 5-9& 10) display the ^{11}B NMR and FTIR spectra of the reactants and product Br-PBA, $TBA_2[closo - B_{12}OH_{12}]$, PBA closomer respectively. The NMR spectroscopy results proved the successful formation of the desired material. Moreover, FTIR results confirmed the formation of the final product. According to the FTIR spectra in (Figure 5-10), which is a comparison between the reactants and the product. The OH stretch band at 3250 cm^{-1} was assigned to B-OH. By forming the final product, a stretching band around 3000 cm^{-1} was observed which corresponds to =C-H while a stretch around 1650 cm^{-1} corresponds to C=C. For C-O formation, bending and stretching vibrations were observed at 1000 and 1300 cm^{-1} respectively. Additionally, a B-O stretch was found to be around 1400 cm^{-1}.

5.6 Mechanism of cage hydroxylation reaction

By looking at the reaction progression of the cage hydroxylation ^{11}B NMR spectra (Figure 5-6), we believe that the reaction proceeded by a sequential mechanism and are seeking to confirm that. Therefore, some theoretical calculations as well as time analysis study using ^{11}B NMR spectroscopy have been done and qualitatively discussed.

5.6.1 Experimental data

In order to obtain as much of the data points and be able to study the real time $Cs_2B_{12}H_{12}$ hydroxylation mechanism, the reaction was performed in quartz NMR tube and kept in the magnet over long periods of time at 100 °C. NMR spectra were acquired every five minutes to monitor the reaction progression.

5.6.2 Theoretical calculation

Density functional theory (DFT) was utilized to simulate ^{11}B NMR spectra of different models. B3LYP/6.31G(d,p) was used as a basis set of all calculations. Gaussian 03 was used to create the input files. All calculations were done using supercomputer Lewis cluster at MU.

5.6.3 Comparison of experimental and theoretical results

Allegedly, there are 12 different simulations but according to the script results shown below, it is more complicated than that. In an icosahedron structure, there are one, two, and three bond distance lengths that are possible to have as shown in (Figure 5-11). The first column represents the total number of configurations. The rest of the columns represent the number of different unique possibilities to have a replacement in zero, single, double and triple length bond distances respectively. For instance, if one hydrogen in the cage is replaced by hydroxyl group nOH=1, there are twelve positions that are possible for the replacement. All these positions are chemically equivalent, thus there will be twelve total number of configurations. When another hydroxyl group is attached to the cage nOH=2, there are different possibilities where it can be. One option could be that the hydroxyl group can be the first nearest neighbor. Another option would be that the hydroxyl group will be the second nearest neighbor, while the last option would be that the hydroxyl group will be the third nearest neighbor (Figure5-12). All these options lead to 66 total number of configurations.

When three hydroxyl groups are attached to the cage nOH=3, multiple options would exist. There are 220 unique configurations. As shown in (Figure 5-13), each OH can be in each row (A), and there will be 60 versions of these configurations or 2 OHs can be in the first row and another one in second row (B) and there will be 60 versions and another 60 for the reverse situation(D). There will be 20 versions of having all OHs in first row(C) and another 20 when having OHs in the second row (E). Each row should be NMR equivalent. As the nOH increases, the unique configurations increase and reach 924 configurations when nOH=6.

Therefore, it is important to clarify that the simulated data shown was not intended to be a one to one comparison because not all possible configurations were included in the presented data. There are 5020 configurations of possible intermediates with 1-11 OH substitutions. Hence, this study has approximately one or two models per type of configuration in order to qualitatively understand the reaction mechanism. Given the complexity of all these configurations, it would be unreasonable to accomplish all these calculations.

We hypothesized that the actual mechanism of replacing an H with an O-H is done sequentially. Therefore, the experimental results will be presented and supported by theoretical results. The results presented in (Figure 5-14) are the raw data of experimental NMR spectra while the results presented in (Figure 5-15) demonstrate the NMR spectra obtained from theoretical calculation. As shown in these figures, the experimental and theoretical results appear to follow the same trend in the reaction mechanism. Both results started out with the same spectra for the starting materials, where only a single peak was observed. Then, both results trend in the same direction. In the experimental results, some peaks in the downfield region were going up and then down in the first few spectra, and that was relatively consistent with what was observed in the theoretical result. Likewise, the ending point in both the experimental and theoretical results were comparable.

```
nOH = 1, total number of configurations = 12
NMR equivalent configuration’s =
  12    1    0    0    0

nOH = 2, total number of configurations = 66
NMR equivalent configuration’s =
  30    2    1    0    0
  30    2    0    1    0
   6    2    0    0    1

nOH = 3, total number of configurations = 220
NMR equivalent configuration’s =

  60    3    1    1    1
  60    3    2    1    0
  20    3    3    0    0
  60    3    1    2    0
  20    3    0    3    0

nOH = 4, total number of configurations = 495
NMR equivalent configuration’s =

   15    4    2    2    2
  120    4    3    2    1
  120    4    2    3    1
   60    4    4    2    0
   60    4    3    3    0
   30    4    5    1    0
   60    4    2    4    0
   30    4    1    5    0

nOH = 5, total number of configurations = 792
NMR equivalent configuration’s =

  120     5    4    4    2
   60     5    6    3    1
  180     5    4    5    1
  180     5    5    4    1
   60     5    3    6    1
   60     5    7    3    0
   72     5    5    5    0
   60     5    3    7    0

nOH = 6, total number of configurations = 924
NMR equivalent configuration’s =
```

180	6	7	6	2
180	6	6	7	2
20	6	6	6	3
60	6	9	5	1
120	6	8	6	1
120	6	6	8	1
120	6	7	7	1
60	6	5	9	1
12	6	10	5	0
20	6	9	6	0
20	6	6	9	0
12	6	5	10	0

nOH = 7, total number of configurations = 792
NMR equivalent configuration’s =

120	7	9	9	3
180	7	10	9	2
60	7	8	11	2
180	7	9	10	2
60	7	11	8	2
60	7	12	8	1
72	7	10	10	1
60	7	8	12	1

nOH = 8, total number of configurations = 495
NMR equivalent configuration’s =

15	8	12	12	4
120	8	13	12	3
120	8	12	13	3
60	8	13	13	2
60	8	14	12	2
60	8	12	14	2
30	8	15	11	2
30	8	11	15	2

nOH = 9, total number of configurations = 220
NMR equivalent configuration’s =

60	9	16	16	4
60	9	16	17	3
20	9	18	15	3
60	9	17	16	3
20	9	15	18	3

nOH = 10, total number of configurations = 66
NMR equivalent configuration’s =

```
  30   10   20   21    4
  30   10   21   20    4
   6   10   20   20    5
```

nOH = 11, total number of configurations = 12
NMR equivalent configuration’s =

```
  12   11   25   25    5
```

nOH = 12, total number of configurations = 1
NMR equivalent configuration’s =

```
   1   12   30   30    6
```

5.7 Conclusion and future work

In conclusion, the PBA-closomer was successfully synthesized and the results were analyzed and confirmed using ^{11}B NMR and FT-IR spectroscopy. Future research by our collaborators in the School of Pharmacy will perform biological testing including: basic HIV gp-120 and PBA-closomer binding interaction, basic cytotoxicity testing, and CD4/gp120 binding prevention experiment.

Moreover, since two HIV drugs have been studied, a dual drug will be formed, which will be a combination of PBA-closomer and maraviroc, and the drug release will be studied using ^{11}B and ^{19}F NMR spectroscopy.

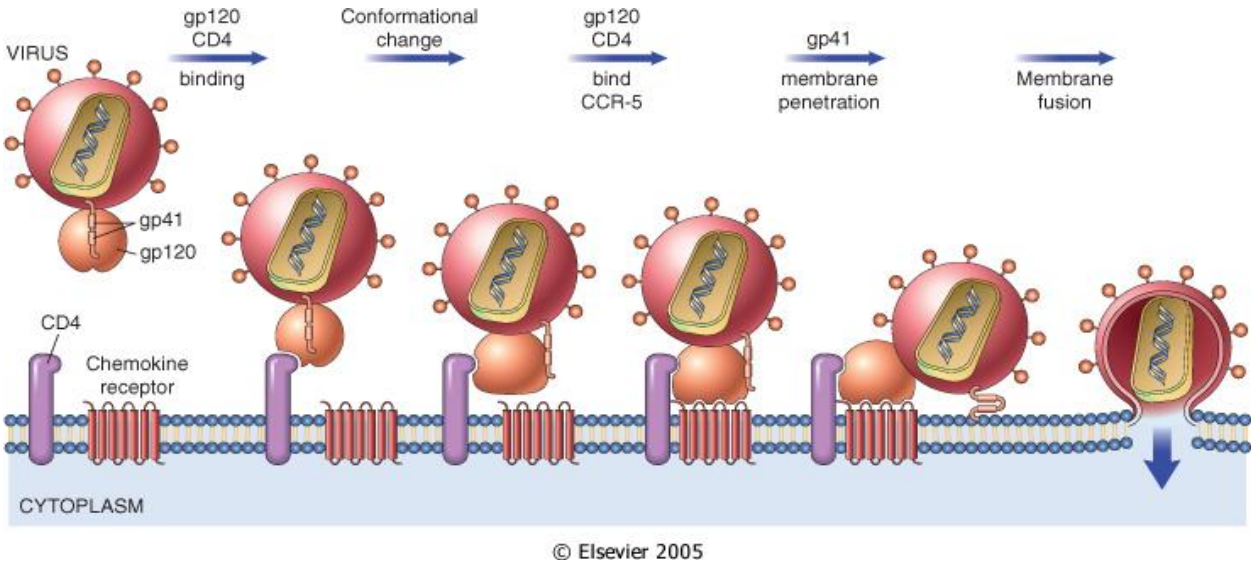

Figure 5-1. Mechanism of HIV entry

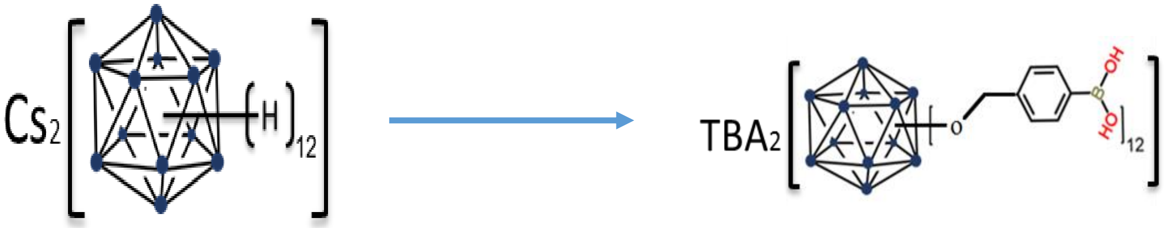

Figure 5-2. The overall synthetic scheme

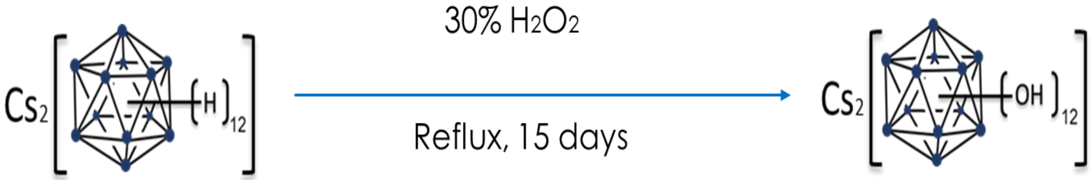

Figure 5-3. Cage hydroxylation

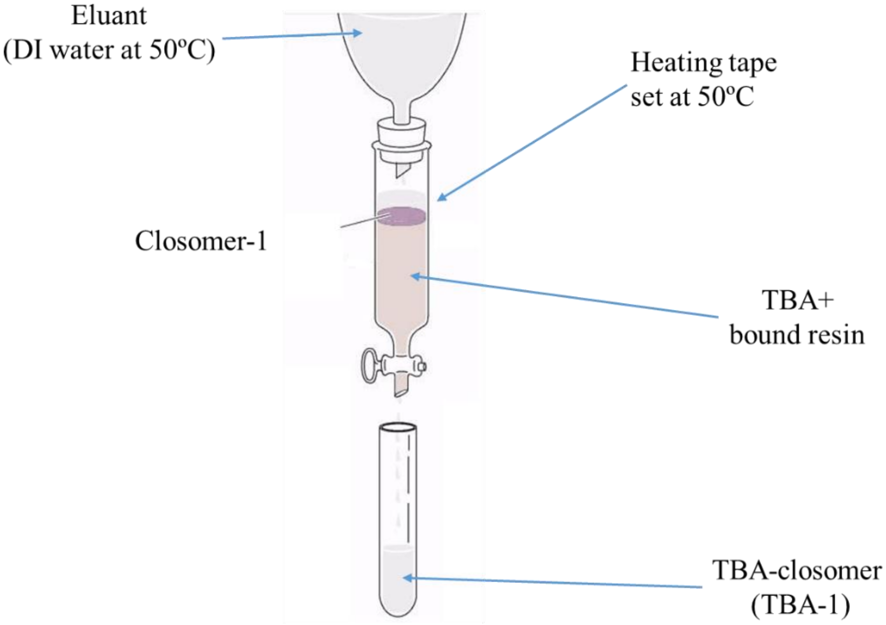

Figure 5-4. The cationic exchange chromatography

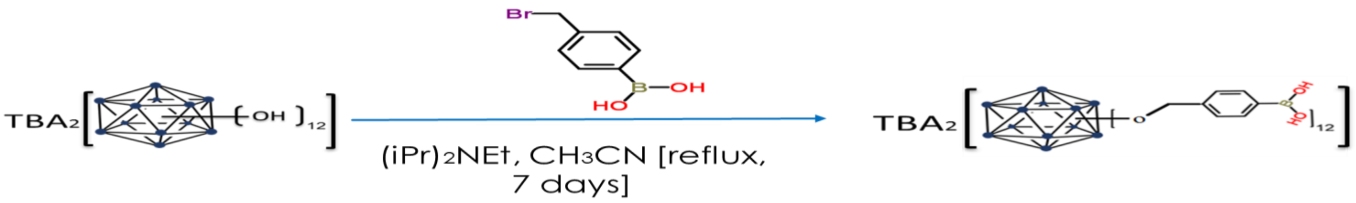

Figure 5-5. Cage etherification

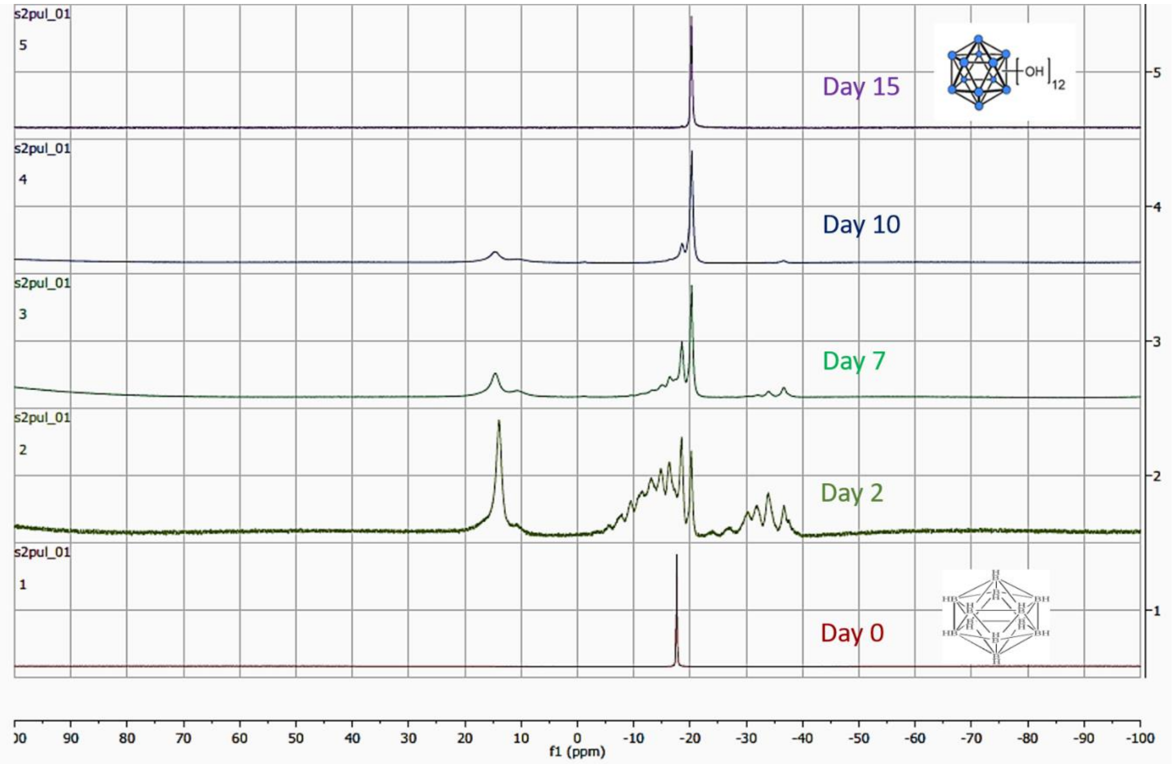

Figure 5-6. ^{11}B NMR spectra of day 0: starting material, day 2,7and 10: (intermediate) reaction progression, and day15: the product.

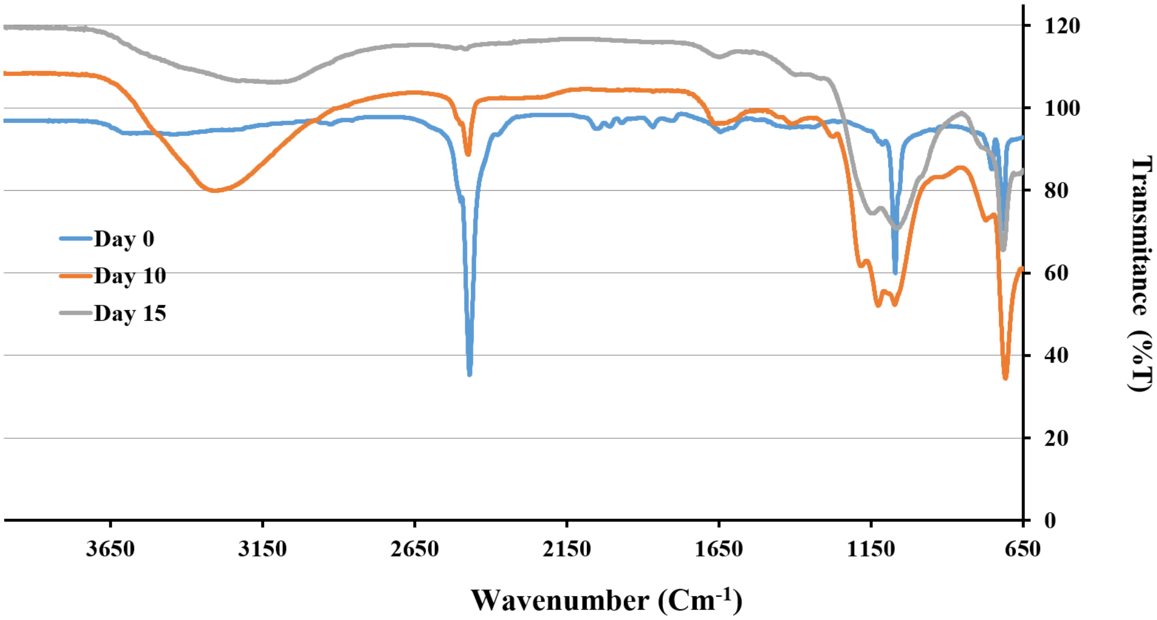

Figure 5-7. FT-IR spectra for the reaction progression

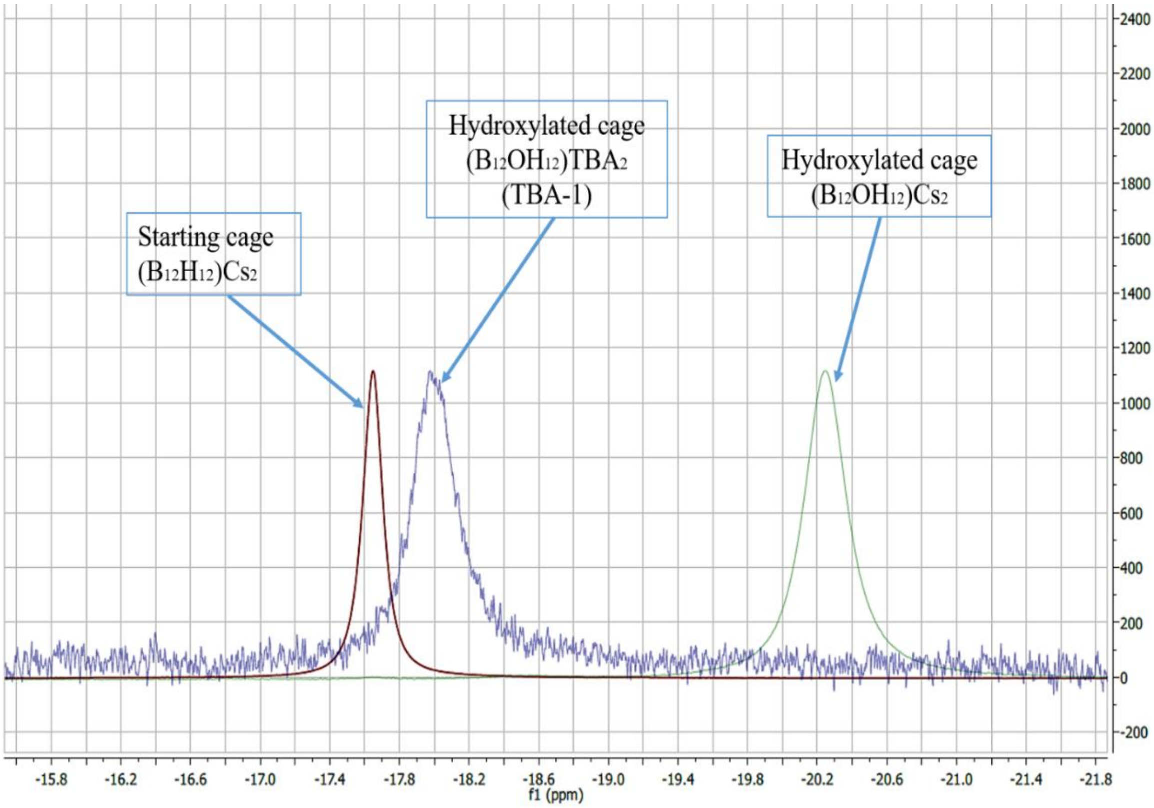

Figure 5-8 . ^{11}B NMR spectra of the stating materials and the product of the cationic exchange chromatography process

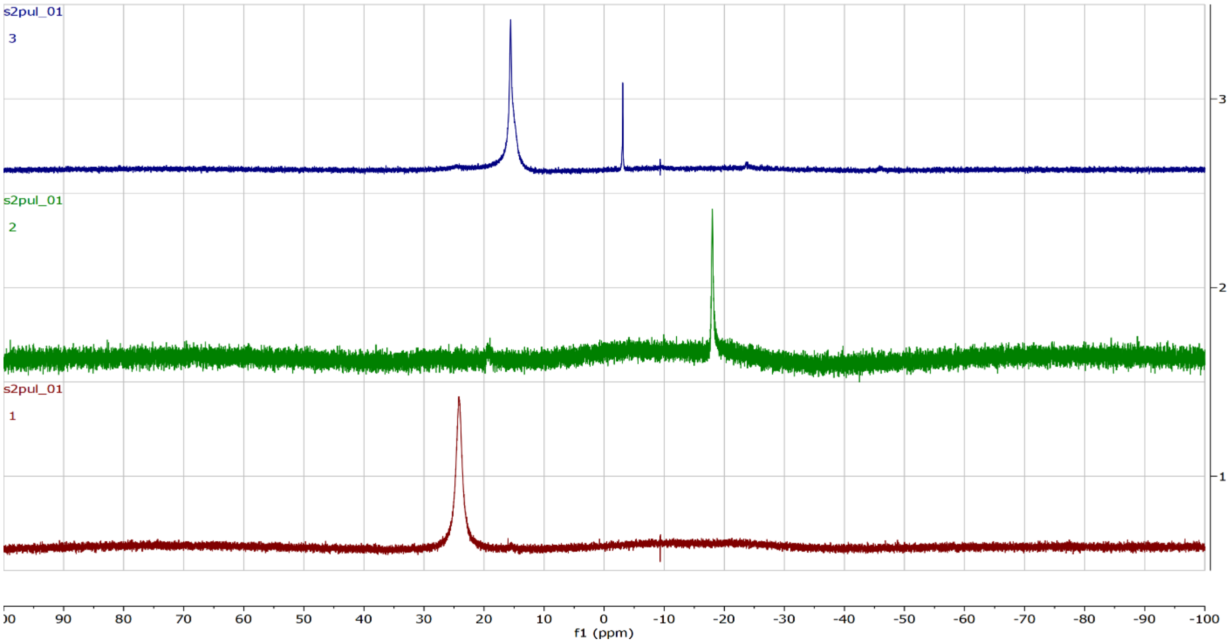

Figure 5-9. ^{11}B NMR spectra confirming the step two etherification. 1: Br-PBA, 2: TBA_2 $B_{12}OH_{12}$, 3: PBA-closomer.

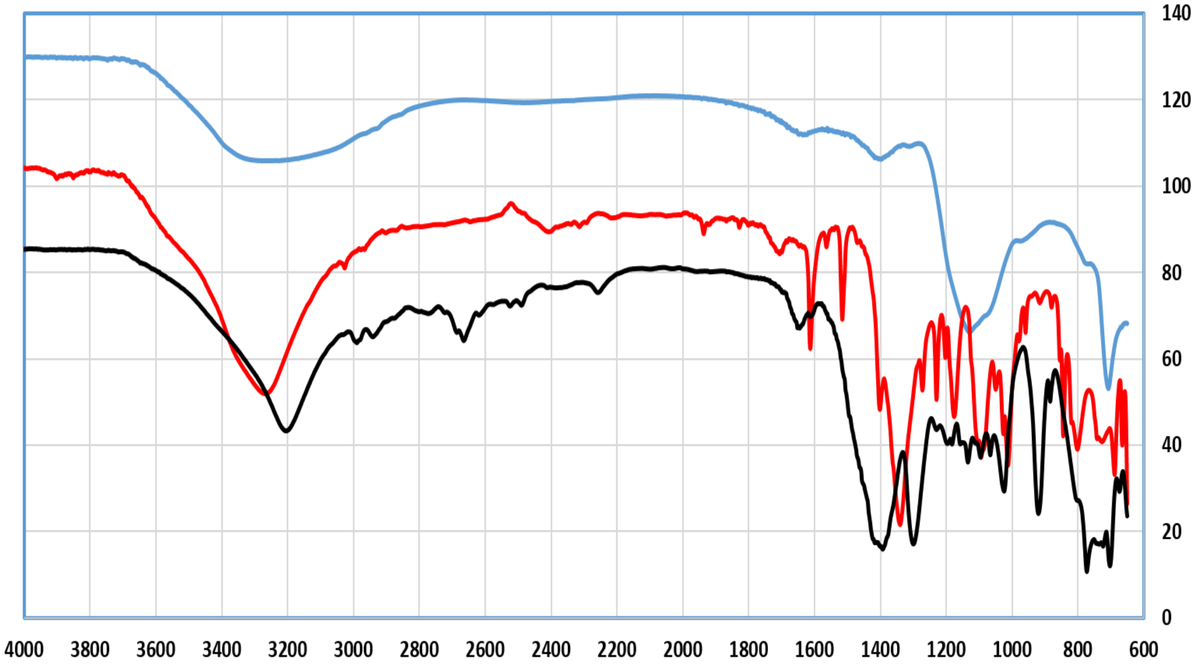

Figure 5-10. FTIR for black: PBA-closomer, red: Br-PBA and blue: $TBA_2[closo - B_{12}OH_{12}]$,

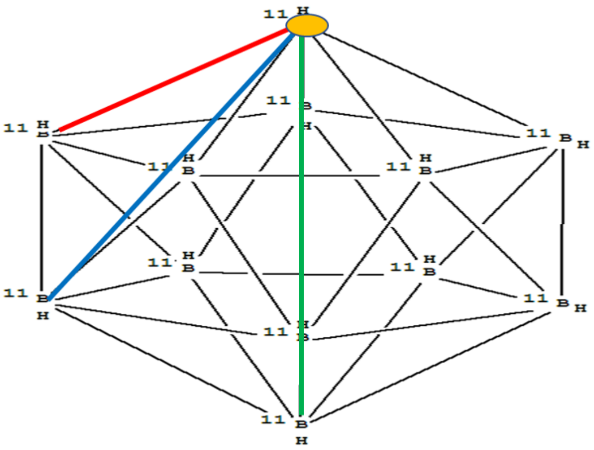

Figure 5-11. Different internuclear in an icosahedron 0 (yellow), 1(red), 2(blue), and 3(green) bond distances apart.

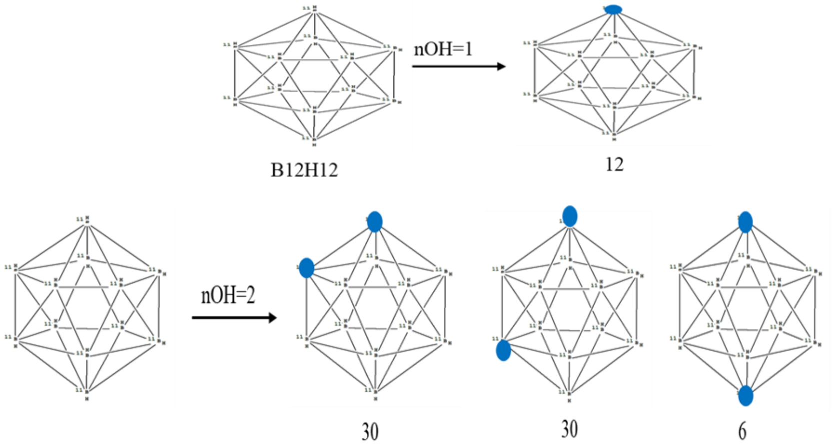

Figure 5-12. Some different possible configurations when nOH=1 and 2

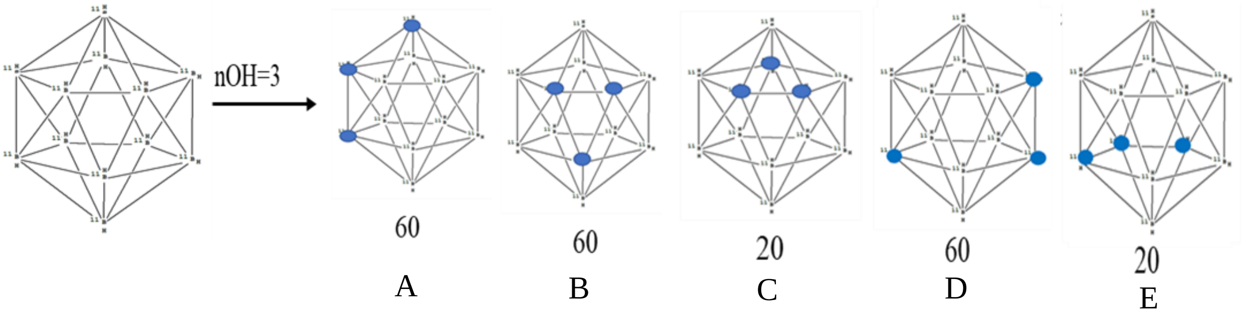

Figure 5-14. Some different possible configurations when nOH=3

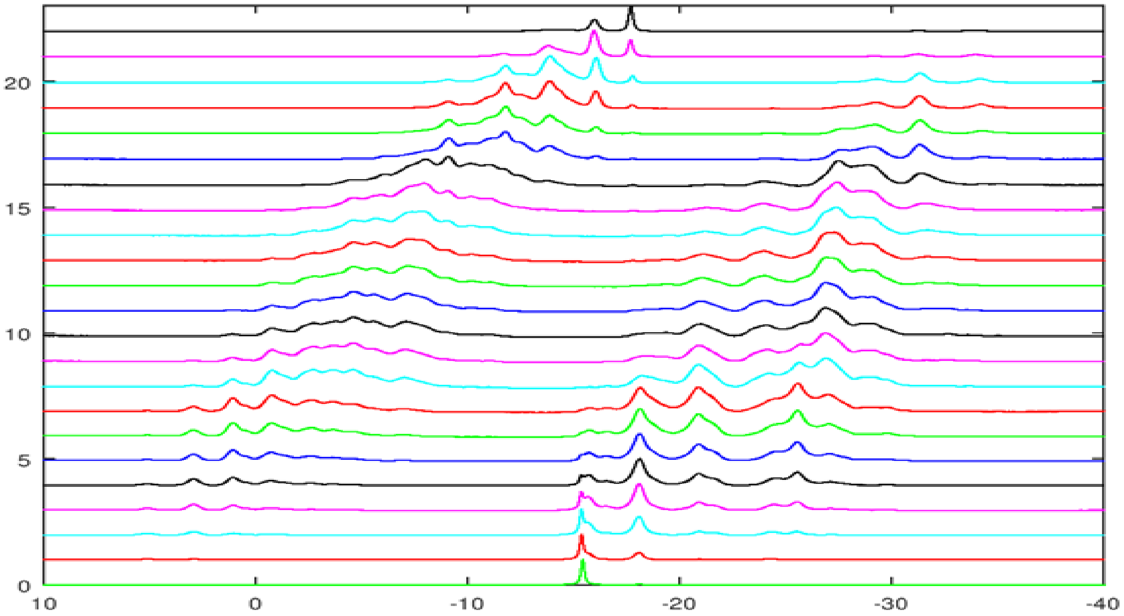

Figure 5-13. Experimental result of ^{11}B NMR spectra over time

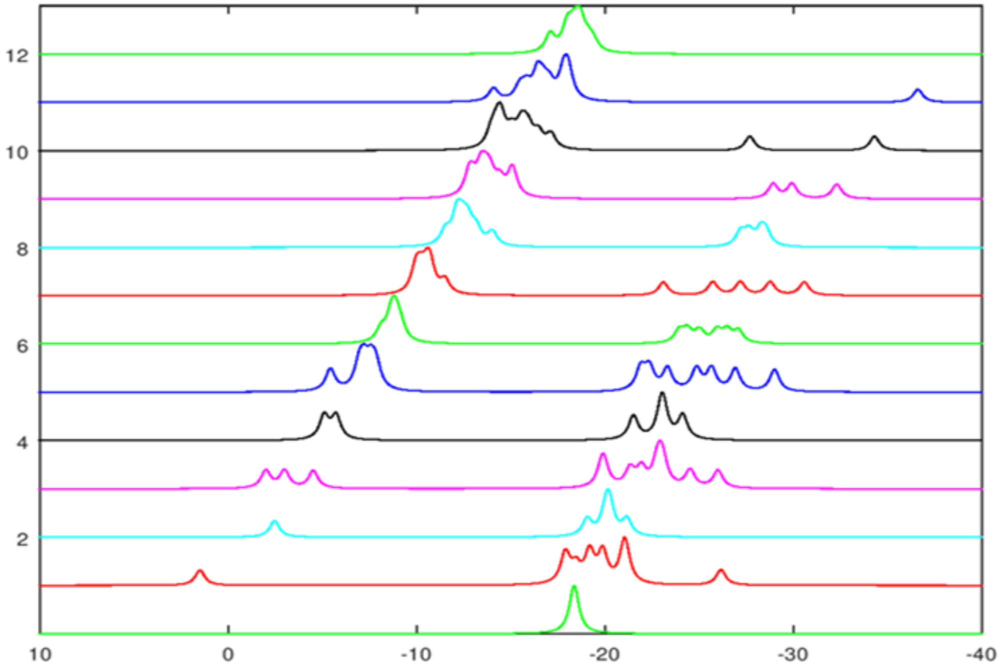

Figure 5-15. Simulated ^{11}B NMR for cage-nOH structures

References

(1) Center for Substance Abuse Treatment. Substance Abuse Treatment for Persons with HIV/AIDS. Rockville (MD): Substance Abuse and Mental Health Services Administration (US); 2000. (Treatment Improvement Protocol (TIP) Series, No. 37.) Chapter 1--Introductio.

(2) Gao, F.; Bailes, E.; Robertson, D. L.; Chen, Y.; Rodenburg, C. M.; SF, M.; Cummins, L. B.; Arthur, L. O.; Peeters, M.; Shaw, G. M.; et al. Origin of HIV-1 in the Chimpanzee Pan Troglodytes. *Nature* **1999**, *397* (6718), 436–441. https://doi.org/10.1038/17130.

(3) Zhu, T.; Korber, B. T.; Nahmias, A. J.; Hooper, E.; Sharp, P. M.; Ho, D. D. An African HIV-1 Sequence from 1959 and Implications for the Origin of the Epidemic. *Nature* **1998**, *391* (February), 594–597.

(4) Simon, F.; Mauclère, P.; Roques, P.; Loussert-Ajaka, I.; Müller-Trutwin, M. C.; Saragosti, S.; Georges-Courbot, M. C.; Barré-Sinoussi, F.; Brun-Vézinet, F. Identification of a New Human Immunodeficiency Virus Type 1 Distinct from Group M and Group O. *Nat. Med.* **1998**, *4* (9), 1032–1037. https://doi.org/10.1038/2017.

(5) Wilen, C. B.; Tilton, J. C.; Doms, R. W.; Walker, B.; Mcmichael, A.; Wilen, C. B.; Tilton, J. C.; Doms, R. W.; Craigie, R.; Bushman, F. D.; et al. HIV : Cell Binding and Entry. *Cold Spring Harb. Perspect. Med.* **2012**, *2* (8), 1–14. https://doi.org/10.1101/cshperspect.a006866.

(6) Mizuochi, T.; Spellman, M. W.; Larkin, M.; Solomon, J.; Basa, L. J.; Feizi, T. Carbohydrate Structures of the Human-Immunodeficiency-Virus (HIV) Recombinant Envelope

Glycoprotein Gp120 Produced in Chinese-Hamster Ovary Cells. *Biochem. J.* **1988**, *254* (2), 599–603. https://doi.org/10.1042/bj2540599.

(7) Hansen, J. E. Carbohydrates of Human Immunodeficiency Virus. *APMIS. Suppl.* **1992**, *27* (24), 96–108.

(8) Mizuochi, T.; Matthewsv, T. J.; Solomon, J. Diversity of Oligosaccharide Structures on the Envelope Glycoprotein Gp120 of Human Immunodeficiency Virus 1 from the Lymphoblastoid Cell Line H9. *J. Biol. Chem.* **1990**, *265* (15).

(9) Bonomelli, C.; Doores, K. J.; Dunlop, D. C.; Thaney, V.; Dwek, R. A.; Burton, D. R.; Crispin, M.; Scanlan, C. N. The Glycan Shield of HIV Is Predominantly Oligomannose Independently of Production System or Viral Clade. *PLoS One* **2011**, *6* (8), 1–7. https://doi.org/10.1371/journal.pone.0023521.

(10) Raska, M.; Novak, J. Involvement of Envelope-Glycoprotein Glycans in HIV-1 Biology and Infection. *Arch. Immunol. Ther. Exp. (Warsz).* **2010**, *58* (3), 191–208. https://doi.org/10.1007/s00005-010-0072-3.

(11) Huang, X.; Jin, W.; Hu, K.; Luo, S.; Du, T.; Griffin, G. E.; Shattock, R. J.; Hu, Q. Highly Conserved HIV-1 Gp120 Glycans Proximal to CD4-Binding Region Affect Viral Infectivity and Neutralizing Antibody Induction. *Virology* **2012**, *423* (1), 97–106. https://doi.org/10.1016/j.virol.2011.11.023.

(12) Balzarini, J. Targeting the Glycans of Gp120: A Novel Approach Aimed at the Achilles Heel of HIV. *Lancet Infect. Dis.* **2005**, *5* (11), 726–731. https://doi.org/10.1016/S1473-3099(05)70271-1.

(13) Akkouh, O.; Ng, T. B.; Singh, S. S.; Yin, C.; Dan, X.; Chan, Y. S.; Pan, W.; Cheung, R. C. F. Lectins with Anti-HIV Activity: A Review. *Molecules* **2015**, *20* (1), 648–668. https://doi.org/10.3390/molecules20010648.

(14) Swanson, M. D.; Winter, H. C.; Goldstein, I. J.; Markovitz, D. M. A Lectin Isolated from Bananas Is a Potent Inhibitor of HIV Replication. *J. Biol. Chem.* **2010**, *285* (12), 8646–8655. https://doi.org/10.1074/jbc.M109.034926.

(15) Akashi, M.; Niikawa, T.; Serizawa, T.; Hayakawa, T.; Baba, M. Capture of HIV-1 Gp120 and Virions by Lectin-Immobilized Polystyrene Nanospheres †. *Bioconjug. Chem.* **1998**, *9* (1), 50–53. https://doi.org/10.1021/bc970045y.

(16) Hayakawa, T.; Kawamura, M.; Okamoto, M.; Baba, M.; Niikawa, T.; Takehara, S.; Serizawa, T.; Akashi, M. Concanavalin A-Immobilized Polystyrene Nanospheres Capture HIV-1 Virions and Gp120: Potential Approach towards Prevention of Viral Transmission. *J. Med. Virol.* **1998**, *56* (4), 327–331. https://doi.org/10.1002/(SICI)1096-9071(199812)56:4<327::AID-JMV7>3.0.CO;2-A.

(17) Mahalingam, A.; Geonnotti, A. R.; Balzarini, J.; Kiser, P. F. Activity and Safety of Synthetic Lectins Based on Benzoboroxole- Functionalized Polymers for Inhibition of HIV Entry. *Mol. Pharm.* **2011**, *8* (6), 2465–2475. https://doi.org/10.1021/mp2002957.

(18) Brooks, W. L. A.; Sumerlin, B. S. Synthesis and Applications of Boronic Acid-Containing Polymers: From Materials to Medicine. *Chem. Rev.* **2016**, *116* (3), 1375–1397. https://doi.org/10.1021/acs.chemrev.5b00300.

(19) Trippier, P. C.; Mcguigan, C.; Balzarini, J. Original Article Phenylboronic-Acid-Based Carbohydrate Binders as Antiviral Therapeutics : Monophenylboronic Acids. **2010**, *257*,

249–257. https://doi.org/10.3851/IMP1632.

(20) Trippier, P. C.; Balzarini, J.; McGuigan, C. Phenylboronic-Acid-Based Carbohydrate Binders as Antiviral Therapeutics: Bisphenylboronic Acids. *Antivir. Chem. Chemother.* **2011**, *21* (3), 129–142. https://doi.org/10.3851/IMP1707.

(21) Jalisatgi, S. S.; Kulkarni, V. S.; Tang, B.; Houston, Z. H.; Lee, M. W.; Hawthorne, M. F. A Convenient Route to Diversely Substituted Icosahedral Closomer Nanoscaffolds. *J. Am. Chem. Soc.* **2011**, *133* (32), 12382–12385. https://doi.org/10.1021/ja204488p.

(22) Ma, L.; Hamdi, J.; Wong, F.; Hawthorne, M. F. Closomers of High Boron Content: Synthesis, Characterization, and Potential Application as Unimolecular Nanoparticle Delivery Vehicles for Boron Neutron Capture Therapy. *Inorg. Chem.* **2006**, *45* (1), 278–285. https://doi.org/10.1021/ic051214q.

(23) Goswami, L. N.; Houston, Z. H.; Sarma, S. J.; Li, H.; Jalisatgi, S. S.; Hawthorne, M. F. Synthesis of Vertex-Differentiated Icosahedral Closo -Boranes: Polyfunctional Scaffolds for Targeted Drug Delivery. *J. Org. Chem.* **2012**, *77* (24), 11333–11338. https://doi.org/10.1021/jo3021314.

(24) Johnson, V. A. Combination Therapy: More Effective Control of HIV Type 1? *AIDS Res Hum Retroviruses* **1994**, *10* (8), 907–912.

(25) Schmitt, B.; Bernhardt, T.; Moeller, H. J.; Heuser, I. Combination Therapy in Alzheimer's Disease: A Review of Current Evidence. *CNS Drugs* **2004**, *18* (13), 827–844.

(26) Mokhtari, R. B.; Homayouni, T. S.; Baluch, N.; Morgatskaya, E.; Kumar, S.; Das, B.; Yeger, H. Combination Therapy in Combating Cancer. *Oncotarget* **2015**, *8* (23), 38022–

38043. https://doi.org/10.18632/oncotarget.16723.

(27) Bondarev, O.; Khan, A. A.; Tu, X.; Sevryugina, Y. V.; Jalisatgi, S. S.; Hawthorne, M. F. Synthesis of [Closo-B12(OH)11NH3] -: A New Heterobifunctional Dodecaborane Scaffold for Drug Delivery Applications. *J. Am. Chem. Soc.* **2013**, *135* (35), 13204–13211. https://doi.org/10.1021/ja4069613.

(28) Chen, F.; Ehlerding, E. B.; Cai, W. Theranostic Nanoparticles. *J. Nucl. Med.* **2014**, *55* (12), 1919–1922. https://doi.org/10.2967/jnumed.114.146019.

(29) Heber, E. M.; Kueffer, P. J.; Lee, M. W.; Hawthorne, M. F.; Garabalino, M. A.; Molinari, A. J.; Nigg, D. W.; Bauer, W.; Hughes, A. M.; Pozzi, E. C. C.; et al. Boron Delivery with Liposomes for Boron Neutron Capture Therapy (BNCT): Biodistribution Studies in an Experimental Model of Oral Cancer Demonstrating Therapeutic Potential. *Radiat. Environ. Biophys.* **2012**, *51* (2), 195–204. https://doi.org/10.1007/s00411-011-0399-0.

(30) Solange C. Garcia, S. S. G., Guilherme B. Bubols, Rachel P. Bulcão, Mariele F. Charão, A. R. P. In Vivo Toxicological Evaluation, Cardiotoxicity, and Hepatotoxicity. *Nanotoxicology* **2013**, *299–324*.

(31) Huang, R.; Carney, R. P.; Ikuma, K.; Stellacci, F.; Lau, B. L. T. Effects of Surface Compositional and Structural Heterogeneity on Nanoparticle–Protein Interactions: Different Protein Configurations. *ACS Nano* **2014**, *8* (6), 5402–5412. https://doi.org/10.1021/nn501203k.

(32) Farha, O. K.; Julius, R. L.; Lee, M. W.; Huertas, R. E.; Knobler, C. B.; Hawthorne, M. F. Synthesis of Stable Dodecaalkoxy Derivatives of Hypercloso-B 12H12. *J. Am. Chem. Soc.* **2005**, *127* (51), 18243–18251. https://doi.org/10.1021/ja0556373.

Part II. APPLICATIONS OF SOLID-STATE NMR SPECTROSCOPY

Overview

Solid-state NMR has proven to be an applicable technique for spectroscopic studies by expanding its uses in many fields such as chemistry, physics, biology, and geology. In part II of this dissertation, some applications of solid-state NMR spectroscopy will be presented and discussed in diverse research projects.

In chapter 7, the local physical structure of different boron carbide thin films were examined via solid-state NMR spectroscopy. A number of SSNMR experiments and results were discussed.

In chapter 8, SSNMR spectroscopy technique was utilized to study TiO_2, and improve its optical properties.

Objectives

The overall objectives of this part of the dissertation are:

1. Apply SSNMR spectroscopy techniques to study the internal structure of boron carbide thin films grown by plasma enhanced chemical vapor deposition (PECVD)
2. Monitor the progress of TiO_2 reaction, and study green and white TiO_2 using SSNMR spectroscopy.

Chapter 6 . SSNMR SPECTROSCOPY CONCEPTS AND EXPERIMENTS

6.1 The concept of magic-angle spinning (MAS)

Typically, a SSNMR spectrum is broader and has a lower resolution compared to the solution NMR spectrum. There are three important contributions that make the SSNMR spectrum somewhat featureless. First is the dipolar broadening which is the dipolar interaction between two spins. This interaction can be either a homonuclear or heteronuclear interactions. Equations 6-1&2 show the Hamiltonian of homonuclear and heteronuclear interactions respectively. The second reason is the chemical shift anisotropy (CSA), which arises from the asymmetry of electronic density around the nuclei and the Hamiltonian of CSA is given in Equation (6-3). The last contribution is the first-order quadrupolar interaction. Equation (6-4) shows the basic form of the quadrupole Hamiltonian, which describes the interaction between the nuclear electric quadrupole moment eQ and electric field gradient EFG.

The magnitudes of the second-order interaction of the dipolar and chemical shift anisotropy interaction are neglected compared to the Zeeman interaction. Nevertheless, the second-order quadrupolar interaction may have a sufficient magnitude that it cannot be neglected.

In the solution NMR spectroscopy, all these factors average to zero due to the rapid motion of the sample. However, in SSNMR this assumption is no longer accurate. Fortunately, we can average most of these factors to zero and acquire high-resolution spectra with narrow lines using a technique called magic angle spinning (MAS) since all of the factors are orientation dependent with a similar orientation dependence [$D(\theta) \alpha\ 3\cos^2(\theta)-1$] (Figure 6-1). This can be achieved through the mechanical rotation of the sample at 54.74° with respect to the magnetic field in addition to the rapid sample rotation. The dipolar interaction and first-order quadrupolar interactions will be restored individually by applying pulses to the spin state, which will change the product to a non-zero value as shown in (Figure 6-2).

$$H_{\mathrm{D}}^{II} = -\frac{\mu_0}{4\pi}\hbar\sum_{i}\sum_{j}\frac{\gamma^2}{r_{ij}^3}\frac{1}{2}(3\cos^2\theta_{ij}-1)(3I_z^iI_z^j-\mathbf{I}^i\cdot\mathbf{I}^j), \qquad (6\text{-}1)$$

$$H_{\mathrm{D}}^{IS} = -\frac{\mu_0}{4\pi}\hbar\sum_{i}\sum_{j}\frac{\gamma^I\gamma^S}{r_{ij}^3}\frac{1}{2}(3\cos^2\theta_{ij}-1)2I_z^iS_z^j, \qquad (6\text{-}2)$$

$$H_{\mathrm{CS}} = \left\{\sigma_{\mathrm{iso}}\gamma B_0+\frac{1}{2}\delta\left[3\cos^2\theta-1-\eta\sin^2\theta\cos(2\phi)\right]\right\}I_z. \qquad (6\text{-}3)$$

$$\hat{\mathrm{H}}_{\mathrm{Q}} = \frac{eQ}{2I(2I-1)\hbar}\hat{\mathrm{I}}.V.\hat{\mathrm{I}} \qquad (6\text{-}4)$$

Where: Q is the nuclear quadrupole moment

I is for spin I

$\hat{\mathrm{I}}$ is the nuclear spin vector

6.2 Magic-angle spinning setup

Since the discovery of magic angle spinning in SSNMR, the applications of this method have significantly increased in numerous fields such as chemistry, biology and pharmacy [1]. The sample should be packed in a rotor and placed in the angle 54.74° with respect to the applied magnetic field. Additionally, the magic angle spinning rate must be equal to or higher than the magnitude of the anisotropic interaction to average it to zero. Setting this angle on 54.74°

accurately is essential before doing 90 calibration or SSNMR experiments since it has a deleterious effect on different NMR parameters namely: 1) line-width, 2) line-position, and 3) signal to noise ratio S/N.

Different methods have been suggested to place the sample on the magic angle [2–4]. However, an accurate and simple way to accomplish this degree of angle is by using potassium bromide (KBr)[5]. ^{79}Br is utilized since the crystal structure of KBr is a cubic and bromine is a small 1st order quadrupole, but large enough to exhibit averaging by MAS. Additionally, the ^{79}Br resonance frequency is very close to that of ^{13}C, so little effort is needed to tune the probe back. Most new MAS SSNMR probes have an adjustable knob to manipulate the tuning mechanically. During this method, the ^{79}Br signal is going to be monitored to obtain the maximum number of rotational echoes with the largest amplitude.

6.3 Quadrupole nuclei in SSNMR spectroscopy

Typically, SSNMR studies apply to ^{1}H and ^{13}C nuclei, which have a spin I=1/2. However, by looking at the periodic table, 74% of active NMR isotopes are quadrupolar nuclei meaning that 100 of 130 magnetically active naturally occurring isotopes are quadrupolar nuclei (spine $I > ½$)(Figure 6-3)[6]. In SSNMR, quadrupole nuclei are in fact essential. On the other hand, they are quadrupolar nuclei, thus, there will be an electric quadrupolar interaction, which is responsible for broadening the SSNMR signal. Consequently, acquiring and interpreting the SSNMR spectra of these nuclei leads to some difficulties. However, studying them provides a lot of information, particularly in inorganic chemistry and materials applications. Therefore, the high demand of inorganic characterization for different materials led to a significant improvement in the quadrupolar nuclei SSNMR experimental techniques. In 1998, more than 400 references in SSNMR studies of quadrupolar nuclei demonstrated that the electric quadrupolar interaction problem can be overcome and invaluable information can be acquired from SSNMR spectroscopy[7].

6.4 Quadrupolar relaxation

This type of relaxation applies only for nuclei with a spin I >1/2, where the positive charge distribution has the shape of an oblate or prolate spheroid. Moreover, in these quadrupolar nuclei, the electric field gradient (EFG) exerts a torque, and molecular tumbling can initiate transitions among the spin states. Quadrupolar relaxation critically depends on a quadrupole moment (Q), which is 0 for spin=1/2 nuclei. When the quadrupole moment is small (such as ^{2}H and ^{6}Li with spin I=1), the nuclei behaves similarly to a nuclei with spin I=1/2. Hence, a sharp NMR peak will be observed. However, when the quadrupole moment is large, the nucleus will have a very short T1 Equation (6-5). Thus, the observation of NMR signals and spin-spin splitting to the nucleus will be hindered.

In some molecules with tetrahedral or octahedral symmetry, the electric field gradient is small or zero, which will allow T1 to be long enough to acquire an acceptable NMR spectra. When the quadrupole moment (Q) is large, it will show a very fast quadrupole relaxation whether there is a properly symmetric environment or not.

Quadrupole relaxation not only affects the nuclei itself, but it is also affects the neighboring active nuclei. This can happen because of a very rapid quadrupole relaxation resulting in broadening or completely removing the J-coupling between two nuclei. ^{11}B-X group is a very common example for this effect. In a boron NMR experiment, a T_2 effect on the X nucleus, which is the interchange of spin states, is the main reason of broadening the boron spectra. Hence, it will make observing the connection between boron directly bonded to carbon or proton almost unmanageable. Boron nuclei can be classified as a self-decoupled nuclei as it has a very fast quadrupole relaxation that will suppress all coupling with the nearby carbon or proton.

$$R_{QR} = \frac{1}{T_{1_{(QR)}}} = \frac{3}{10}\Pi^2 \frac{2I+3}{I^2(2I-1)}(1+\frac{\eta^2}{3})(\frac{e^2Qqz}{h})^2\tau_C \qquad (6\text{-}5)$$

Where:

η = the asymmetry of electric field

Q= quadrupole moment of nuclei

q= electric field gradient

I= nuclear spin

τ= molecular correlation time

6.5 Basic SSNMR experiments:

Prior to any SSNMR experiment, there are several parameters which have to be set up precisely in each channel in the NMR probe in order to get a spectrum with better resolution and a narrow line[8]. An initial parameter is shimming. The magnet has to be shimmed properly to make sure that the magnetic field around the sample is homogenous. This step should be performed infrequently unless a substantial change occurs to the probe.

In contrast to the shimming, the NMR probe has to be tuned more frequently to a desired frequency to maximize the power carried to the sample so an optimal signal to noise ratio can be achieved.

The RF pulse calibration is the most important parameter which has a critical effect on the collected NMR spectra. The purpose of the pulse calibration is to determine the pulse width required to produce to a 90 degree pulse. This experiment can be achieved by obtaining a series of NMR spectra while increasing the RF pulse widths incrementally. After Fourier transforming the spectra, the calibration curve, known as nutation curve, can be plotted which includes the NMR signals as a function of the RF pulse widths. As shown in (Figure 6-4), while increasing a pulse width, the height of the peak increases as a sin function. The first maximum represents the 90 degree pulse width while the first zero-crossing represents the 180 degree pulse width [9].

T1 measurement and estimation is equally as important as other NMR parameters. It provides the relaxation time, which is related to the repetition time of an experiment. The most common experiment to obtain T1 value is called an inversion recovery experiment. It measures the time it takes for the magnetization to convert back from $-I_z$ to $+I_z$. Figure 6-5 shows the pulse sequence as it has a 180^o inversion pulse, tau time (τ), and then a 90^o pulse. As shown in (Figure 6-5), the tau time (τ) increases gradually in each experiment, and the signal intensity can be plotted as a function of tau. The data could be fitted as a non-linear regression fit Equation (6-6) [10].

$$I_{(\tau)} = I_\infty(1-2\exp(-\tau/T_1)) \qquad (6\text{-}6)$$

Once all the SSNMR parameters are set up accurately, several SSNMR experiments can be performed to obtain fundamental information about different nuclei.

6.5.1 Direct excitation

The direct excitation experiment is a quantitative experiment, which has a quick and simple way to elucidate information about the chemical shift for any active nuclei in the sample. Typically, it is the first experiment performed since it can demonstrate the chemical identity. The pulse sequence of the direct excitation experiment with heteronuclear contentious wave ^{1}H decoupling is shown in (Figure 6-6)[11]. Generally, this experiment is applied for each nucleus in every single project.

6.5.2 Cross Polarization experiment

Cross polarization experiment (CP) can be classified as a starting point for deep and complex analysis in SSNMR spectroscopy. It has been applied successfully to define the structure of several molecules[11–15]. Commonly, the CP experiment is acquired with a combination of magic angle spinning (MAS) as well as heteronuclear dipolar decoupling. The magic angle spinning and the heteronuclear dipolar decoupling serve as tools to improve the resolution of the spectra while the cross polarization assists to increase the experiment sensitivity.

The principle behind this experiment is that the signal of low gamma nuclei will be enhanced by a transfer of polarization from a high gamma nucleus such as ^{1}H, to less abundant nuclei such as ^{13}C, via heteronuclear dipolar coupling. In order to transfer the polarization, the Hartmann-Hahn condition must be fulfilled Equation (6-7)

$$\gamma_I B_I = \gamma_S B_S \qquad (6\text{-}7)$$

Where: γ is the gyromagnetic ratio

B is the amplitude of radio frequency (r.f) applied to each nuclei

The magnetization transformation can be visualized in terms of energy levels as shown in (Figure 6-7). Once the Hartmann-Hahn condition is satisfied, the polarization equalizes between the nuclei leading to an enhanced polarization in the low gamma species (Figure 6-8)[16]. The pulse sequence of the CP experiment is shown in (Figure 6-9), where an application of the pulse to both nuclei occurs simultaneously. By obtaining CP spectra, we can have a hint about which nuclei are close enough to protons to see the transfer.

Lee-Goldburg (LG) cross polarization is another version of CP experiment. In LG-CP experiment, ^{1}H-^{1}H homonuclear dipolar interaction will be suppressed, and X-^{1}H pin-pair interaction in isolation will be permitted in order to get more precise information about the dipolar coupling strength. This can happen by irradiating the proton spin with a LG homonuclear decoupling pulse. Figure 6-10 shows the pulse sequence of the LG-CP experiment.

By quantifying the LG-CP oscillations and build-up curves, an estimation of dipolar coupling can be made which ultimately will lead to structural information. Additionally, the distances between ^{1}H and other nuclei can be elucidated, allowing a conception of whether the distance is short, medium, or long between these nuclei as shown in (Figure 6-11). This information about distances will be very helpful for building an image for the internal structure. For example, if the distance between the two nuclei is short, that means the X nucleus is directly bound to the proton and a fast oscillation will be detected in the build-up curve. When the distance is long, that indicates the X nucleus does not have a proton and the nearest proton is far away. Therefore, a slow oscillation in the build-up curve will be identified[5,17–22].

6.5.3 Rotational-echo adiabatic passage double resonance (REAPDOR)

The Rotational-echo adiabatic-passage double-resonance experiment is an expansion of Rotational-echo double-resonance (REDOR). It is well-documented tool which is designed to selectivity reintroduce the dipolar interaction between spin I=1/2 and spin S>1/2. Recovery of the heteronuclear dipole interaction between these two spins may be used to accurately measure the intera-nuclear distance since the dipolar interaction depends on the inverse cube of the distance between two nuclei. The REAPDOR experiment has been applied successfully to measure the distance between ^{13}C -^{11}B[23]. In order to obtain a REAPDOR curve, two experiments must be acquired as shown in (Figure 6-12), and the spinning rate has to be precise. One experiment is obtained with a middle pulse in the ^{11}B channel to recouple the heteronuclear interaction and measure the dephasing in ^{11}B signal S. Another experiment is also obtained with an elimination of the middle pulse in ^{11}B channel which will produce a reference signal S_0. The result is expressed according to Equation (6-8) which is a plot of that equation versus dipole evolution time. By fitting these data to a theoretical curve, information about the inter-molecular distance can be achieved.

$$\Delta S/S_0 = (S_0 - S)/S_0 \qquad (6\text{-}8)$$

6.5.4 2D Homonuclear correlation experiment

The objective of this experiment is to reintroduce the homonuclear coupling and identify the correlation between two identical nuclei such as ^{13}C -^{13}C. There are a variety of experiments, which can be done to achieve this goal such as Dipolar Rrecoupling Using A Windowless Sequence (DRAWS), finite pulse Radio-frequency-driven recoupling (fpRFDR), and SPC[24–26]. The 2- dimensional NMR spectrum is presented as a plot of intensity versus two frequencies as shown in (Figure 6-13)[8]. A precise interpretation of 2D spectrum can reveal useful information about the correlations between different nuclei in different environments. In 2D spectrum, cross peaks represent a correlation between two nuclei.

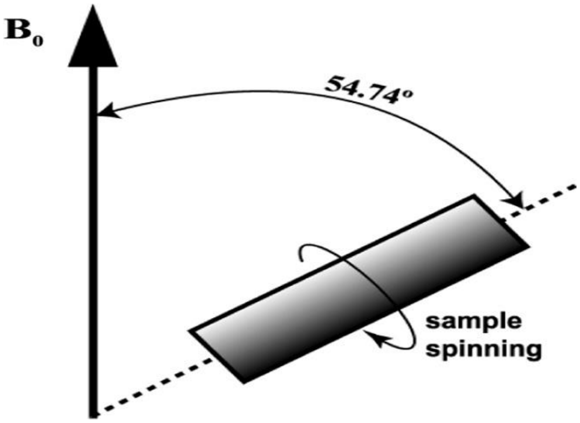

Figure 6-1. Placing the sample in the magic angle ($3\cos^2\Theta - 1 = 0$ when $\Theta = 54.74°$)

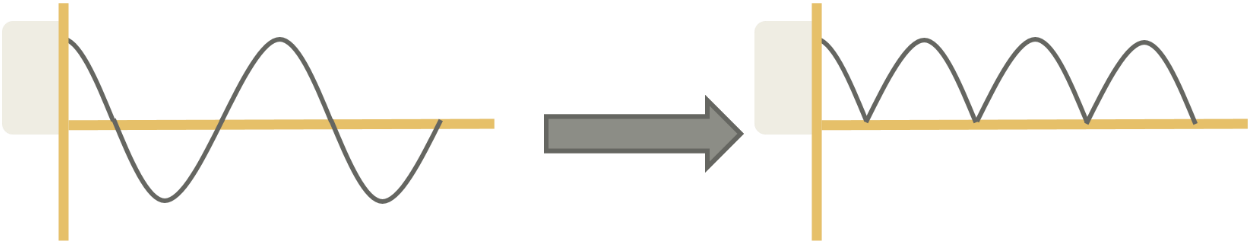

$$H_D = f(\theta)g(\hat{I} \cdot \hat{S})$$

Figure 6-2. Recoupling the dipolar interaction and first-order quadrupolar interactions under MAS by applying pulses to the spin state to change the product to a non-zero value

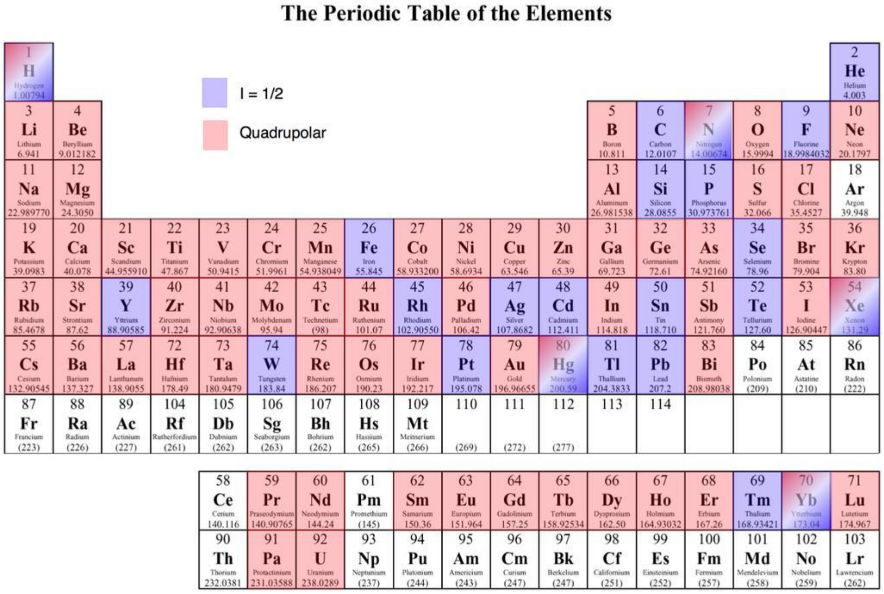

The Periodic Table of the Elements

🟪 I = 1/2

🟥 Quadrupolar

1 H Hydrogen 1.00794																	2 He Helium 4.003
3 Li Lithium 6.941	4 Be Beryllium 9.012182											5 B Boron 10.811	6 C Carbon 12.0107	7 N Nitrogen 14.00674	8 O Oxygen 15.9994	9 F Fluorine 18.9984032	10 Ne Neon 20.1797
11 Na Sodium 22.989770	12 Mg Magnesium 24.3050											13 Al Aluminum 26.981538	14 Si Silicon 28.0855	15 P Phosphorus 30.973761	16 S Sulfur 32.066	17 Cl Chlorine 35.4527	18 Ar Argon 39.948
19 K Potassium 39.0983	20 Ca Calcium 40.078	21 Sc Scandium 44.955910	22 Ti Titanium 47.867	23 V Vanadium 50.9415	24 Cr Chromium 51.9961	25 Mn Manganese 54.938049	26 Fe Iron 55.845	27 Co Cobalt 58.933200	28 Ni Nickel 58.6934	29 Cu Copper 63.546	30 Zn Zinc 65.39	31 Ga Gallium 69.723	32 Ge Germanium 72.61	33 As Arsenic 74.92160	34 Se Selenium 78.96	35 Br Bromine 79.904	36 Kr Krypton 83.80
37 Rb Rubidium 85.4678	38 Sr Strontium 87.62	39 Y Yttrium 88.90585	40 Zr Zirconium 91.224	41 Nb Niobium 92.90638	42 Mo Molybdenum 95.94	43 Tc Technetium (98)	44 Ru Ruthenium 101.07	45 Rh Rhodium 102.90550	46 Pd Palladium 106.42	47 Ag Silver 107.8682	48 Cd Cadmium 112.411	49 In Indium 114.818	50 Sn Tin 118.710	51 Sb Antimony 121.760	52 Te Tellurium 127.60	53 I Iodine 126.90447	54 Xe Xenon 131.29
55 Cs Cesium 132.90545	56 Ba Barium 137.327	57 La Lanthanum 138.9055	72 Hf Hafnium 178.49	73 Ta Tantalum 180.9479	74 W Tungsten 183.84	75 Re Rhenium 186.207	76 Os Osmium 190.23	77 Ir Iridium 192.217	78 Pt Platinum 195.078	79 Au Gold 196.96655	80 Hg Mercury 200.59	81 Tl Thallium 204.3833	82 Pb Lead 207.2	83 Bi Bismuth 208.98038	84 Po Polonium (209)	85 At Astatine (210)	86 Rn Radon (222)
87 Fr Francium (223)	88 Ra Radium (226)	89 Ac Actinium (227)	104 Rf Rutherfordium (261)	105 Db Dubnium (262)	106 Sg Seaborgium (263)	107 Bh Bohrium (262)	108 Hs Hassium (265)	109 Mt Meitnerium (266)	110 (269)	111 (272)	112 (277)	113	114				

58 Ce Cerium 140.116	59 Pr Praseodymium 140.90765	60 Nd Neodymium 144.24	61 Pm Promethium (145)	62 Sm Samarium 150.36	63 Eu Europium 151.964	64 Gd Gadolinium 157.25	65 Tb Terbium 158.92534	66 Dy Dysprosium 162.50	67 Ho Holmium 164.93032	68 Er Erbium 167.26	69 Tm Thulium 168.93421	70 Yb Ytterbium 173.04	71 Lu Lutetium 174.967
90 Th Thorium 232.0381	91 Pa Protactinium 231.03588	92 U Uranium 238.0289	93 Np Neptunium (237)	94 Pu Plutonium (244)	95 Am Americium (243)	96 Cm Curium (247)	97 Bk Berkelium (247)	98 Cf Californium (251)	99 Es Einsteinium (252)	100 Fm Fermium (257)	101 Md Mendelevium (258)	102 No Nobelium (259)	103 Lr Lawrencium (262)

Figure 6-3. Periodic table showing that 74% of active NMR isotopes are quadrupolar nuclei

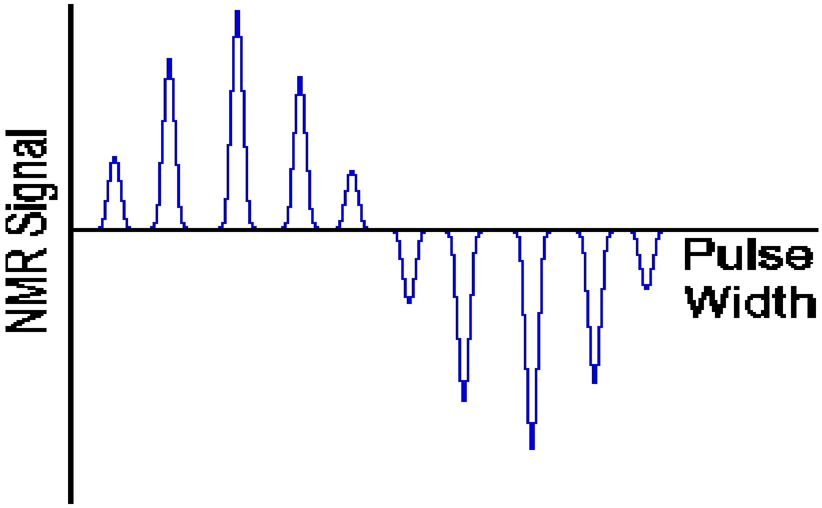

Figure 6-4. Nutation curve for the RF pulse calibration

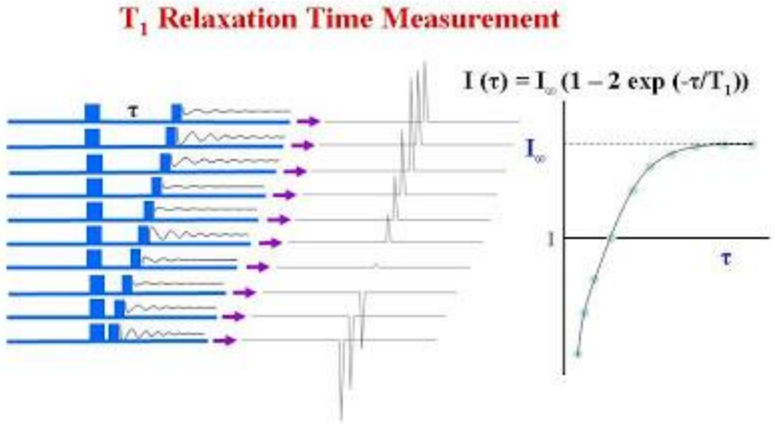

Figure 6-5. Inversion recovery experiment to measure T1

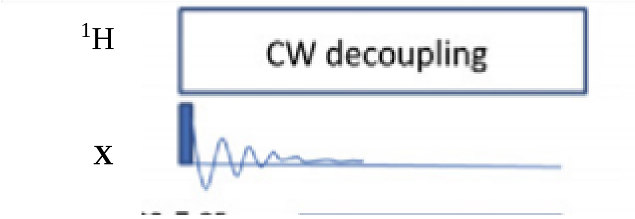

Figure 6-6. Pulse sequence of direct excitation

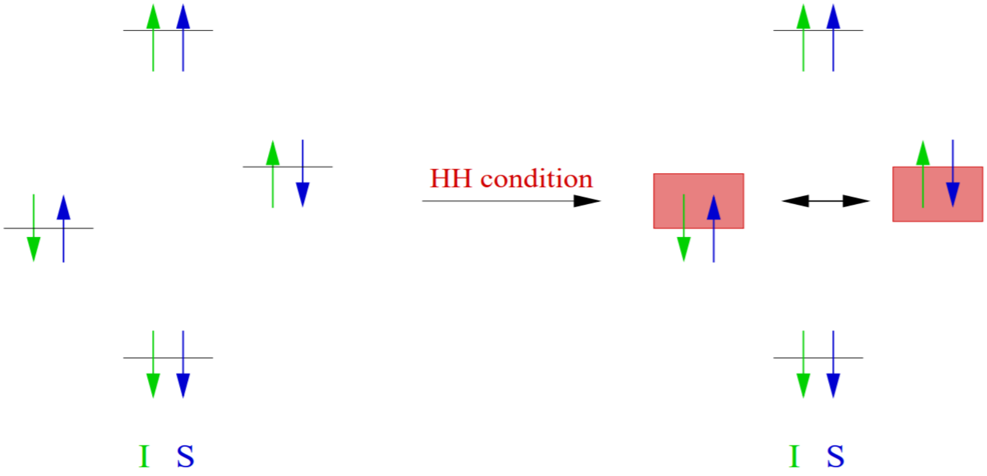

Figure 6-7. Magnetization transformation as energy level

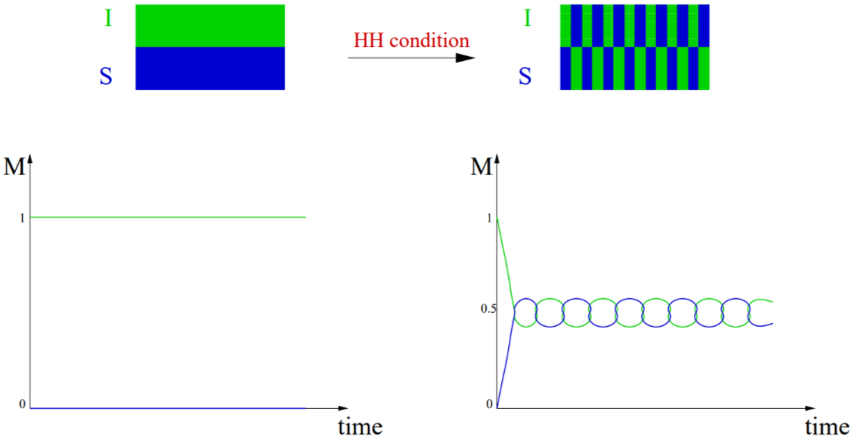

Figure 6-8. The polarization transfer

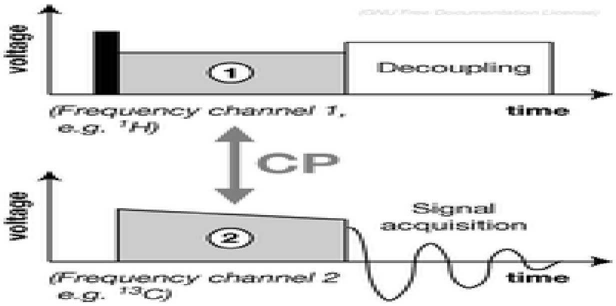

Figure 6-9. Cross polarization pulse sequence

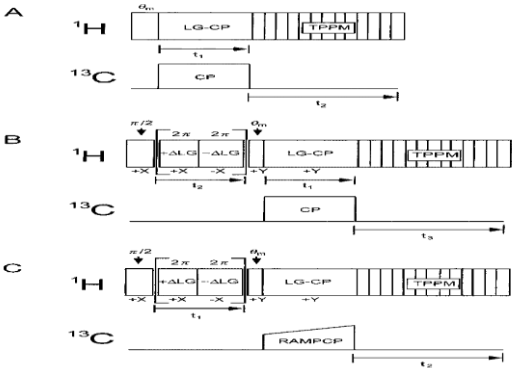

Figure 6-10.pulse sequence of the LG-CP experiment

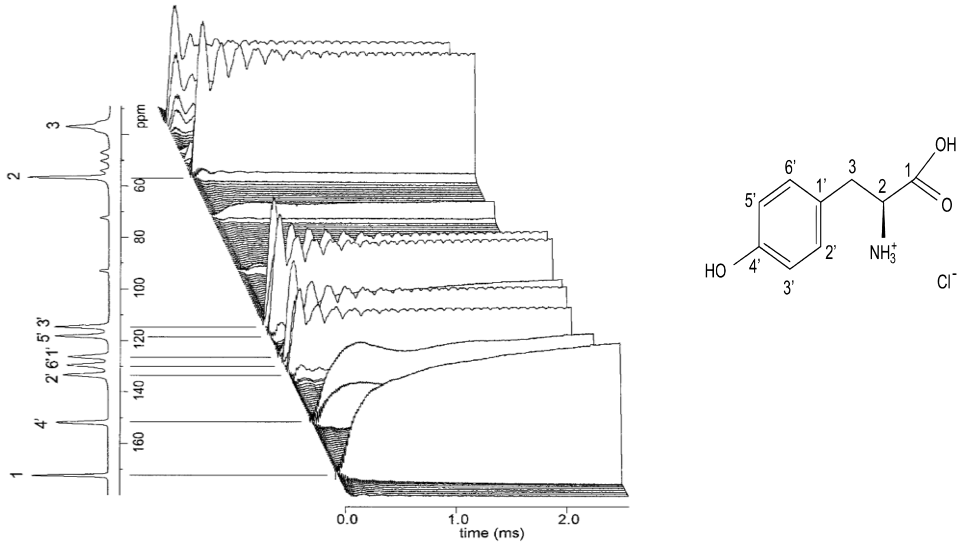

Figure 6-12. 2-D LG-CP build-up curves of tyrosine,HCl

Fast build up, and fast oscillation indicates short distance to nearest neighboring protons

Slow build up with slow or no oscillation indicates long distance

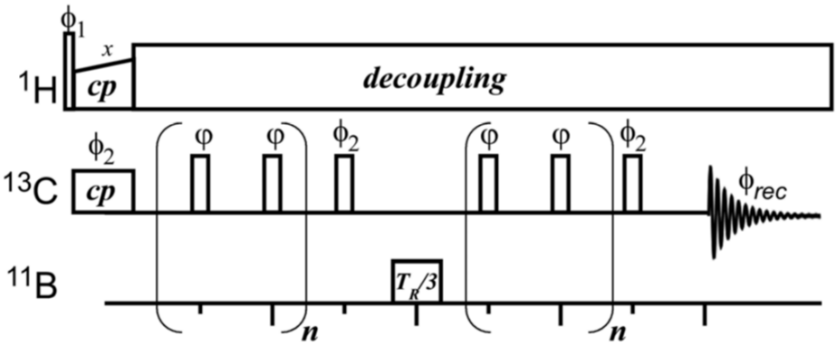

Figure 6-11. REAPDOR experiment pulse sequence

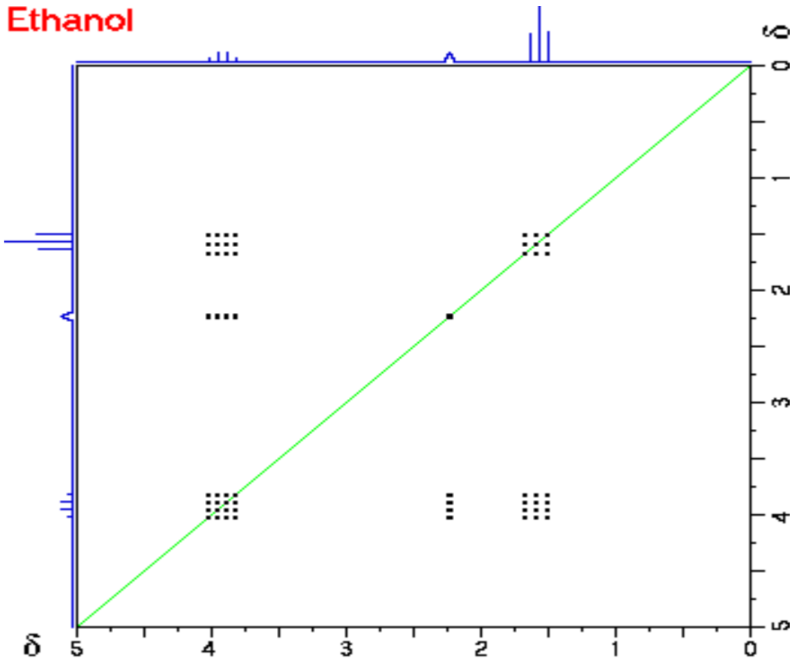

Figure 6-13. 2D NMR spectrum indicating possible correlations between peaks in ethanol

References

(1) Nagaraja, C. S.; Ramanathan, K. V. An Accurate and Simple Method for Setting the Magic Angle for Solid State NMR Studies. *J. Magn. Reson.* **2000**, *146* (1), 165–168. https://doi.org/10.1006/jmre.2000.2137.

(2) Khetrapal, C. .; Arun Kumar, B. .; Ramanathan, K. .; Suryaprakash, N. Setting the Magic Angle Using NMR Spectra of Oriented Molecules. *J. Magn. Reson.* **1987**, *73* (3), 516–518. https://doi.org/10.1016/0022-2364(87)90014-X.

(3) Bodenhausen, G.; Caravatti, P.; Deli, J.; Ernst, R. .; Sauter, H. Optical Alignment in Magic-Angle NMR. *J. Magn. Reson.* **1982**, *48* (1), 143–147. https://doi.org/10.1016/0022-2364(82)90246-3.

(4) Frye, J. S.; Maciel, G. E. Setting the Magic Angle Using a Quadrupolar Nuclide. *J. Magn. Reson.* **1982**, *48* (1), 125–131. https://doi.org/10.1016/0022-2364(82)90243-8.

(5) Taylor, R. E. 13C CP/MAS: Application to Glycine. *Concepts Magn. Reson. Part A Bridg. Educ. Res.* **2004**, *22* (2), 79–89. https://doi.org/10.1002/cmr.a.20015.

(6) Ashbrook, S. *Introduction To Quadrupolar NMR*; St Andrews, 2008.

(7) Freude, D. Quadrupolar Nuclei in Solid-State Nuclear Magnetic Resonance. *Encycl. Anal. Chem.* **2006**, 12188–12224. https://doi.org/10.1002/9780470027318.a6112.

(8) Hornak, J. P. *The Basic of NMR*; Rochester, NY.

(9) Lindon, J. *Introduction to Solid-State NMR Spectroscopy, by Melinda J. Duer. Blackwell Science, Oxford, 2004, ISBN 1-4051-0914-9, 349 Pp.*; 2005; Vol. 18. https://doi.org/10.1002/nbm.948.

(10) Facey, G. University of Ottawa NMR Facility Blog. A blog for the NMR users at the University of Ottawa and all others interested in NMR spectroscopy.

http://www.nmr.uottawa.ca/en/welcome.html.

(11) Paquette, M. M.; Li, W.; Sky Driver, M.; Karki, S.; Caruso, A. N.; Oyler, N. A. The Local Physical Structure of Amorphous Hydrogenated Boron Carbide: Insights from Magic Angle Spinning Solid-State NMR Spectroscopy. *J. Phys. Condens. Matter* **2011**, *23* (43), 2–6. https://doi.org/10.1088/0953-8984/23/43/435002.

(12) Ladizhansky, V.; Vega, S. Article A Method for Measuring Heteronuclear (H − C) Distances in High Speed MAS NMR A Method for Measuring Heteronuclear (1 H- 13 C) Distances in High Speed MAS NMR. *Society* **2000**, No. 10, 3465–3472. https://doi.org/10.1021/ja992714j.

(13) Hong, M.; Yao, X.; Jakes, K.; Huster, D. Investigation of Molecular Motions by Lee-Goldburg Cross-Polarization NMR Spectroscopy. *J. Phys. Chem. B* **2002**, *106* (29), 7355–7364. https://doi.org/10.1021/jp0156064.

(14) Solid-state nuclear magnetic resonance. https://en.wikipedia.org/wiki/Solid-state_nuclear_magnetic_resonance.

(15) Lee, M.; Goldburg, W. I. Nuclear-Magnetic-Resonance Line Narrowing by a Rotating Rf Field. *Phys. Rev.* **1965**, *140* (4A). https://doi.org/10.1103/PhysRev.140.A1261.

(16) Reich, H. J. *Relaxation in NMR Spectroscopy*; Wisconsin, 2017.

(17) Samoson, A.; Tuherm, T.; Past, J. Ramped-Speed Cross Polarization MAS NMR. *J. Magn. Reson.* **2001**, *149* (2), 264–267. https://doi.org/10.1006/jmre.2001.2302.

(18) Tripon, C.; Aluas, M.; Filip, X.; Filip, C. Polarization Transfer from Remote Protons in 13C CP/MAS. *J. Magn. Reson.* **2006**, *183* (1), 68–76. https://doi.org/10.1016/j.jmr.2006.07.019.

(19) Smith, M. E.; Strange, J. H. NMR Techniques in Materials Physics: A Review. *Meas. Sci. Technol.* **1996**, *7* (4), 449–475. https://doi.org/10.1088/0957-0233/7/4/002.

(20) Stevanato, G. Long-Lived States in Multi-Spin Systems. Ph.D. Dissertation, UNIVERSITY OF SOUTHAMPTON, 2015.

(21) Laws, D. D.; Bitter, H.-M. L.; Jerschow, A. Solid-State NMR Spectroscopic Methods in Chemistry. *Angew. Chemie Int. Ed.* **2002**, *41* (17), 3096–3129. https://doi.org/10.1002/1521-3773(20020902)41:17<3096::AID-ANIE3096>3.0.CO;2-X.

(22) Alia, A.; Ganapathy, S.; De Groot, H. J. M. Magic Angle Spinning (MAS) NMR: A New Tool to Study the Spatial and Electronic Structure of Photosynthetic Complexes. *Photosynth. Res.* **2009**, *102* (2–3), 415–425. https://doi.org/10.1007/s11120-009-9478-3.

(23) Wang, J.; Balazs, Y. S.; Thompson, L. K. Solid-State REDOR NMR Distance Measurements at the Ligand Site of a Bacterial Chemotaxis Membrane Receptor †. *Biochemistry* **1997**, *36* (7), 1699–1703. https://doi.org/10.1021/bi962578k.

(24) Drobny, G. P.; Gregory, D. M.; Shiels, J. C.; Kiihne, S.; Hatcher, M. E.; Mitchell, D. J.; Mehta, M. A. Distance Measurements in Nucleic Acids Using Windowless Dipolar Recoupling Solid State NMR. *Solid State Nucl. Magn. Reson.* **2002**, *7* (3), 211–228. https://doi.org/10.1016/s0926-2040(96)01267-2.

(25) Oyler, N. A.; Tycko, R. Multiple Quantum 13 C NMR Spectroscopy in Solids under High-Speed Magic-Angle Spinning †. *J. Phys. Chem. B* **2002**, *106* (33), 8382–8389. https://doi.org/10.1021/jp020906m.

(26) Zhang, R.; Nishiyama, Y.; Sun, P.; Ramamoorthy, A. Phase Cycling Schemes for Finite-Pulse-RFDR MAS Solid State NMR Experiments. *J. Magn. Reson.* **2015**, *252*, 55–66. https://doi.org/10.1016/j.jmr.2014.12.010.

Chapter 7 . STRUCTURE DETERMINATION OF BORON CARBIDE THIN FILMS USING SOILD STATE NMR SPECTROSCOPY

7.1 Introduction

Boron carbides (BC) are a class of icosahedral boron-rich molecular solids. They are known as one of the hardest materials at room temperature. Moreover, they are chemically inert, and very thermostable. Although boron has three valence electrons, it has the tendency to form unusual three-center two-electron bonds and is inclined to organize itself in stable deltahedra (Figure 7-1). On account of their unique thermal, mechanical, and electrical properties, boron rich carbides have many applications including, protective armor due to its light weight and neutron detectors because of the high cross section for the absorption of neutrons (^{10}B). Boron rich carbides may be formulated as low-k dielectric materials, which can be utilized for ultra large scale integrated circuit design. Additionally, they are used as p-type semiconductors in the semiconductor devices[1–5].

The local physical structure of boron carbide has been the subject of many studies[2,6]. The lattice structure of crystalline boron carbide has twelve icosahedra at the vertices of a rhombohedral unit cell (Figure 7-2). There are six atoms in each icosahedron at polar sites and they are bound directly to neighboring icosahedra. Furthermore, six equatorial atoms are bound to the three-atom chain, which is located on the crystallographic c axis. The stoichiometry of crystalline boron carbide can range from $B_{4.3}C$ to $B_{11.2}C$ without undergoing a phase change. It is known that at the carbon-rich limit ($B_{4.3}C$) is composed mostly of $B_{11}C$ icosahedra and C-B-C chains. As the relative boron content increases and the solid becomes more boron rich, B atoms are replaced with C atoms, one by one. Amorphous hydrogenated boron carbide has a similar icosahedral building block; however, the physical structure is essentially different. The reason for this difference is the lack of long-range order along with the attachment of hydrogen[7].

Many studies have been done to discover the local structure of boron rich carbide[8,9]. However, these studies do not give conclusive evidence for the structure of the thin film. Diffraction techniques (X-ray, neutron, electron) are methods used to identify the atomic and molecular structure of crystal[10]. Pair distribution functions use the distribution of bond lengths and interatomic distances to illustrate structural information. However, this study works with boron and carbon, which are known as low Z materials and low X-ray atomic scattering factors. Thus, the intensity is too weak, and it is hard to acquire any structural information from these techniques. The electron atomic scattering factors for B and C are much larger than X-ray atomic scattering factors by a factor of $\sim 10^8$. Accordingly, it is accessible to identify the structure of thin films. On the other hand, the resolution is low due to the complex and amorphous structure. The neutron scattering of B and C are not distinguishable from each other since they have very close neutron scattering lengths. In addition, the neutron source is too expensive and that bounds the operation of this technique.

X-ray photoemission spectroscopy (XPS), also known as electron spectroscopy for chemical analysis (ESCA), is another tool that can aid in identifying the local structure of boron carbide thin films. XPS is a surface-sensitive quantitative spectroscopic technique that has been widely used to analyze the surface chemistry of boron carbide thin film[11,12]. XPS can probe the empirical formula, chemical state, electronic state of elements that are present in these materials. The average depth of analysis for an XPS measurement is approximately (0-10nm). Hence, only the elements on the surface will be recognized. If the surface is different from what is below, the determination of the inner structure would be missing. A depth profile experiment can be performed, but the deeper we go the more energy goes into the sample, which would cause a change or damage the structure. Moreover, XPS does not easily detect elements with a low atomic number (Z) like hydrogen (Z=1) or Helium (Z=2), and it is more challenging to detect B and C in which the signal to noise ratio is weaker than heavier atoms. Under these circumstances, we might overestimate the ratio between the elements. Therefore, these weaknesses of XPS spectroscopy restrict a consistent use of XPS in the characterization of boron carbide thin films structure.

Near Edge X-Ray Absorption Fine Structure (NEXAFS) spectroscopy is an element specific method. It usually measures the light elements like carbon, oxygen, and nitrogen, and it is essentially equivalent to X-Ray Absorption Near Edge Structure (XANES) spectroscopy. These techniques can be helpful in probing the local physical structure of boron carbide by determining the local bonding and the oxidation state of the elements[13,14]. Continued scanning leads into what is called Extended X-ray Absorption Fine Structure (EXAFS) spectroscopy. This contains information about interactions with the nearest neighbor atom as well as bond order. Although these techniques can illuminate structural clues to the overall physical structure of boron carbide thin films, the spectra are difficult to interpret.

Electron microprobe analysis (EMPA), also named electron probe microanalysis (EPMA), is a non-destructive analytical method to characterize the chemical composition of a few mm in the substantial size. EPMA has been used for defining the electronic structure of graphite[15] . EPMA not only identifies the electronic structure but also provides valuable information about bonds in carbon and boron materials. EMPA falls short because it cannot detect Hydrogen, so we cannot count on this technique to characterize the local physical structure of boron carbide.

Fourier transform infrared spectroscopy (FT-IR) has been a workhorse tool for qualitative and quantitative examination of the local physical structure of boron carbide thin films. FT-IR can measure the absorption or emission of a liquid, solid, or gas. The critical information that can be acquired from FT-IR spectroscopy is bond types and functional groups of boron carbide thin films through the analysis of local vibrational modes. Even though FT-IR has revealed relatively insightful information about the local physical structure of boron carbide thin films, key information is still unknown, such as the position of these bonds and the connectivity between the elements. Additionally, sometimes it is hard to interpret FT-IR data. For these reasons, other techniques must be used in conjugation with FT-IR spectroscopy to fully characterize the local physical structure of boron carbide thin films[16–18].

In contrast to other spectroscopic methods, NMR does not require long-range constitutional order. It can efficaciously study the short-range chemical and physical structure as well as the intermediate–range connectivity. The spectrum can be interpreted entirely. It can expose the structure and chemical environment of molecules, as well as reaction dynamics, and reaction states. Additionally, NMR extends further than all possible techniques by obtaining 2D experiments, which allows the flexibility to manipulate the spectrum and isolate different atoms.

7.2 General Research Approach

The current study investigates the local physical structure of boron carbide thin-films. Even when using the same material precursor (ortho-carborane and labeled methane), the properties of hydrogenated boron carbide thin films vary considerably under different experimental conditions. With various properties, each of these thin films can be suitable for different types of semiconductor devices. Considering the fact that an identical precursor can lead to thin films with distinct properties clearly means that there are local, molecular structural differences between these. Hence, this study investigates the local structure of boron carbide thin films, which will help to correlate the structure and properties of thin film. Understanding this relationship will help to discover the best conditions for making more efficient semi-conductor devices.

Plasma enhanced chemical vapor deposition (PECVD) was utilized to grow different materials under different growth conditions. Solid-state NMR spectroscopy techniques were applied to characterize the local physical structure of thin films.

7.3 Film growth and sample preparation

Plasma enhanced chemical vapor deposition (PECVD) was used to grow boron-carbide thin films (Figure 7-3)[18]. In this process,^{13}C-labeled methane and ortho-carborane were sublimed. The ^{13}C-labeled methane and ortho-carborane gases were delivered to the reactor using Ar gas as a carrier gas. With the starting materials and Ar gasses present in the plasma, the chemical reaction took place. Fragments are deposited on Al substrate[19].

7.4 SSNMR experiments

All the SSNMR spectroscopy was carried out on a three channel Tecmag Apollo console with 8.45 T magnet and homebuilt double- and triple-resonance SSNMR probes. For ^{11}B, ^{13}C spectra, 3.2 mm probe was used with MAS frequency 10 KHz to obtain the best resolution. The frequency of detecting nuclei, namely ^{1}H, ^{11}B, and ^{13}C are 357.200 MHz, 114.602 MHz, and 89.821MHz respectively. With three active nuclei, there are quite a few SSNMR experiments that can illustrate the local physical structure of boron carbide thin films as they were discussed in detail in previous chapter.

7.5 Results and discussion

7.5.1 Film growth and sample preparation

Table 7-1 shows the growth condition of the interest materials. Thin films of ^{13}C-labeled methane and ortho-carborane grew successfully with a thickness up to 2-3 um. The thin-films were isolated from Al substrate by dissolving the substrate in dilute HCl [19]. The treatment of thin films with HCl may influence the physical or chemical structure of thin films, but insignificant changes in IR spectra were detected before and after the treatment with HCl. By using dilute HCl, a sufficient amount of isolated materials can be obtained at a low cost. In order to prepare the samples for SSNMR studies, the isolated materials were crushed gently and packed in the rotors at a weight of approximately 2mg per sample in each rotor.

7.5.2 Direct excitation experiment

Figure 7-4 shows the ^{11}B NMR spectra of three different thin films namely: M13C3, M13C4, and M13C5. According to the spectra, no shift in ^{11}B peak has been observed. Therefore, the ^{11}B in all of these samples have the same chemical environment.

7.5.3 Lee-Goldburg Cross Polarization experiment (LGCP)

The LGCP experiment provides information about the strength of the interaction between ^{13}C-^{1}H. Figure 7-5 illustrates the result of LG-CP experiment for the reference U-^{13}C Alanine. By looking at the shape of each buildup curve and the time scale, we clearly can notice a different strength of interaction between ^{13}C and ^{1}H. In the alpha carbon, the oscillation was very fast and the buildup curve time was rapid which confirms that proton and carbon are adjacent. For the methyl group, the oscillation and the buildup curve was not as fast as alpha and that approves a small distance between carbon and proton. Carbonyl, on the other hand, has a slower oscillation and longer buildup curve time, which indicates that carbonyl has a proton but not that nearby. All our samples behave similarly in LG-CP experiment. Figures (7-6 A, B, and C) show the result of LG-CP experiment for all thin films. When examining across the peak from left to right, the interactions are clearly changing. There is a different oscillation and buildup curve time in each side of the peak for each sample. Therefore, we have slightly different chemical environment across the peak.

7.5.4 Rotational-echo adiabatic passage double resonance (REAPDOR)

The results of REAPDOR experiments are shown in (Figures 7-7 A, B, and C). The spectra were acquired at a different time scale. The blue spectra S is the dephased, while the red spectra is the control S_o). Since there was no difference detected between S and S_o signals, there are not boron bound to the carbon. Approximately all the samples have the same carbon and boron distribution.

7.5.5 2D-SPC Homonuclear correlation experiment

Figure 7-8 illustrates the correlation in the control sample UALA. However, the samples M13C4, 5 revealed no correlation since no off diagonal pieces have been observed (Figure 7-9 A and B). The result obtained was not unexpected since only part of the sample was labeled.

7.6 conclusion and future work

In conclusion, we have moderately collected some information about the ^{13}C labeled methane and ortho- carborane thin films grown by PECVD. Our analysis was hampered by a low signal-to-noise ratio due to the low natural abundance of ^{13}C, and the useful information that we could obtain from SSNMR spectroscopy about the local physical structure of ortho-carborane thin film was dramatically reduced.

Consequently, for the future work, we are planning to isotopically enrich the precursor ortho-carborane with ^{13}C carbons. Using^{13}C labeled ortho-carborane would have major outcomes: improvement in S/N by a factor of ~90 fold in ^{13}C experiment, and the ability to measure interatomic distances by doing carbon-carbon correlation experiments and 2D experiments. We have started synthesizing ortho-carborane as shown in the synthetic scheme in Appendix I.

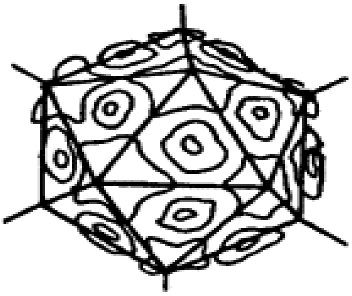

Figure 7-1. The icosahedral building block of boron-rich solids, with contours illustrating bonding electron density.

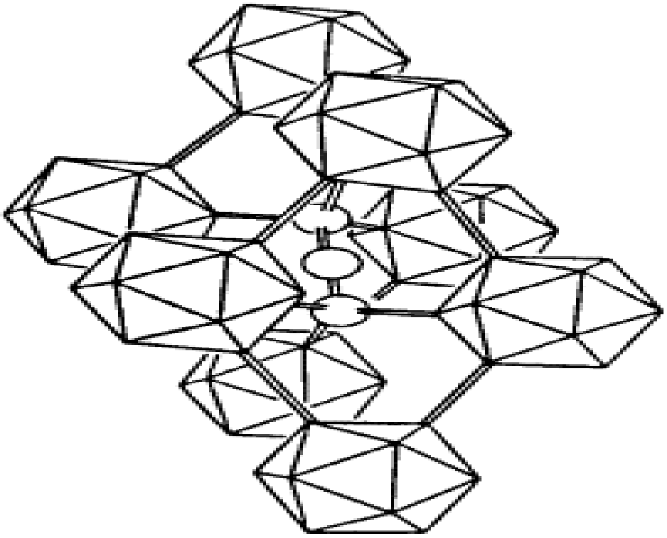

Figure 7-2. Boron carbide crystal structure

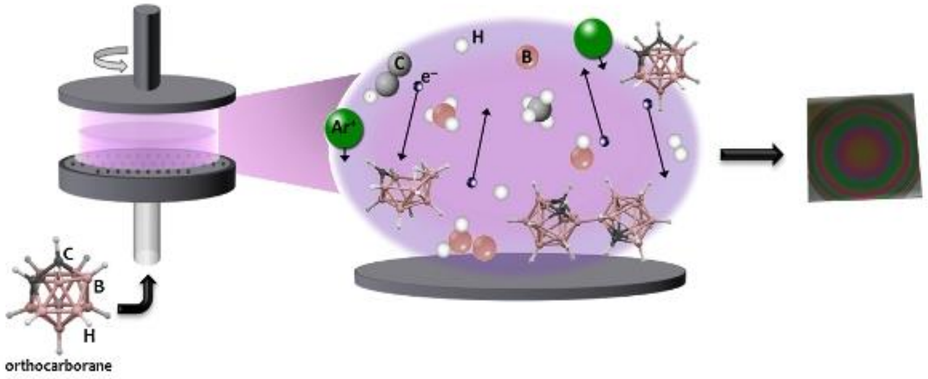

Figure 7-3. Plasma enhanced chemical vapor deposition PECVD growth of thin film

Table 7-1. Growth condition of thin films using PECVD

Name	Power	Temperature	Pressure	Ar+ortho	Methane ^{13}C	Growth time
M13C_3	40W	275C	2 Torr	190sccm*	10 sccm	30 min
M13C_4	40W	275C	2 Torr	150sccm*	50 sccm	30 min
M13C_5	40W	275C	2 Torr	175sccm*	25 sccm	30 min

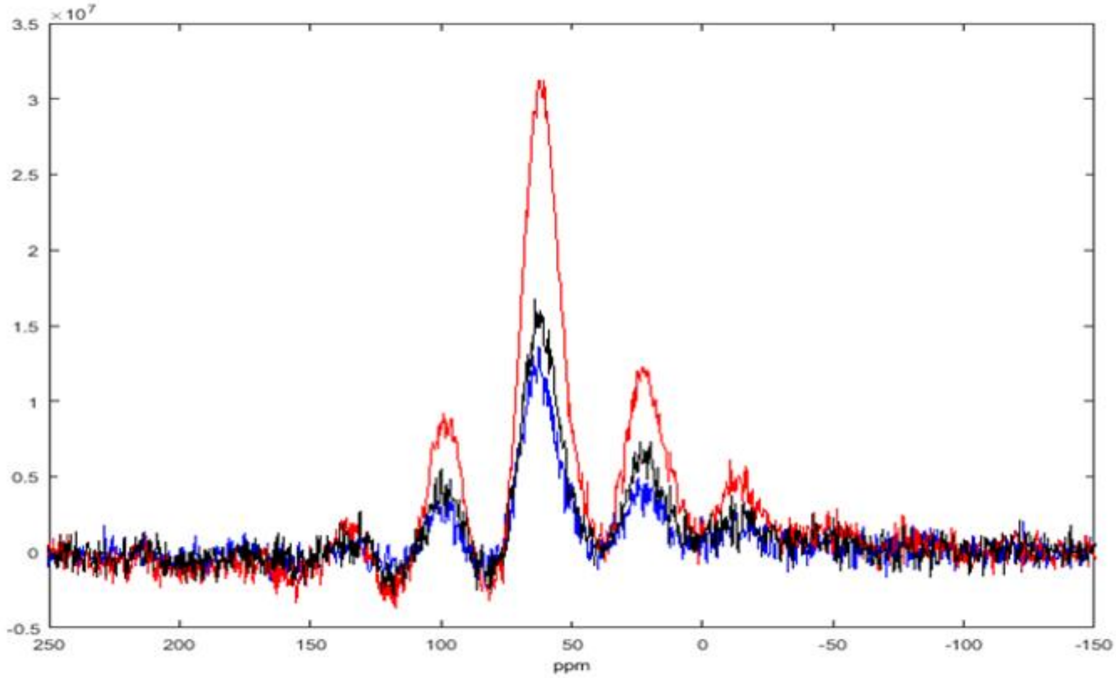

Figure 7-4. ^{11}B NMR spectra, direct excitation experiment

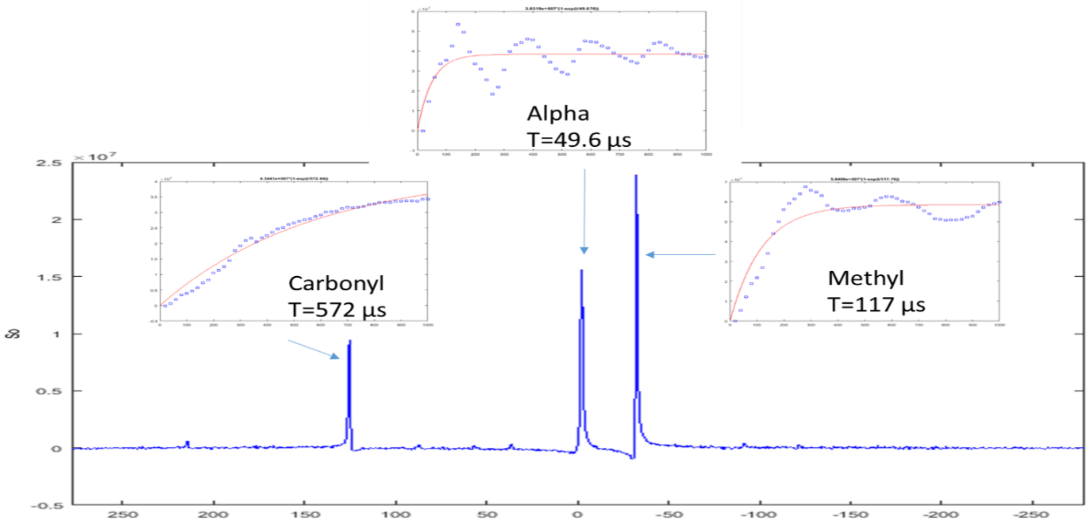

Figure 7-5. LG-CP result for reference U-^{13}C Alanine

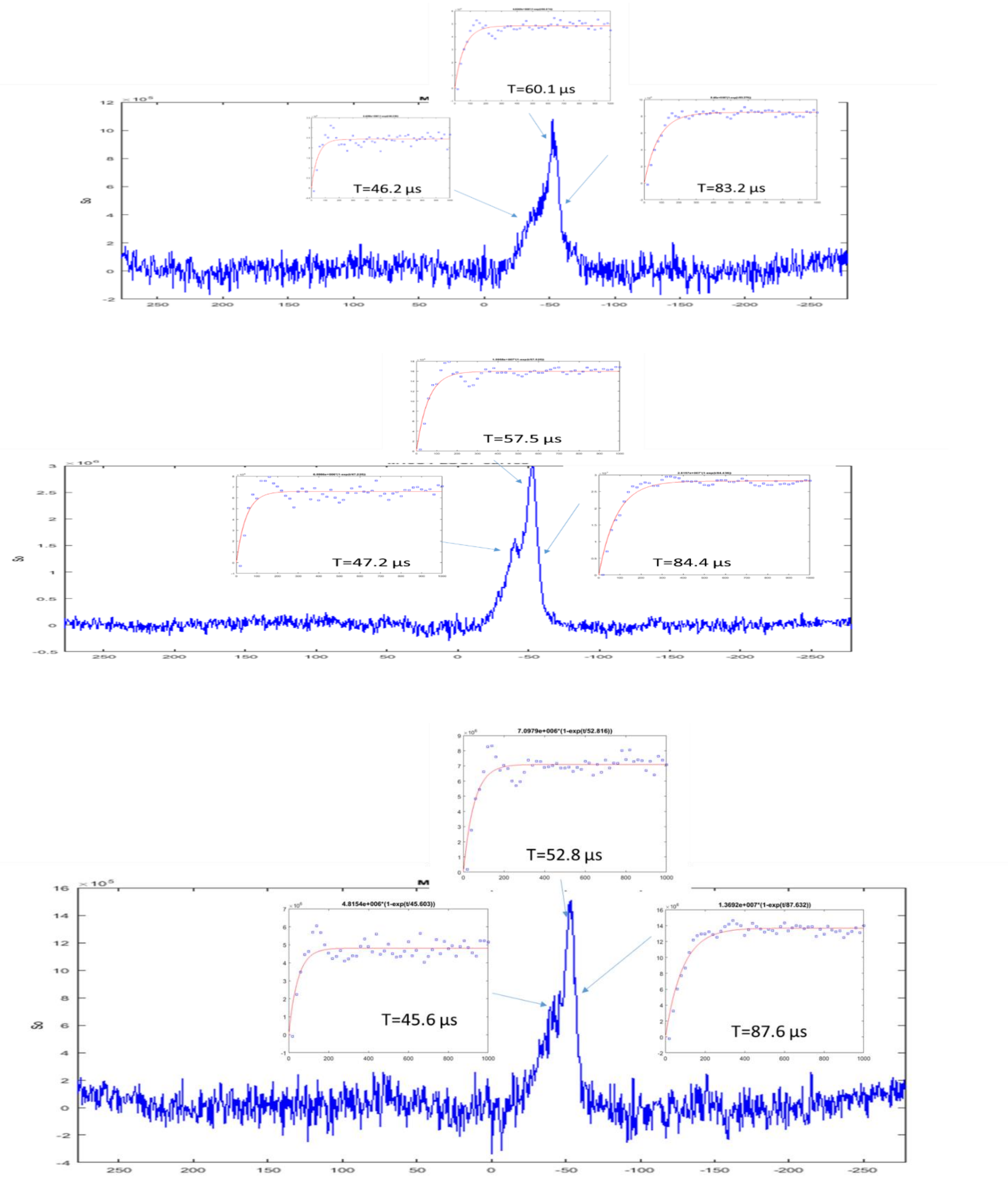

Figure 7-6. LG-CP results for all thin films A: M13C3, B: M13C4, and C: M13C5

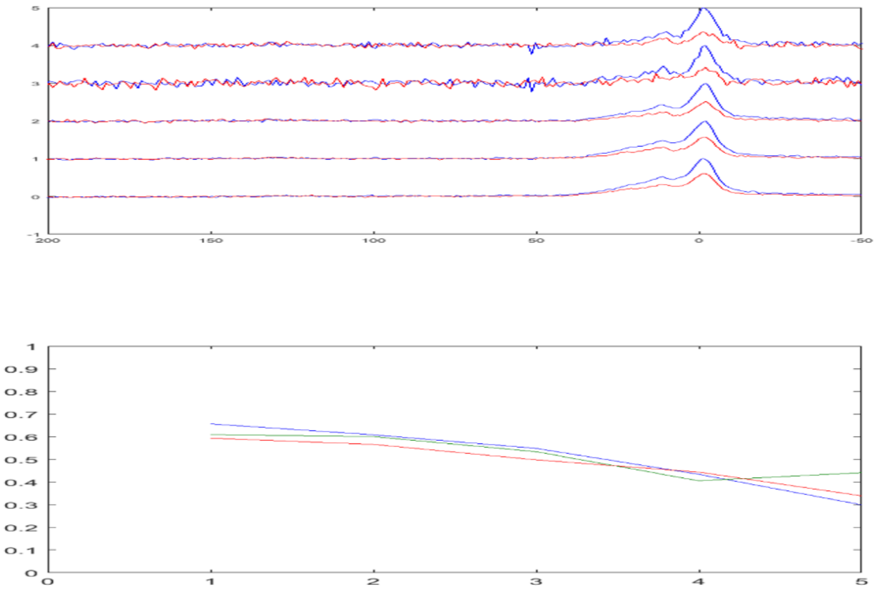

REAPDOR results for all thin film A: M13C3

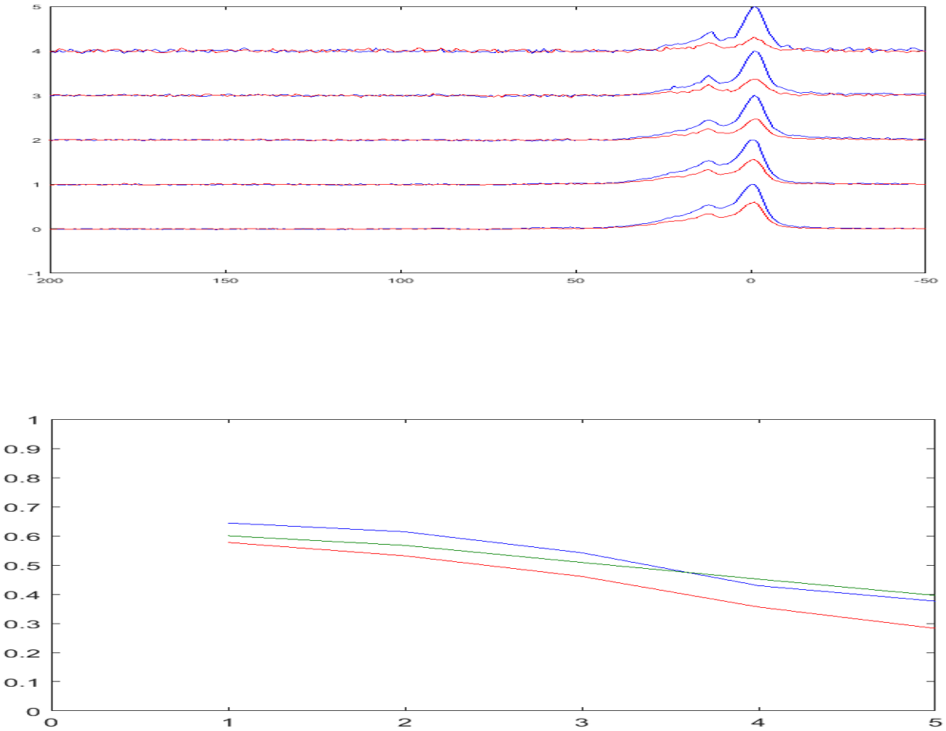

REAPDOR results for all thin films B: M13C4

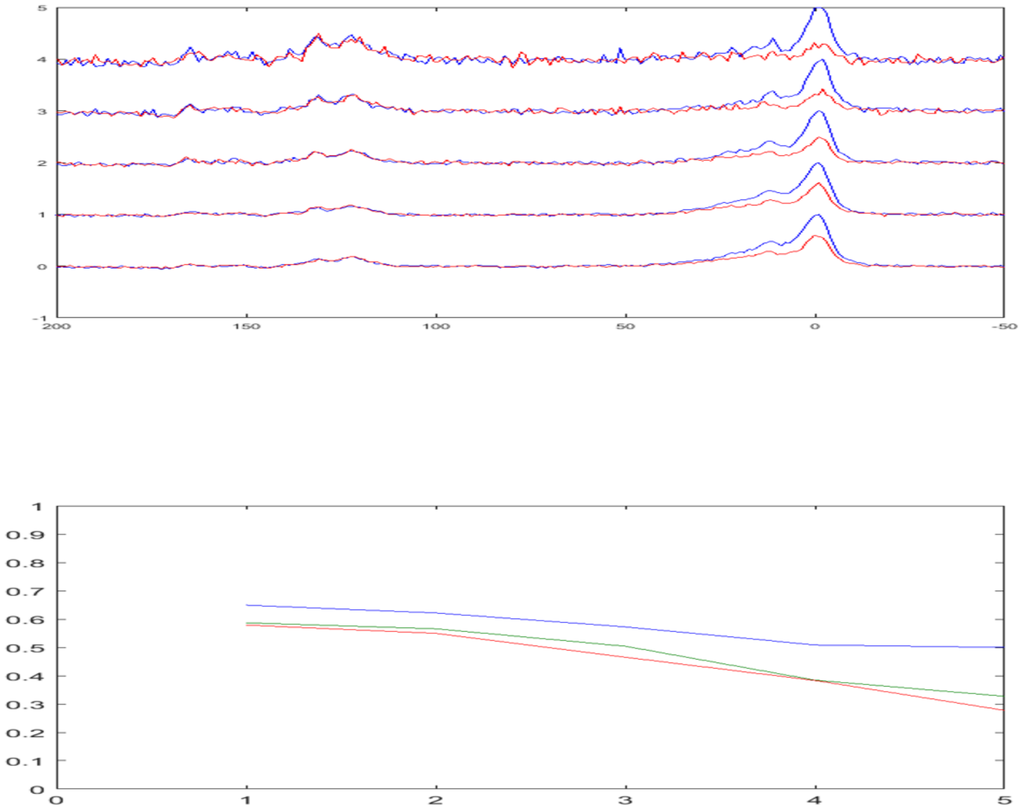

Figure 7-7. REAPDOR results for all thin films A: M13C3, B: M13C4, and C: M13C5

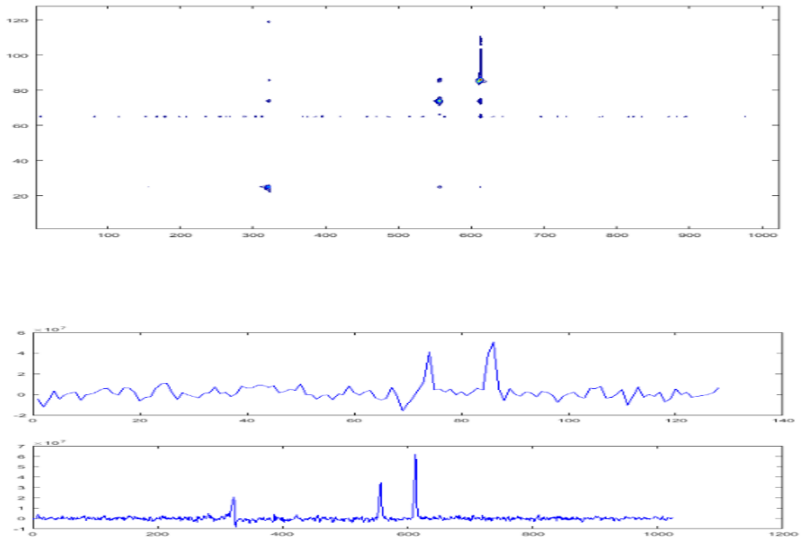

Figure 7-8. 2D-SPC result for UALA control to demonstrate pulse sequence is correct

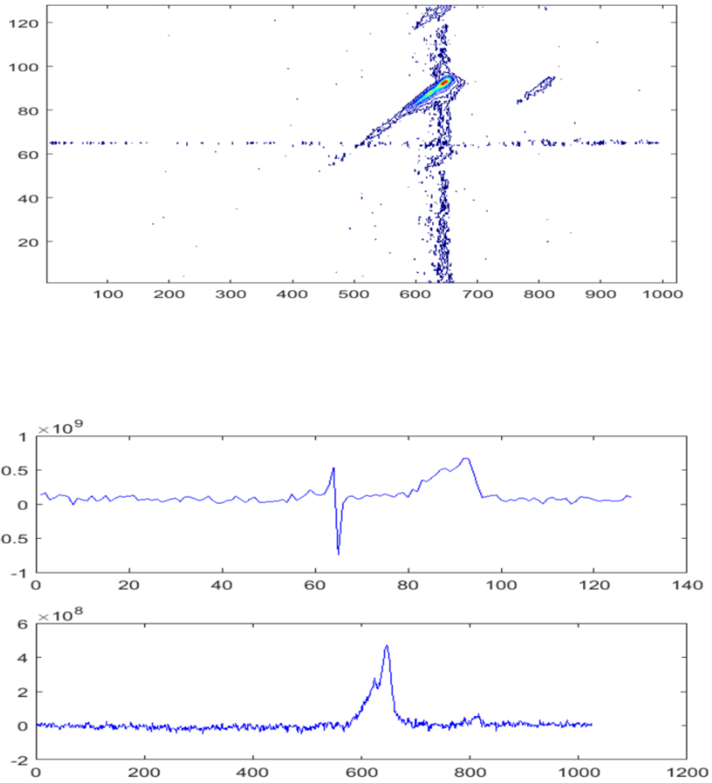

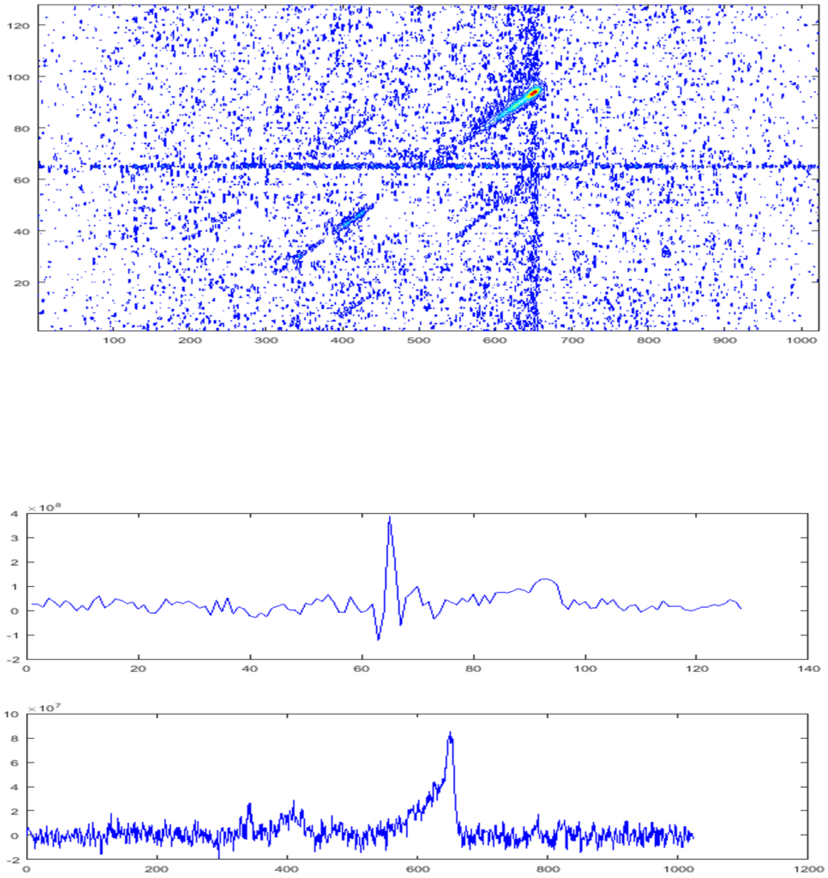

Figure 7-9. 2D-SPC results thin films A: M13C4, and B: M13C5

References:

(1) Braddock-wilking, J.; Lin, S.; Feldman, B. J. Evidence for and Role of Boron Carbide Icosahedra in the Hardness of Amorphous Hydrogenated Boron Carbide. *Tribol. Lett.* **1998**, *5*, 145–148. https://doi.org/https://doi.org/10.1023/A:1019173120525.

(2) Emin, D. Unusual Properties of Icosahedral Boron-Rich Solids. *J. Solid State Chem.* **2006**, *179* (9), 2791–2798. https://doi.org/10.1016/j.jssc.2006.01.014.

(3) Vast, N.; Sjakste, J.; Betranhandy, E. Boron Carbides from First Principles. *J. Phys. Conf. Ser.* **2009**, *176*. https://doi.org/10.1088/1742-6596/176/1/012002.

(4) Balakrishnarajan, M. M.; Pancharatna, P. D.; Hoffmann, R. Structure and Bonding in Boron Carbide: The Invincibility of Imperfections. *New J. Chem.* **2007**, *31* (4), 473–485. https://doi.org/10.1039/b618493f.

(5) Sasaki, S.; Takeda, M.; Yokoyama, K.; Miura, T.; Suzuki, T.; Suematsu, H.; Jiang, W.; Yatsui, K. Thermoelectric Properties of Boron-Carbide Thin Film and Thin Film Based Thermoelectric Device Fabricated by Intense-Pulsed Ion Beam Evaporation. *Sci. Technol. Adv. Mater.* **2005**, *6* (2), 181–184. https://doi.org/10.1016/j.stam.2004.11.010.

(6) Paquette, M. M.; Li, W.; Sky Driver, M.; Karki, S.; Caruso, A. N.; Oyler, N. A. The Local Physical Structure of Amorphous Hydrogenated Boron Carbide: Insights from Magic Angle Spinning Solid-State NMR Spectroscopy. *J. Phys. Condens. Matter* **2011**, *23* (43), 435002. https://doi.org/10.1088/0953-8984/23/43/435002.

(7) Werheit, H. Are There Bipolarons in Icosahedral Boron-Rich Solids? *J. Phys. Condens. Matter* **2007**, *19* (18). https://doi.org/10.1088/0953-8984/19/18/186207.

(8) Ivashchenko, V. I.; Shevchenko, V. I.; Turchi, P. E. A. First-Principles Study of the Atomic and Electronic Structures of Crystalline and Amorphous B4C. *Phys. Rev. B* **2009**, *80* (23),

235208. https://doi.org/10.1103/PhysRevB.80.235208.

(9) Paquette, M. M.; Li, W.; Sky Driver, M.; Karki, S.; Caruso, A. N.; Oyler, N. A. The Local Physical Structure of Amorphous Hydrogenated Boron Carbide: Insights from Magic Angle Spinning Solid-State NMR Spectroscopy. *J. Phys. Condens. Matter* **2011**, *23* (43), 2–6. https://doi.org/10.1088/0953-8984/23/43/435002.

(10) Bao, R.; Chrisey, D. B. Short Range Order Structure of Amorphous B4C Boron Carbide Thin Films. *J. Mater. Sci.* **2011**, *46* (11), 3952–3959. https://doi.org/10.1007/s10853-011-5320-3.

(11) Jacobsohn, L.; Schulze, R.; Maiadacosta, M.; Nastasi, M. X-Ray Photoelectron Spectroscopy Investigation of Boron Carbide Films Deposited by Sputtering. *Surf. Sci.* **2004**, *572* (2–3), 418–424. https://doi.org/10.1016/j.susc.2004.09.020.

(12) Department of Physics and Materials Science University of Hong Kong City Surface Science Western, UWO. http://mmrc.caltech.edu/SS_XPS/XPS_PPT/XPS_Slides.

(13) Zhang, D.; Mcilroy, D. N.; O'Brien, W. L.; De Stasio, G. The Chemical and Morphological Properties of Boron-Carbon Alloys Grown by Plasma-Enhanced Chemical Vapour Deposition. *J. Mater. Sci.* **1998**, *33* (20), 4911–4915. https://doi.org/https://doi.org/10.1023/A:1004422016254.

(14) NEXAFS Spectroscopy. https://www-ssrl.slac.stanford.edu/stohr/nexafs.htm.

(15) Zalavutdinov, R. K.; Gorodetsky, A. E.; Zakharov, A. P. Study of Chemical Bonds in Carbon and Boron Materials by EPMA. *Diam. Relat. Mater.* **1995**, *4* (12), 1383–1385. https://doi.org/10.1016/0925-9635(95)00326-6.

(16) Beckmann, R.; Jacob, W.; Annen, A.; Saß, M.; von Keudell, A. Structure of Plasma-Deposited Amorphous Hydrogenated Boron-Carbon Thin Films. *Thin Solid Films* **2002**,

312 (1–2), 147–155. https://doi.org/10.1016/s0040-6090(97)00735-9.

(17) Molecular Materials Research Center. Beckman institute California Technology. http://mmrc.caltech.edu/FTIR/FTIRintro.pdf.

(18) Billa, R. B.; Hofmann, T.; Schubert, M.; Robertson, B. W. Annealing Effects on the Optical Properties of Semiconducting Boron Carbide. *J. Appl. Phys.* **2009**, *106* (3), 25–29. https://doi.org/10.1063/1.3190679.

(19) Braddock-Wilking, J.; Lin, S. H.; Feldman, B. J. 13C NMR Spectroscopy of Amorphous Hydrogenated Carbon - Further Evidence of Inhomogeneity. *Solid State Commun.* **2001**, *119* (1), 19–21. https://doi.org/10.1016/S0038-1098(01)00205-8.

Chapter 8 . STUDY THE OPTICAL PROPERTIES OF TIO_2 USING SOILD STATE NMR SPECTROSCOPY

8.1 Introduction

Titanium oxide plays a significant role as a photocatalyst due to its distinctive photocatalytic activity. However, the band gap of TiO_2 is actually wide, about 3.0-3.2 ev, and absorbs only the ultra-violet UV light, which represents a small portion of the natural sun light spectra[1]. Recently, enormous efforts have been made in order to improve the properties of TiO_2 and shift the absorption from UV region to visible light or infrared light regions. Such attempts have included doping the TiO_2 with metal/nonmetal elements and coupling TiO_2 with different colorful semiconductors or molecules. Some of those efforts have successfully tuned the properties of TiO_2. In this project, the optical properties of green TiO_2 were improved in a different way by introducing a hydrazine molecule, which is a bidendate ligand containing nitrogen atoms[2,3].

8.2 General research approach

Different spectroscopic techniques have been used in this project to determine what differentiates the green and white TiO_2 such as XPS, FT-IR and SSNMR. Green and white TiO_2 were prepared in the presence and absence of hydrazine monohydrochloride[4].

Our contribution to this project was applying SSNMR spectroscopy method, as it was a useful tool to reveal essential information about the reaction progression to synthesize a green and white TiO_2 and structural determination of green and white TiO_2[5].

8.3 SSNMR experiment

The SSNMR spectra was carried out on a three channel Tecmag Apollo console with 8.45 T magnet and homebuilt double- and triple-resonance SSNMR probes. The frequency of ^1H is 357.200 MHz, and the magic angle frequency rate was 8 KHz. Adamantine was used as an external reference. The proton direct excitation experiment was performed and each spectrum was acquired with 256 scans. Additionally, a proton spectrum was acquired for the empty rotor to measure the contribution of the rotor in the spectra. This contribution was then subtracted from each sample and the results were scaled by mass to obtain an accurate quantitative information about each sample.

8.4 Results and discussion

Figure 8-1 shows the solid-state ^1H NMR spectra of pure TiO_2, pure hydrazine monohydrochloride, white TiO_2, and green TiO_2 respectively. Figure 8-2 closely demonstrates the difference between green and white TiO_2. In both samples, green and white, there is a large broad peak around 5.43 ppm. Moreover, there is a peak near 1.11 ppm, which represents the absorption of H_2O, and a peak around 0.00 ppm which represents the absorption of DMF solvent on the surface.

In green TiO_2, a strong sharp peak was observed near 2.80 ppm and it is slightly different than the peak that was observed for hydrazine monohydrochloride around 3.08ppm (Figure 8-1). The slight difference indicates that the N in hydrazine was successfully substituted to the surface of TiO_2.

8.5 Conclusion

Solid-state NMR spectroscopy has displayed a critical role in this project as it noticeably supported the completion of the formation of desired materials. Furthermore, it confirmed the coordination of the hydrazine molecule to the surface of titanium atoms Ti.

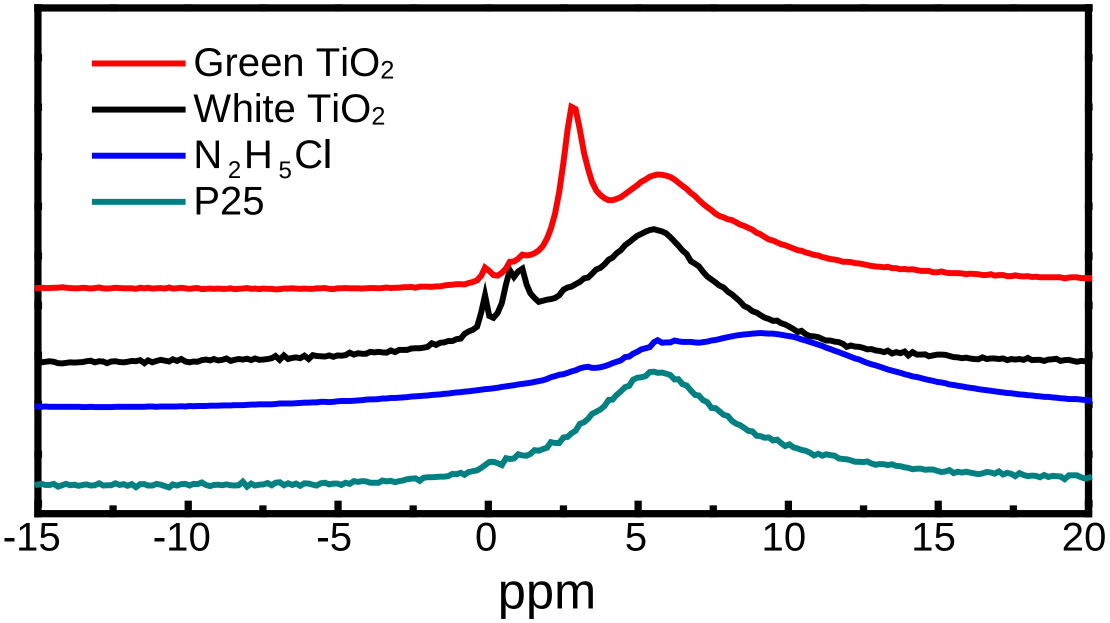

Figure 8-1. Solid-state NMR spectra for all samples

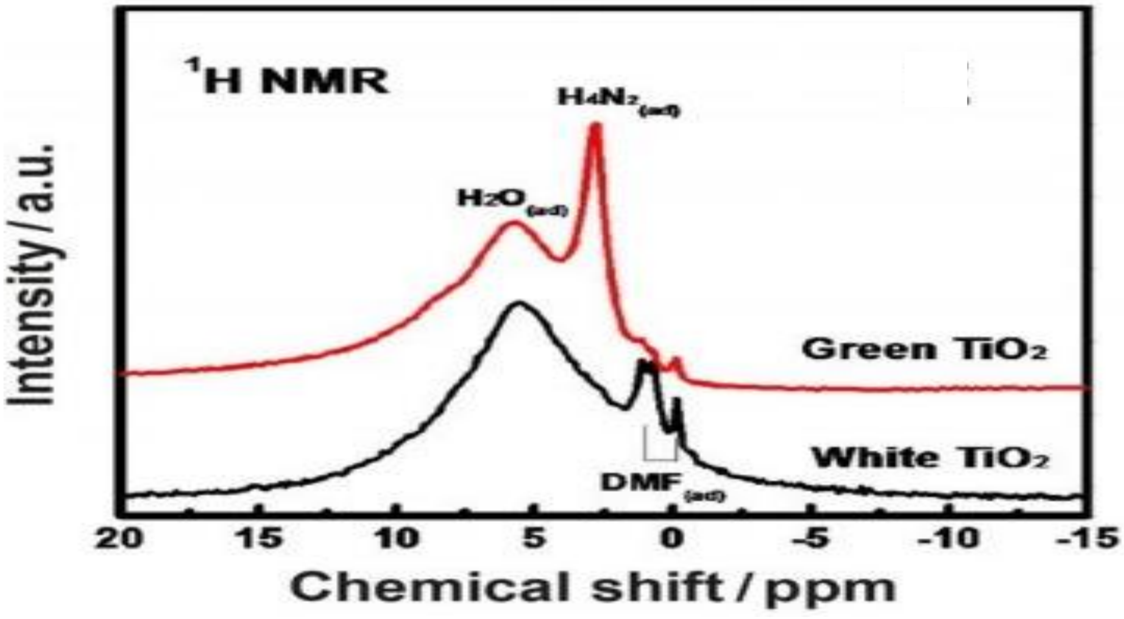

Figure 8-2. Solid-state NMR spectra for green and white TiO_2

References

(1) Kalathil, S.; Khan, M. M.; Ansari, S. A.; Lee, J.; Cho, M. H. Band Gap Narrowing of Titanium Dioxide (TiO2) Nanocrystals by Electrochemically Active Biofilms and Their Visible Light Activity. *Nanoscale* **2013**, *5* (14), 6323. https://doi.org/10.1039/c3nr01280h.

(2) Ohki, Y.; Tominaga, J.; Watanabe, T.; Rockstuhl, C.; Awazu, K.; Fujimaki, M.; Murakami, H.; Yoshida, N. A Plasmonic Photocatalyst Consisting of Silver Nanoparticles Embedded in Titanium Dioxide. *J. Am. Chem. Soc.* **2008**, *130* (5), 1676–1680. https://doi.org/10.1021/ja076503n.

(3) Bai, S.; Wang, L.; Chen, X.; Du, J.; Xiong, Y. Chemically Exfoliated Metallic MoS2nanosheets: A Promising Supporting Co-Catalyst for Enhancing the Photocatalytic Performance of TiO2nanocrystals. *Nano Res.* **2014**, *8* (1), 175–183. https://doi.org/10.1007/s12274-014-0606-9.

(4) Chen, X.; Mao, S. S. Titanium Dioxide Nanomaterials: Synthesis, Properties, Modifications, and Applications. *Chem. Rev.* **2007**, *107* (7), 2891–2959. https://doi.org/10.1021/cr0500535.

(5) Tian, L.; Xu, J.; Alnafisah, A.; Wang, R.; Tan, X.; Oyler, N. A.; Liu, L.; Chen, X. A Novel Green TiO 2 Photocatalyst with a Surface Charge-Transfer Complex of Ti and Hydrazine Groups. *Chem. - A Eur. J.* **2017**, *23* (22), 5345–5351. https://doi.org/10.1002/chem.201606027.

Appendix I

Synthesis of ^{13}C labeled ortho-carborane

In order to improve the S/N and measure the interatomic distances, a ^{13}C labeled precursor need to be synthesized. Since ^{13}C labeled chemicals are very expensive, the first aim is to find a synthetic scheme that uses the least expensive starting materials. Synthesizing ortho-carborane by reacting acetylene gas with decaborane has been done [1], but the yield was insufficient. Therefore, the studies were commenced by performing a proof of concept synthesis of ortho-carborane (before purchasing the rather expensive ^{13}C propargyl alcohol) following these steps: first oxidizing propargyl alcohol to obtain propiolic acid[2] , then protecting that with a t-butyl group to form t-butyl propiolate[2] and finally ortho-carborane was synthesized from a reaction of t-butyl propiolate with decaborane[3]. Solution NMR spectroscopy was used to analyze the results along with GCMS.

Currently, commercially available ^{13}C labeled propargyl alcohol is used. Due to its high cost, future work will include an additional reaction before this proposed scheme. This new step will produce ^{13}C labeled propargyl alcohol from ^{13}C labeled acetylene[4] as shown in (Figure 1)

Preliminary Data

Synthesis of propiolic acid

Procedure:

- Solution of propargyl alcohol was titrated with Jones reagent. The reaction mixture was stirred for an additional 1h at room temperature. 1ml of isopropanol was added to quench the Jones reagent. 100 ml of water was added, and the product was extracted with ethyl acetate. Figure 3 shows the ^{13}C NMR spectrum of propiolic acid.
- Result:

- Yield of propiolic acid was ~ 80% based on NMR spectrum integration (Figure 2).

Synthesis of t-butyl propiolate

- Procedure:

  A solution of propiolic acid and Et_2O was cooled to -78 °c. (Reacting component 1).10 ml of isobutylene was condensed. (Reacting component 2). Reaction component 1 was added to reaction component 2, followed by 1 drop of H_2SO_4. Reaction mixture was held at -78 for 4h, then allowed to warm at rt overnight. The mixture was diluted with water and the aqueous layer separated and extracted 3 times with Et_2O. Figure 4 a and b show the GCMS directly after synthesis and the final result respectively

- Result:

  The yield of t-butyl propiolate was ~ 80% based on NMR spectrum integration (Figure3).

Synthesis of ortho-carborane

This reaction is extremely water sensitive. All precautionary measures must be taken to completely eliminate water from the system. If these measures fail, boric acid will form instead of ortho- carborane.

- Procedure:

0.1g of decaborane was heated in acetonitrile (4 ml) to reflux under exclusion of oxygen and moisture. After 30 min, a solution of TBP (0.11ml) in anhydrous toluene (4ml) was added and the resulting mixture was heated. NMR spectra were acquired every 4 hours. After 15 hours, 1ml of methanol was added to the reaction mixture and refluxed for 30 min. Figure 4 shows the ^{11}B NMR spectra during reaction.

- Purification

The reaction mixture was purified by column chromatography (hexane: ethyl acetate 10:1). Fractions were combined and concentrated. NMR was taken as shown in (Figure 5).

- Result:

Sublimation Recovery: ~ 95%. Yield of O- carborane ~ 40% (Figure 6) based on NMR integration.

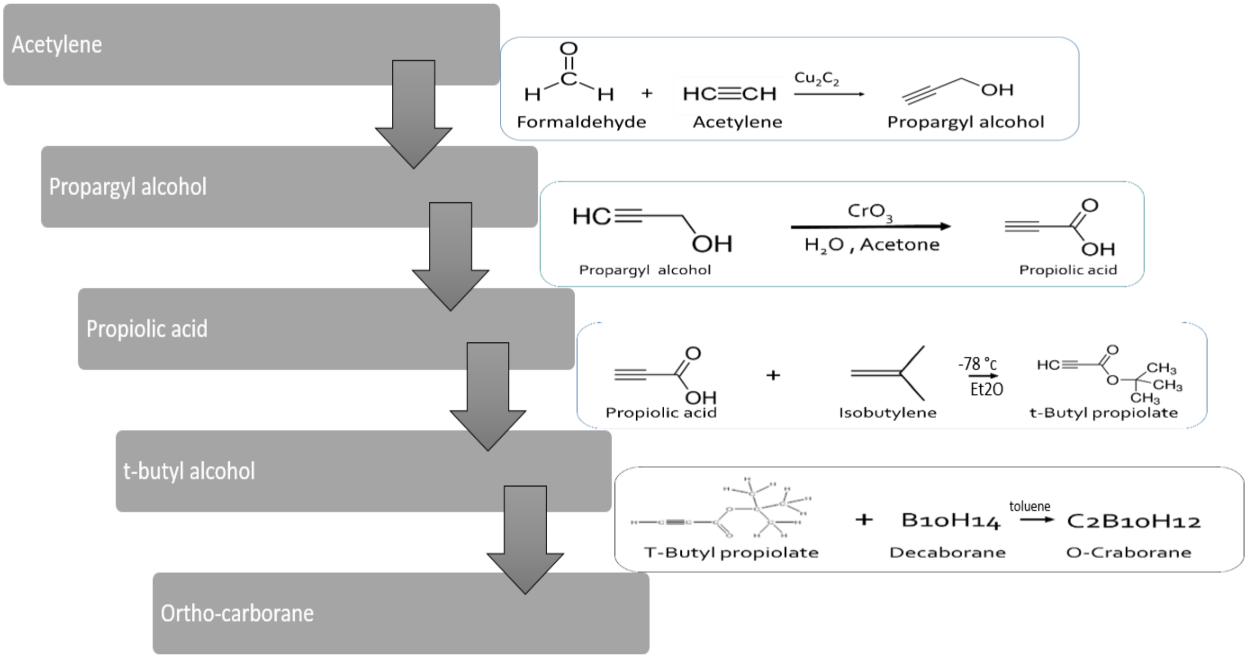

Figure1. Proposed Scheme of synthesizing ^{13}C ortho-carborane

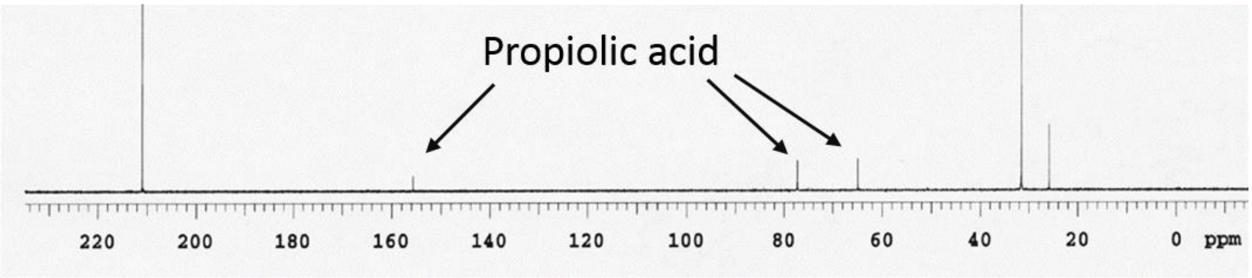

Figure 2. ^{13}C NMR spectrum of crude product

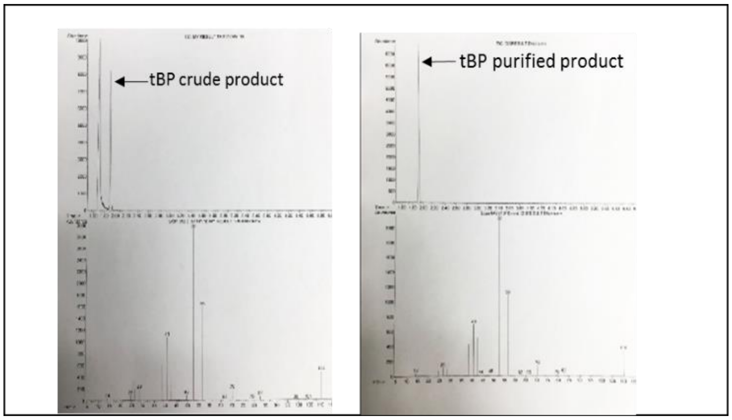

Figure 3.a: GCMS of crude product, b: GCMS result of purified product

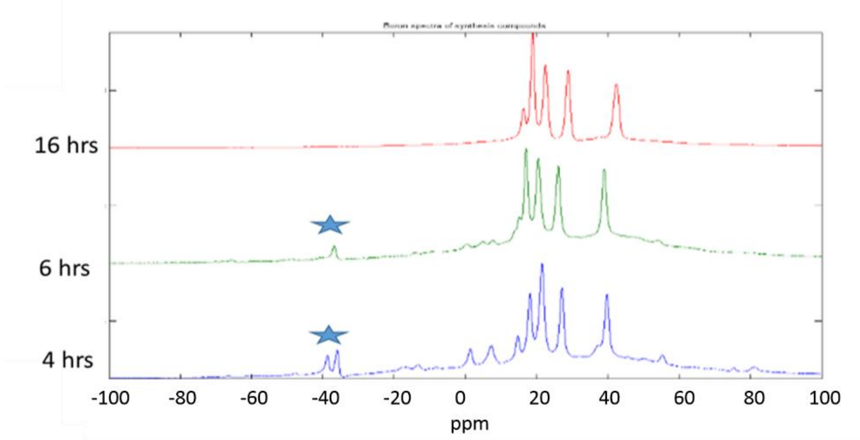

Figure 4. NMR spectra during reaction. The stars show one of the decaborane peaks disappearing as the reaction progresses. It is being converted to ortho-carborane.

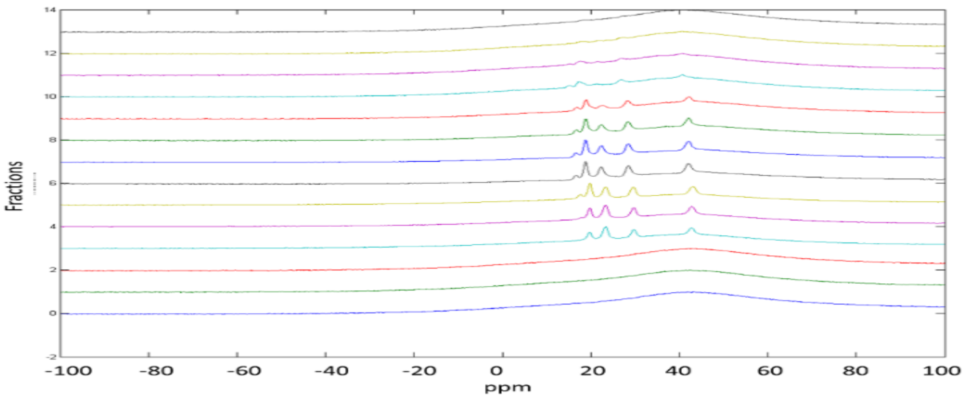

Figure 5. Fractions' NMR spectra during purification process

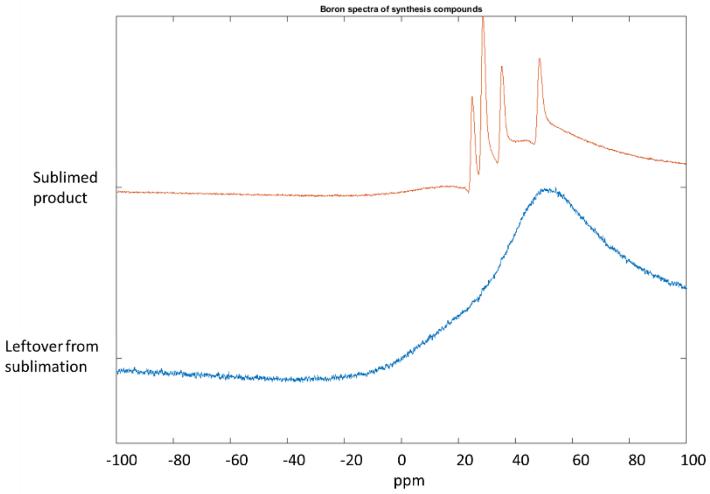

Figure 6. Sublimation results. The top spectrum contains purified product. The bottom spectrum is the leftover from the sublimation process. The absence of peaks shows that the entire product sublimed.

References

(1) Kusari, U.; Li, Y.; Bradley, M. G.; Sneddon, L. G. Polyborane Reactions in Ionic Liquids: New Efficient Routes to Functionalized Decaborane and o -Carborane Clusters. *J. Am. Chem. Soc.* **2004**, *126* (28), 8662–8663. https://doi.org/10.1021/ja048018n.

(2) Wolf, V. Notiz Über Die Darstellung Der Propiolsäure. *Chem. Ber.* **1953**, *86* (6), 735–737. https://doi.org/10.1002/cber.19530860615.

(3) Tietze, L. F.; Griesbach, U.; Elsner, O. Efficient Synthesis of Ortho-Carborane by Reaction of Propiolic Acid Tert-Butyl Ester with Decaborane(14). *Synlett* **2002**, *2002* (07), 1109–1110. https://doi.org/10.1055/s-2002-32586.

(4) Falbe, J.; Bahrmann, H.; Lipps, W.; Mayer, D. Alcohols, Aliphatic. In *Ullmann's Encyclopedia of Industrial Chemistry*; Wiley-VCH Verlag GmbH & Co. KGaA: Weinheim, Germany, 2000. https://doi.org/10.1002/14356007.a01_279.

VITA

Abrar Saleh Alnafisah was born on December 22, 1986, in Qassim, Saudi Arabia. She was educated in local public schools and graduated from high school in 2005. Subsequently, she joined Qassim University where she pursued and earned Bachelor's of Science (B.Sc.) degree in Chemistry with Summa Cum Laude in year 2009.

She joined Qassim University as a teaching assistant and worked for one year. Mrs. Alnafisah was awarded a scholarship from Qassim University to study abroad. She went to Iowa State University to study in the English program for a year and half. Then, she began a master's program in Chemistry at the University of Missouri Kansas City (UMKC). She was working under the guidance of Dr. Nathan A. Oyler and did various studies in boron carbide thin-films synthesis and characterization using Nuclear Magnetic Resonance (NMR). She was awarded her Master of Arts degree in Chemistry in May, 2016. She began work toward her doctorate degree in Chemistry at UMKC. Mrs. Alnafisah continued working with the same supervisor and expanded her work to various research topics, which implemented mostly solution as well as solid-state NMR spectroscopic techniques. Most of her research projects were collaborative efforts between the Department of Chemistry and School of Pharmacy, Department of Physics, and Department of Civil and Mechanical Engineering at University of Missouri Kansas City under the invaluable guidance of Dr. Nathan A. Oyler. Abrar also worked under the guidance of Dr. Andre Z. Clayborne in the summer of 2017 to learn the basic techniques of computational calculations.

Currently, Abrar is a candidate of Ph.D. in Chemistry as a primary discipline and Physics as a co-discipline at UMKC. She is a member of the American Chemical Society (ACS). She has presented the results of her research at various conferences such as: American Chemical Society national meeting and expo (Boston, MA, 2015), Midwest ACS (St. Joseph, MO, 2015), Midwest

ACS (Lawrence, KC, 2017), and ACS national meeting and expo (Boston, MA, 2018). Mrs. Alnafisah has authored and co-authored several publications.